Titre: Title:	Impact of Direct Aging Treatment on the Mechanical Properties of 18Ni-300 Maraging Steel Produced by Hybrid Additive/Subtractive Manufacturing
Auteur: Author:	Felipe Michels
Date:	2025
Type:	Mémoire ou thèse / Dissertation or Thesis
Référence: Citation:	Michels, F. (2025). Impact of Direct Aging Treatment on the Mechanical Properties of 18Ni-300 Maraging Steel Produced by Hybrid Additive/Subtractive Manufacturing [Mémoire de maîtrise, Polytechnique Montréal]. PolyPublie. https://publications.polymtl.ca/71954/

URL de PolyPublie: PolyPublie URL:	https://publications.polymtl.ca/71954/
Directeurs de recherche: Advisors:	Jean-Philippe Harvey, & Priti Wanjara
Programme: Program:	Génie des matériaux

POLYTECHNIQUE MONTRÉAL
affiliée à l'Université de Montréal

Impact of Direct Aging Treatment on the Mechanical Properties of 18Ni-300 Maraging Steel Produced by Hybrid Additive/Subtractive Manufacturing

FELIPE MICHELS
Département de génie chimique

Mémoire présenté en vue de l'obtention du diplôme de *Maîtrise ès sciences appliquées*
Génie des matériaux

Décembre 2025

POLYTECHNIQUE MONTRÉAL
affiliée à l'Université de Montréal

Ce mémoire intitulé :

Impact of Direct Aging Treatment on the Mechanical Properties of 18Ni-300 Maraging Steel Produced by Hybrid Additive/Subtractive Manufacturing

présenté par **Felipe MICHELS**
en vue de l'obtention du diplôme de *Maîtrise ès sciences appliquées*
a été dûment accepté par le jury d'examen constitué de :

Gilles L'ESPÉRANCE, président
Jean-Philippe HARVEY, membre et directeur de recherche
Priti WANJARA, membre et codirectrice de recherche
Denis THIBAULT, membre externe

ACKNOWLEDGEMENTS

I would like to deeply acknowledge my research director Prof. Jean Philippe Harvey, for believing in me and providing all the necessary support to complete this milestone in my career. I am grateful for the opportunity to conduct high-quality science abroad and for his guidance throughout this research project. I thank Prof. Gilles L'Espérance and Prof. Denis Thibault for accepting to be part of the review committee for this project.

I would also like to extend my special thanks to my co-supervisor Dr. Priti Wanjara and her entire team at the National Research Center (NRC), who spared no effort in providing me with all the support I needed to use the infrastructure and consumables to conduct my research in the best possible way. Their knowledge and experience guided me to achieve the high-quality results of this research. I would also like to express my gratitude to the NRC technicians, especially Xavier, Maxime, and Dan, who contributed enormously to the project by providing support in the synthesis, testing, and characterization of the samples.

To all my colleagues and friends at CRCT (Center for Research in Computational Thermochemistry) who made this journey more joyful. Special thanks to Dr. Aidin Barabi, who assisted me in performing mechanical tests, characterizing and analyzing samples, sharing his experience in problem solving.

To my family, who constantly encouraged me on this journey abroad, making it as pleasant and enjoyable as possible. My special thanks to Eduarda Depine Dornelles da Silva, who agreed to embark on this adventure with me and became my family, providing me with all the support and comfort I needed to complete this dream.

RÉSUMÉ

L'effet synergétique entre la matrice martensitique affinée obtenue par fabrication additive et le durcissement par précipitation résultant du traitement de vieillissement fait de l'acier maraging 18Ni-300 un excellent matériau pour les applications d'outillage de moulage par injection et les composants aéronautiques de haute performance. L'exploration de traitements thermiques alternatifs pour les aciers maraging fabriqués selon la technique de Fusion Laser sur Lit de Poudres (L-PBF) revêt un grand intérêt pour la communauté scientifique. En raison de la rapidité de refroidissement inhérente au processus, la microstructure initiale telle que fabriquée présente des mésostructures et de l'austénite résiduelle issues de la solidification qui peuvent être modifiés par migration des éléments solutés lors d'un traitement thermique postérieur, ce qui encourage la recherche de traitements plus efficaces. Le vieillissement direct s'est révélé être une alternative compétitive, offrant aux pièces une excellente résistance mécanique et des propriétés de ténacité améliorées par rapport aux traitements conventionnels. Ce traitement thermique peut être étudié plus en détails dans les aciers maraging imprimés par L-PBF, afin d'améliorer le rapport résistance-ténacité tout en réduisant les coûts de production.

Ce projet s'est donc concentré sur l'étude de l'impact de différentes températures de vieillissement direct sur les propriétés de traction et de résistance aux impacts Charpy de l'acier maraging 18Ni-300 imprimé par L-PBF. Plus précisément, la transition de température ductile-fragile (DBTT) a été étudiée pour chaque condition imposée, un thème qui a reçu peu d'attention dans la littérature sur la fabrication additive jusqu'à maintenant. À cette fin, 20 coupons en acier maraging 18Ni-300 ont été fabriqués en utilisant la technologie L-PBF. Ces coupons ont été usinés pour l'analyse de la densification des échantillons, la caractérisation microstructurale, l'analyse par diffraction des rayons-X, la microdureté Vickers et les essais de traction et de impacts Charpy. Un vieillissement direct a été effectué à 490 °C, 510 °C, 530 °C et 560 °C pendant 6 heures, suivi d'un refroidissement à l'air. La densification des coupons imprimés fut acceptable, résultant en des valeurs de dureté conformes à la littérature et une microstructure martensitique avec austénite résiduelle. Le traitement à 490 °C a conduit à une microstructure martensitique dure et à la formation d'austénite inversée, ce qui a entraîné une dureté et une résistance maximales au détriment de la ténacité. À mesure que la température augmentait jusqu'à 560 °C, on a observé une tendance à la réduction de la dureté et à un meilleur équilibre entre résistance et ténacité. Cela s'explique par une augmentation du volume d'austénite, qui agit comme une phase ductile et peut potentiellement déclencher l'effet de plasticité induite par transformation (TRIP). Des courbes

DBTT ont été développées et ont montré un déplacement de cette transition fragile-ductile vers des températures plus élevées à mesure que la température de vieillissement direct fut augmentée.

ABSTRACT

The synergistic combination of additive manufacturing's refined martensitic matrix coupled with precipitation strengthening from aging treatment makes 18Ni-300 Maraging Steel an excellent solution for injection mold tooling applications and high-performance aircraft components. They require complex, high-strength geometries while possessing good toughness to withstand stresses under critical conditions. The exploration of alternative heat treatments for maraging steels manufactured by L-PBF technique has been of enormous interest to the scientific community. Due to the rapid cooling rate inherent to the process, the as-built microstructure exhibits mesostructures and retained austenite from solidification that can be levelled up by solute migration with post-heat treatment, which encourages the quest for more effective treatments. Direct aging has been a cost-effective alternative, providing excellent mechanical strength and enhanced toughness properties compared to conventional treatments. As there is still no post-heat treatment procedure fully accepted by the industrial additive manufacturing community, direct aging can be investigated in L-PBF-printed maraging steels to improve the strength-toughness relationship while reducing production costs. The project focuses on studying the impact of different direct aging temperatures on the tensile and Charpy impact properties of 18Ni-300 maraging steel printed by L-PBF. In depth, Ductile-Brittle Temperature Transition (DBTT) will be investigated for each direct aging condition imposed, a topic that has received limited attention in additive manufacturing literature. For this purpose, 20 prismatic coupons of 18Ni-300 maraging steel were manufactured using Additive-Subtractive Hybrid Manufacturing (ASHM) based on optimized process parameters. These coupons were machined for analysis of the as-built sample densification, microstructural characterization, X-ray diffraction (XRD) analysis, Vickers microhardness, and tensile and Charpy impact tests. Direct aging was performed at 490 °C, 510 °C, 530 °C, and 560 °C for 6 hours, followed by air cooling. The densification of the printed coupons was acceptable, resulting in hardness values consistent with the literature and a soft martensitic microstructure with residual retained austenite. Direct aging treatment at 490 °C led to a hard martensitic microstructure and the formation of reverted austenite, which resulted in peak strength at the expense of toughness. As the direct aging temperature increased up to 560 °C, a trend was observed towards hardness reduction and a better strength-toughness balance. This can be explained by the increase in austenite content, which acts as a soft phase and can potentially trigger the transformation-induced plasticity (TRIP) effect. DBTT curves were developed, resulting in a shift towards higher temperatures as the direct aging temperature increased.

TABLE OF CONTENTS

LIST OF TABLES

LIST OF FIGURES

LIST OF SYMBOLS AND ACRONYMS

AM	Additive Manufacturing
MAM	Metal Additive Manufacturing
L-PBF	Laser-Powder Bed Fusion
ASHM	Additive-Subtractive Hybrid Manufacturing
Ni	Nickel
SL	Stereolithography
CAD	Computer-Aided Design
STL	Standard Tessellation Language
SLS	Selective Laser Sintering
DED	Directed Energy Deposition
EB	Electron Beam
BJT	Binder Jetting
LB	Laser Beam
SLM	Selective Laser Melting
18Ni-300 MS	18Ni-300 Maraging Steel
ED	Energy Density
PSD	Particle Size Distribution
ST	Solution Treatment
STA	Solution + Aging
DA	Direct Aging
UTS	Ultimate Tensile Strength
YS	Yield Strength
El	Elongation
E	Young Modulus
TRIP	TRansformation-Induced Plasticity
SFE	Stacking Fault Energy

HV	Hardness Vickers
DBTT	Ductile-Brittle Transition Temperature
SEM	Scanning Electron Microscope
TEM	Transmission Electron Microscopy
AD	Apparent Density
EDM	Electro-discharge Machining
XRD	X-Ray Diffraction
DIC	Digital Image Correlation
OM	Optical Microscope
AB	As-Built
DA490	Direct Aging at 490 °C
DA510	Direct Aging at 510 °C
DA530	Direct Aging at 530 °C
DA560	Direct Aging at 560 °C
EDS	Energy-Dispersive X-ray Spectroscopy

CHAPTER 1 INTRODUCTION

The Additive Manufacturing (AM) market has been growing significantly in recent years. This technology sector tripled its revenue in just six years, from approximately 6 billion in 2016 to 18 billion in 2022 [1]. More specifically, the Metal Additive Manufacturing (MAM) industry grew by 24.4% in sales in 2023 compared to the previous year [1]. Among the most widely applied MAM techniques, Laser-Powder Bed Fusion (L-PBF) is becoming a promising alternative for producing high-performance complex parts with material-saving efficiency, offering the potential of recycling powder-based feedstock. In order to produce parts with high surface quality while maintaining optimal density and mechanical response, an integration of L-PBF manufacturing combined with high-speed micromachining has been adopted, referred to as Additive-Subtractive Hybrid Manufacturing (ASHM).

Maraging steel belongs to a special class of low-carbon steels with high Nickel (Ni) content, well-known for their strengthening by precipitation of intermetallic compounds upon aging. Since 1960, traditional maraging steels, such as 18Ni grade, have been designed to achieve high strength while good ductility and excellent fracture toughness in the absence of carbon, which has proven valuable in aerospace/aircraft aplications, military, nuclear and tooling industries [2]. This trade-off between mechanical strength and toughness is of paramount importance to withstand the impact loads projected for tooling applications such as plastic injection molding, high-pressure die casting, extrusion, and punching.

In particular, 18Ni-300 maraging steel shows a synergistic effect of excellent weldability with a high cooling rate to achieve grain refinement combined with a small amount of retained austenite after manufacturing parts using the L-PBF process [3]. However, the formation of mesostructures induced by melt pools due to the conditions imposed in the L-PBF process can generate heterogeneities in the microstructure as well as micro-segregations that can affect the material's mechanical properties [4]. Thus, heat treatments or thermal cycles are imposed to homogenize the microstructure while allowing the precipitation of intermetallics, thus, increasing the ultimate tensile strength and yield strength of the steel, at the expense of a reduced ductility.

Extensive research has focused on conventional heat treatment cycles such as solution treatment at temperatures above 720 °C until 1000 °C to remove laser scan tracks and cellular substructures, followed by aging treatment at 450-600 °C to promote the formation of hard intermetallic particles (such as Ni_3Mo, Ni_3Ti, Ni_3Al, and Fe_2Mo) within the martensitic matrix, which restricts the movement of dislocations, thus strengthening the material [3].

Such traditional heat treatment for additively manufactured maraging steel still need to be optimized (specifically the temperature program and thermal cycle length) to finely tune the mechanical properties of the alloy. For L-PBF processes, the material is subjected to cyclic reheating and cooling among the built layers, as an in-situ heat treatment, which can favor the precipitation of nanoparticles without the need for solution treatments as in conventional heat treatment cycles [3]. Thus, a new direct aging route has been explored to optimize the microstructure, promoting the precipitation of hard nanoparticles while maintaining mechanical properties similar to wrought 18Ni-300 maraging steel [5].

Aerospace and tooling applications require excellent toughness to overcome impact loads at high service temperatures [6]. For direct aging treatment, the literature focuses on achieving peak mechanical strength, which typically occurs at temperatures around 480 to 500 °C. The high density of hard particles while minimal austenite content obtained in the microstructure at this temperature range contributes to an excellent strength mechanical response despite poor ductility [7]. By increasing the temperature above 500 °C, a balance in the strength-toughness ratio can be achieved through an increase in the austenite content in the microstructure and the dissolution of precipitates in the matrix. Thus, it becomes imperative to study a broader range of direct aging temperatures capable of addressing the toughness requirement without excessively compromising the strength of printed 18Ni-300 maraging steel [6]. In addition, to understand the toughness behavior at high temperatures, the ductile-brittle transition temperature of maraging steels can be explored, a field that has received limited interest although it is essential for tooling applications.

CHAPTER 2 LITERATURE REVIEW

The following sections will define various concepts that are required to understand the many themes that are covered in this thesis, which include 1) the general aspects of metal additive manufacturing, and 2) the principles of L-PBF process. In addition, it will cover the influence of physical-chemical characteristics of maraging steel powder on the final bulk printed properties and mechanical behaviour after post processing heat treatment.

2.1 Metal Additive Manufacturing (MAM) Systems

The development of AM dates back to the 1980s, mainly with a focus on rapid prototyping of components in polymeric materials, wood or paper using Stereolithography (SL) [8]. From that point onwards, industrial technological innovations allowed a diversification of available materials to be applied in additive manufacturing. Nowadays, the term has become more broadly defined, given the wide range of AM technologies and materials that can be employed. Thus, the definition of additive manufacturing, according to ISO/ASTM 52900:2021(E), refers to *all those technologies that manufacture layer-by-layer joined material to create physical objects, as specified by 3D model* [9].

In this regard, it specifies that there are fundamental steps that define additive manufacturing technology, which are: the digital phase, the manufacturing phase and the post-processing phase (Figure 2.1).

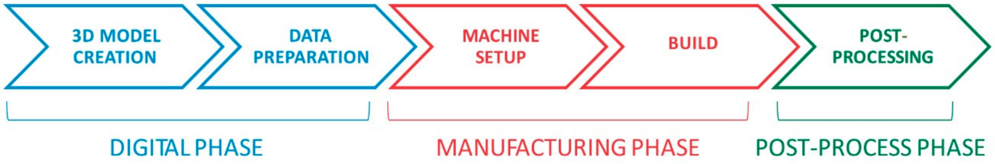

Figure 2.1 Fundamental Phases of Additive Manufacturing (AM) process [10].

These main phases feature sub-steps that are essential in order to achieve a successful manufacture of the intended component/part. During the digital phase, it is required to create the 3D object of the planned component using a dedicated software which typically generates a Computer-Aided Design (CAD) format. This CAD format is then converted into an Standard Tessellation Language (STL) file, which is processed to generate fixed-thickness digital slices of horizontal layers of the 3D object. For the manufacturing phase, the file with the pre-established slices is loaded into the building machine and the printer is configured according to the selected process parameters. The component is then manufactured layer-by-layer until completion. The post-processing phase can comprise various sub-steps depending on the product process, such as: removal of the part from the build platform, removal of the support structures, machining, heat treatment, etc [10].

Conventional metal manufacturing is often characterized by multi-processes based on material casting, subtraction and subsequent post-processing (i.e., heat treatment and surface finishing) to transform the component to its final shape. This usually requires casting devices that limit the geometry/shape of the part, incurring in longer industrial production cycles and substantial costs. AM processes have successfully bridged the gap of rapid prototyping in almost every field of production. It has become capable of manufacturing highly complex parts in geometry/shape with a low production lead time, under stricter control conditions, making good quality serialized parts. With AM processes, it is possible to optimize raw materials feedstock while refining the material composition, producing parts with high dimensional tolerances without the need for costly dies or molds [11].

Envisioning the long-term advantages of AM, the first patented metal additive manufacturing technology was Selective Laser Sintering (SLS) in 1986 [12], in an attempt to print prototypes through a layer-by-layer process inspired by weld cladding technology. After the first patent, several other technologies were created, such as Binder Jetting (BJT), based on the inkjet binder deposition method, as well as Directed Energy Deposition (DED) technique, in which the raw material feedstock is deposited directly into a melt pool [8].

A considerable improvement was achieved in AM techniques after the introduction of lasers or Electron Beam (EB), which made it feasible to increase the deposition rate of material on the layers and precisely focus the electron beam, resulting in a better dimensional and metallurgical end-product quality. Adjusting the thermal intensity allowed a good distribution of thermal energy among the layers and control of the depth of thermal penetration, which plays a key role in the final microstructure of the material [13].

The development of laser-based technologies has mainly taken place through SLS or Powder Bed Fusion processes where a high-powered energy source is focused onto a powder bed, in which it will progressively melt and ensure controlled re-solidification, layer-by-layer. Currently, it has become one of the most promising and commercially used technologies, despite its limitations and technological challenges.

The variations between MAM systems depend on the energy source used for the process, as well as how the raw material is delivered to the system and its distribution under the building surface. Based on the type of technique, the feedstock material can be delivered in the form of powder, filament/wire, or sheet. Usually, the metallic powder feedstock is distributed on the build plate in layers in a L-PBF process or deposited by a nozzle in a DED [14]. In other types of technique, such as BJT, a solvent is used as a binding agent in a layer of powder to carry out the printing process. Sheet lamination (SHL) uses sheets as feedstock and ultrasound to manufacture bulk parts. Figure 2.2, taken from Lavernia et al. (2024) [14], shows the categories of MAM processes, as well as their differences in terms of feedstock and energy source.

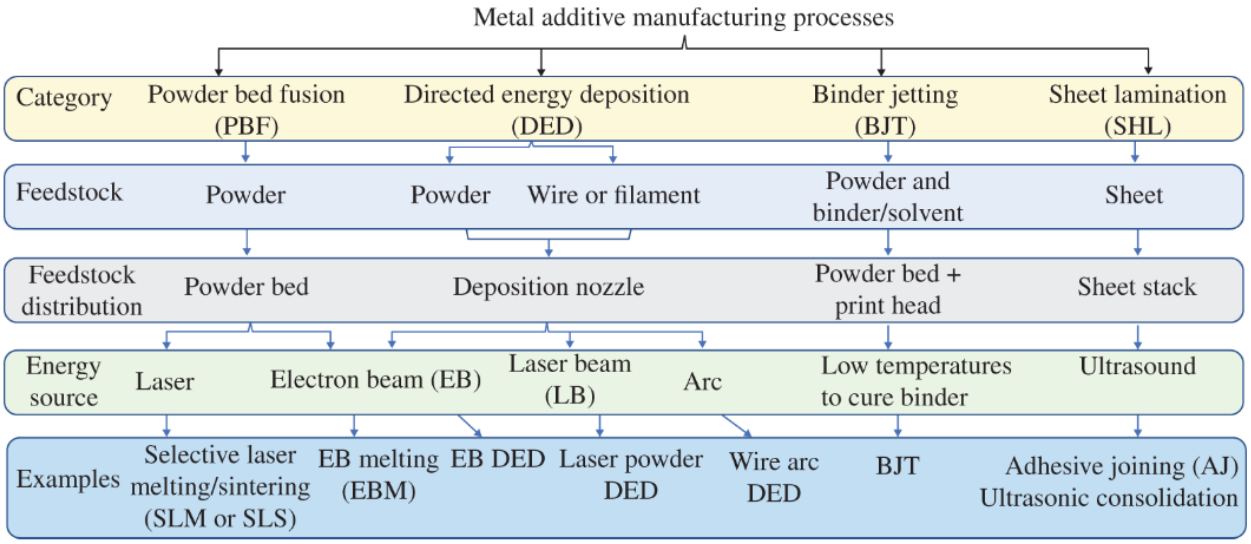

Figure 2.2 Categories of MAM processes [14].

2.1.1 Developments and Limitations

The market's landscape demand for metal additive manufacturing has gained traction with the rise of "on-demand manufacturing" as a complementary technique to traditional manufacturing. MAM has allowed freedom to build complex parts with greater precision and tight control of process parameters. The flexibility brings along the ability to customize and personalize parts, reducing mold and tooling costs maintaining structural and mechanical integrity [15].

Since this technique builds up layer-by-layer, material is only added where necessary, thereby reducing the cost of material waste and reducing the footprint of the operation [16]. Depending on the material being applied and the customer's specifications, it is possible to recycle the powder several times, increasing the raw powder's lifespan and decreasing production costs. Nevertheless, there is evidence that powder's characteristics and mechanical properties can be affected by the use of recycled powder [17, 18], as well as the presence of impurities in the powder. Therefore, monitoring the physical and chemical properties (i.e.

flowability, densification, particle size distribution, morphology, chemical composition) of the powder is of great importance [19].

The numerous opportunities mentioned can be contrasted with the inherent limitations of MAM processes. The production speed of components is still one of the great challenges of the technique, which, despite improvements, is still slow for large production scales. Depending on the selected process, the size of the part manufacturing area is still limited, making it a process limited to prototyping and small-scale manufacturing [20].

There are challenges regarding the type of material that can be processed, which is highly dependent on the possibility to densify the printed product. In fact, the process parameters (i.e. laser power, scanning speed, hatching space and layer thickness) must be fine-tuned on the basis of the selected material to ensure maximum homogeneous densification throughout the complex geometry of the final component. Non-optimal processing conditions may lead to poor mechanical performance compared to traditional processes. In addition, the need for post-processing steps in most MAM processes due to poor geometrical resolution and final surface finish increases manufacturing lead-time and drives up production costs [21].

As MAM is a relatively new technology, there is still substantial room for innovation and improvements. In fact, this has been the subject of many recent scientific publications. One of these advances is Additive-Subtractive Hybrid Manufacturing (ASHM), which primarily addresses surface finish quality limitations while saving post-processing time by incorporating subtractive processes, such as machining, into the AM workflow. This merging of additive/subtractive processes enables higher levels of precision and better final quality of the printed sample, while lowering production costs. Also, as studied by Mashhadikarimi et al. (2025) [22], the ASHM technique can be used for the assemblage of dissimilar materials (in this case maraging steel powder printed onto a S7 tool steel) to repair and increase the durability of components, extending their service life. Using optimal post-processing conditions, these authors demonstrated that it was possible to obtain a stable, stress-free, and mechanically robust dissimilar joint that can be used in the development of tool inserts with confirmed cooling channels [22]. **The ASHM process will be used in this project to print high-quality final products using previously optimized processing parameters.** The focus of the present study will be on the post-processing stage (i.e. the direct aging heat treatment) and its impacts on the mechanical properties of the printed parts.

2.2 Laser Powder Bed Fusion (L-PBF)

Among all the AM process categories discussed in section 2.1, Powder Bed Fusion (PBF) based technologies stand out for their major contributions to the MAM market. PBF processes are capable of producing parts with complex geometries and good metallurgical quality [23, 24]. According to ISO/ATSM 52900, PBF can be defined as *a process in which thermal energy selectively melts regions of a powder bed or bonded by means of an adhesive to build up parts* [9]. A PBF technology comprises one or more thermal energy sources (Laser Beam (LB), EB, or Infrared Light (IrL)), a mechanism to control the powder fusion to a selected region of each layer, and methods for precisely adding and controlling the powder layers.

The principles on which the L-PBF process is based are schematically illustrated in Figure 2.3, taken from Spears and Gold (2016) [25]. As shown on this figure, the system requires a build plate, which serves as the printing area on which the part will be produced. During the printing process, a system of lenses and mirrors reflect and redirect the LB to the surface of the build platform. The LB's position in the planar directions (X-Y) is controlled by adjusting the mirror's angle according to the selected parameters in CAD. A powder layer of pre-defined thickness (i.e. between 20 and 100 μm [26]) is added to the build platform from the recoater and the LB fuses this thin layer of powder according to the geometry of the part. The build plate is then moved downwards (z-direction) and the recoater blade pushes another new fresh layer of powder from the powder reservoir and spreads it uniformly on top of the previous layer. The process of fusion by the laser beam and the addition and spreading of the powder is repeated until the desired part is completed [14].

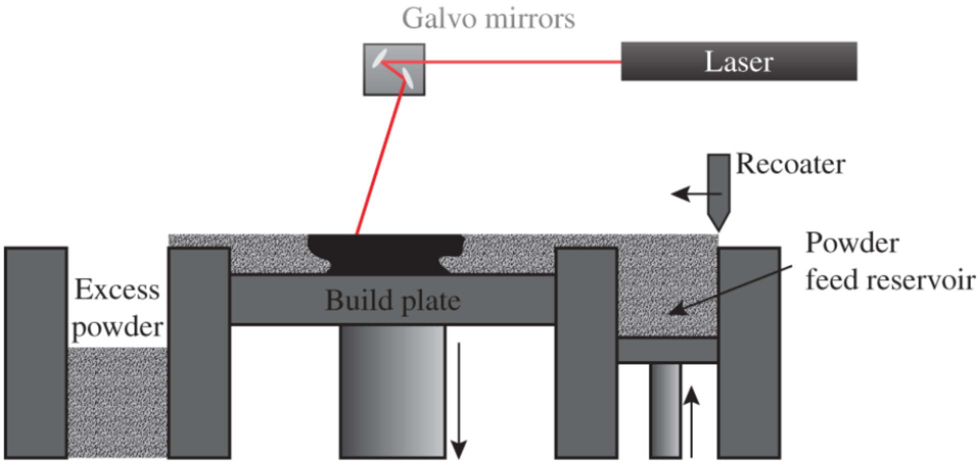

Figure 2.3 Schematic illustration of the Powder Bed Fusion (PBF) process [25].

As the printed part must be smaller than the area of the building platform, the manufactured component is surrounded by the excess unused/unmelted powder in each layer, serving as a support structure for the subsequent layers, eliminating the need for secondary supports. In L-PBF processes, the printing of the part takes place inside a enclosed chamber filled with inert gas, typically argon or nitrogen, to minimize oxidation and degradation of the powder material which is critical when printing metals and alloys. Also, the temperature of the environment is controlled using infrared heaters, as well as the build plate using resistive heaters. This uniform temperature control of the build platform and powder above room temperature is necessary to minimize laser power requirements and prevent warping of the part from non-uniform thermal expansion and contraction mechanisms. When the part is completed, a cool-down period is required to allow the component to reach room temperature prior to handling. This avoids exposing the hot part to oxidation/degradation in the presence of oxygen and/or thermal shock. The part is finally removed from the build plate, the excess powder surrounding it is cleaned off and finishing operations are employed [27].

Multiple mechanisms are possible during powder fusion: liquid-phase sintering, solid-state sintering, chemically induced binding and full melting. For this reason, the terminology used to describe the L-PBF process has become broad. Common terms used in the literature include Selective Laser Sintering (SLS), Selective Laser Melting (SLM), Laser Metal Fusion (LMF), Laser Beam Melting (LBM), etc. Although there are various mechanisms and terminologies that use the word "sintering", L-PBF systems applied to metals are based on the complete full melting of the particles instead of sintering them [28, 29].

One of the great advantages of L-PBF is the vast market in which it can be applied, such as the biomedical, engineering, automotive, aerospace, transportation and jewelry industries [30]. This is due to the possibility of applying a range of metals to the process without compromising the mechanical quality and characteristics of the desired component. The main types of metal components produced by L-PBF that have gained traction are aluminium, titanium and cobalt-chromium alloys, as well as stainless steels and ultra-high-strength steels such as maraging steel [31].

Nevertheless, the microstructure of these materials is intrinsically related to the rapid cooling of subsequent layers inherent in the L-PBF process. The rapid solidification and high temperature gradient between layers can reach up to 108 K/s, leading to metastable phases, segregations and undesirable metallurgical defects [31].

Several phenomena occur in the interaction between LB and the powder (Figure 2.4), which, depending the laser power applied, can take four distinct states of matter (i.e. solid, liquid, gas and plasma), influencing particle dynamics, thermal fluid dynamics, solid state transformations and mechanical states that can cause defects and compromise mechanical properties [32].

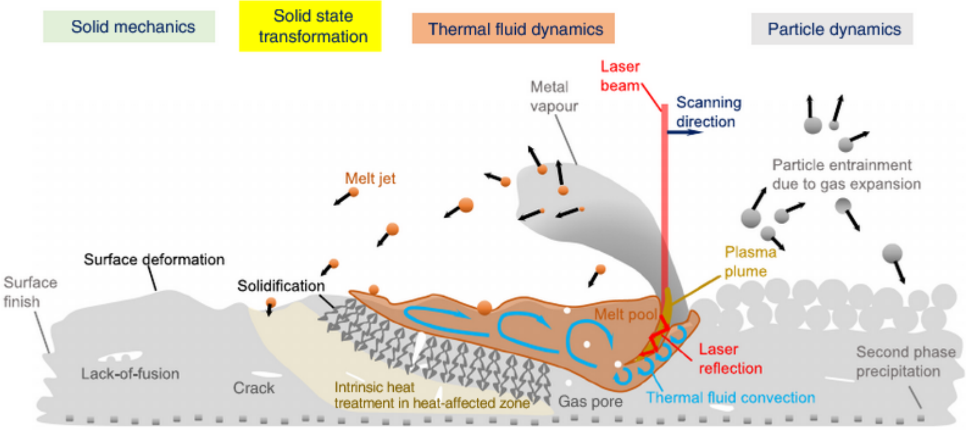

Figure 2.4 Schematic illustration of multi-physics phenomena in powder-bed fusion process [32].

During laser-material interaction, the powder can experience absorption, transmission and reflection of the incident laser beam. The energy absorption in the powder particles is high enough to melt and form the so-called melt pool. Due to the high energy density per unit area of the laser, the movement of the liquid metal can become highly turbulent in the melt pool region [33]. If the laser energy is too high, it can vaporize the melt pool elements and even ionize the metal vapour and form plasma. This interaction can lead to complex dynamics and fluid drag phenomena, particle movement and microstructural solidification that still remain a research challenge [34].

In fact, each material has its own physical powder characteristics that can affect the powder/LB interaction and the final microstructure, as well as the process parameters that influence the densification of the component, print quality, defects and mechanical properties. Thus, the following subsections will detail the most critical process parameters for L-PBF technology as well as intrinsic material powder properties that can affect the printing process and the final microstructure.

2.2.1 Influence of Process Paramenters

The selection of L-PBF process parameters directly influences the complex transient thermal behavior of the melt pool, in which they can be changed independently, though this selection of parameters generates a multi-variable optimization problem. The relationship between process parameters/strategies and melt pool characteristics may often result in unexpected metallurgical defects, such as pores, warping, thermal cracking, shrinkage and unintentional anisotropic physical and mechanical properties [10]. Therefore, understanding the effect of each input parameter is essential in order to meet the specifications of the designated component while obtaining the optimum product quality. The main critical parameters (Figure 2.5) will be discussed in the following subtopics.

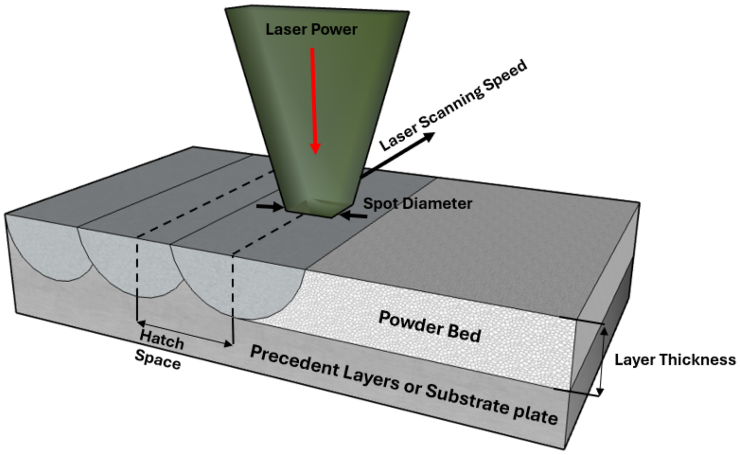

Figure 2.5 Schematic illustration of the main critical process parameters in L-PBF process. Elaborated by the author.

2.2.1.1 Scanning Strategies

During the L-PBF process of manufacturing the component, temperature control of the environment as well as the part is essential in order to reduce the temperature gradient and reduce any deformations and residual stresses. Therefore, the direction of the laser beam's planar movement can cause excessive heat input in localized regions of the part, generating a temperature gradient that leads to stress generation. The accumulation of stress and deformation by repeated thermal cycles through each layer can lead to compromised mechanical properties and potential failure [31].

Thus, the scanning strategy is one of the critical process parameters for achieving stable temperatures during the process and good print quality. The choice of laser beam spatial movement pattern can be selected according to the material employed, part geometry, hatching space, targeted microstructure and mechanical properties. The pattern can be changed according to the printing direction, scanning sequence, rotation angle, etc. Figure 2.6, taken from Abd-Elaziem et al. (2022) [31], shows the main scanning strategy patterns used in L-PBF processes.

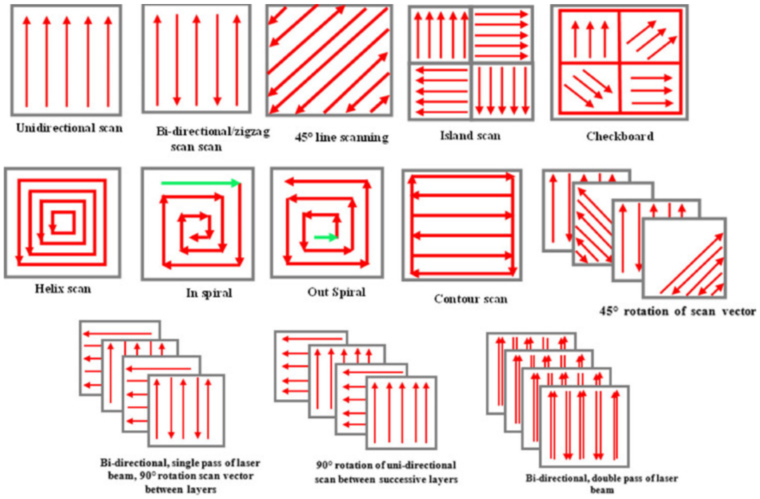

Figure 2.6 Schematic illustration of the main scanning strategies implemented in L-PBF [31].

Wan et al. (2018) [35] studied the effect of the bidirectional scanning strategy with and without 90° rotation on an L-PBF-printed Inconel 718 and concluded that different grain structures are formed in the melt pool according to the scanning strategy used due to the control of the heat flow direction and local thermal gradient. The direction of the laser beam during the L-PBF process has a major influence on the crystallographic texture and the uneven response of the alloy's elastic and plastic properties of the printed component due to the variation in the solidification rate and the configuration of the melt pool. Bhardwaj and Shukla (2018) [36] adopted the strategy of rotating 90° bidirectional and cross-directional on 18Ni-300 MS L-PBF printed samples and reached the conclusion that there is a preferential growth of columnar cells followed by epitaxial formation in both directions, resulting in higher compressive residual stresses. They also obtained a higher percentage of retained austenite in the bi-directional strategy (around 10%), impacting on the tensile properties of the material.

The rotation of the scanning angle is also of key importance for the morphology of the melt pool and the final microstructure. Joo et al. (2024) [37] investigated 3 different scanning rotations (0°, 45° and 90°) on 18Ni-300 MS during direct melt deposition to discover that the 45° sample exhibited a denser melt pool distribution, with a higher concentration of retained austenite and fine martensite. The combination of high back-stress hardening with a fine martensite block and lath size allowed this sample to achieve the best tensile properties.

For parts printed on L-PBF, which feature LB scanning patterns, uniaxial movement of the build plate and powder deposition in layers, the mechanical properties are inherently anisotropic. Nevertheless, post heat treatment of the parts increases the residual stress relaxation of the microstructure and reduces the anisotropy of the part. For example, Mooney et al. (2018) [38] investigated the effect of heat treatment on the mechanical properties and plastic anisotropy of 18Ni-300 MS fabricated at 0°, 45° and 90°. In fact, a considerable anisotropy was found for the as-built sample, which was drastically reduced after the aging treatment. Karlapudy et al. (2023) [39] obtained notable improvements in the anisotropy of tensile and hardness properties for different heat treatment conditions compared to as-built 18Ni-300 MS manufactured using the L-PBF technique.

Furthermore, the appropriate selection of the printing strategy contributes to a better uniformity of temperature distribution and solidification of the final microstructure. As most materials are not applied in their as-built state, especially maraging steels, a better understanding of the relationship between heat treatments after the L-PBF process and anisotropy properties will be discussed in Section 2.3.2.

2.2.1.2 Laser Power

During L-PBF process, the solidification of the melt pool is determined by energy absorption and heat transfer in the powder/energy interaction zone. Since the energy source comes from a laser beam, what will dictate high quality printing and high relative density is the laser-related parameters such as laser power, the laser mode (continuous or pulsed), the area to which the energy will be applied (spot size) and the amount of time the energy will be applied to a given area (scanning speed) [25]. This laser-related parameters can be used to describe the Laser energy density, which refers to energy level absorbed by a volumetric unit of powder during the melting process and is correlated to the specific contribution of the process parameters to the heat input by the laser beam. The laser Energy Density (ED) can be estimated as follows:

$$ED = \frac{P}{vht} \tag{2.1}$$

Where "P" represents the laser power (W), "v" is the scanning speed (mm/s), "h" is the hatching spacing (μm) and "t" is the layer thickness (μm). The variation in these parameters influences the densification of the material, since insufficient laser power input can form lack-of-fusion defects (i.e. unmelted powder), which leads to the generation of pores in the microstructure of the material, affecting the relative density of the component. As the laser energy increases, more particles will be fully melted in the melt pool region, increasing the densification of the material. However, excessive laser power can cause material vaporization and spatter particules that decreases the relative density of the part [40].

Mutua et al. (2017) [41] and Casalino et al. (2014) [42] aimed to optimize the relative density of maraging steel processed by L-PBF by varying the laser power and scanning speed, demonstrating its effect on the mechanical and physical properties of the printed material. Casalino et al. (2014) [42] established the baseline, highlighting that laser power must be higher than 90 W to achieve relative densities above 99%, with pore sizes less than 30 μm. Mutua et al. (2017) [41] found that laser power of 100 W produces 97.9% of relative density with irregular pore sizes. As the laser power increased to 300 W, the relative density reached its maximum of 99.8%, however at 400 W the relative density decreased to 99.2%. This decrease in relative density caused by the high ED occurred due to the presence of spherical pores caused by gas entrapment within the melt pool.

Bai et al. (2017) [40] reinforced the idea of the relative density threshold, for which it was a laser power of 160 W, achieving a dense specimen of 99.19%. It also concluded that low ED (low laser power and high scanning speed) leads to insufficient powder fusion. High ED (high laser power and low scanning speed) generates high metal vaporization and spatter, forming voids and inclusions. For Sarafan et al. (2021) [43], the optimized relative density (99.0-99.8%) of 18Ni-300 MS samples came from high laser power levels of 240 W (ED = 57.1 J/mm^3) to 320 W (ED = 76.2 J/mm^3), with coarser pores of up to 50 μm. At power levels of 380 W (ED = 90.5 J/mm^3), the volume of coarser pores reached 100 μm, due to the development of gas bubbles, coalescence of small pores at high power and vaporization of the powder. With ED increasing to a value above 67 J/mm^3 there is a higher probability of the relative density reaching values greater than 99%. However, care should be taken with this simple rule since a similar energy density of 68 J/mm^3 can lead to densities in the range of 78.0 to 99.4% (since the same energy density corresponds to different process parameter combinations [44]).

2.2.1.3 Laser Scanning Speed

In contrast to laser power, the scanning speed parameter has a different effect on the relative density of printed components. According to the Equation 2.1, low scanning speeds lead to a high ED. When excessively slow, it promotes vaporization and spreading of the particles in the melt pool, increasing the percentage of pores in the material. At the opposite, high scanning speeds can reduce the process lead time but also affect the quality of the melt pool, contributing to a lack of sufficient energy for the total melting of the particles, forming lack-of-melting defects [3, 40].

Adjustments must be made to these parameters to ensure that the material solidifies properly without the presence of metallurgical defects that are detrimental to the material. In the research by Mutua et al. (2017) [41], by increasing the scanning speed from 400 to

700 mm/s, there was an improvement in relative density from 98.4 to 99.8%. However, when the scanning speed was increased to 1000 mm/s, the relative density decreased to 98.7%. The best result was obtained with a laser power of 300 W, scanning speed of 700 mm/s and energy density of 71.43 J/mm^3.

Several authors concluded that the laser power has a more dominant effect than the scanning speed. Larimian et al. (2021) [45] found that for the same ED during SLM 316 stainless steel printing, high laser power and low scanning speed significantly increased the mechanical properties compared to those manufactured with low laser power and high scanning speed. This shows that increasing the laser power at low scanning rates contributes to adequate energy for melting the powder particles in the melt pool. It reduces the surface tension and viscosity, favoring flowability of the liquid phase for densification of the material.

De Souza et al. (2019) [26] investigated 4 different scan speeds (600 to 1500 mm/s) in SLM printed 18Ni-300 MS and found that as the scan speed increased, the track width becomes narrower, leading to grain refinement and a dendritic/cellular microstructure due to the higher cooling rate. However, at excessive scan speeds, the scan track turns discontinuous, inducing more shear stress in the material, generating surface tension related effects in the melt pool which lead to ball formation and higher surface roughness. Mugwagwa et al. (2019) [46] also concluded that lower scanning speeds tend to reduce the residual stress of maraging steel parts manufactured by SLM. By keeping the layer thickness at 0.03 mm and laser power at 160 W, and stepping up the scanning speed from 400 to 800 mm/s, the residual stress increased from 158 to 227 MPa.

2.2.1.4 Powder Thickness

The thickness of the powder layer is one of the critical parameters and its microstructure. It is defined from the organized spreading of the powder over the underlying layers to form the selected thickness in which the laser will interact. The thickness is controlled by the position/movement of the recoater distributing the material and the physical characteristics of the material such as density and flowability. The thickness range that can be selected depends on the L-PBF printing machine that will be used, although on the latest printers it can vary from 20 to 100 μm [47].

During the L-PBF process, the thermal energy required to melt the powder that comes from the laser beam is inversely proportional to the thickness of the layer. If the powder layer is thick enough that it is not possible for the energy to penetrate the powder bed, solidification will be incomplete and will lead to voids and pores that reduce the relative density of the printed material [46]. Also, thinner powder layers improve the thermo-fluidity of the melt between the layers from the increased penetration into the layer. However, it can expose the underlying layers to remelting and cooling variations that can alter the microstructure of the material [47]. For the same laser power and scanning velocity, Mugwagwa et al. (2019) [46] found a decrease in relative density from 99.6% to 99.4% when increasing the layer thickness from 30 μm to 45 μm. Bai et al. (2020) [48] also reported an increase in the number of pores and decrease in the densification of the material as the layer thickness increased. For layer thicknesses of 20 μm the relative density was 98.60%, while at layer thicknesses of 50 μm the relative density decreased to 91.63%.

For thinner layers, the cooling rates are higher, which reduces the interdendritic spacing and results in a finer microstructure [26]. Santana et al. (2023) [49] investigated the effect of layer thickness on L-PBF printed 300 maraging steel and concluded that the martensitic cell size increases significantly as a function of layer thickness, due to the high heat dissipated during solidification for thinner layers. Enhanced solidification of the material contributes to obtaining better mechanical properties of the printed samples. As researched by Kempen et al. (2011) [50], the microhardness of L-PBF printed samples decreased with increasing layer size from 30 μm to 60 μm for the same laser scanning speed. For Inconel 718 samples manufactured in SLM, the tensile properties were slightly better for smaller thicknesses in a range from 20 to 50 μm [51]. However, strain failure is still high and residual stress increases for smaller thicknesses. This can be explained by the fast cooling rate and shorter thermal cycles [46]. Kim et al. (2024) [52] recently determined that the optimum L-PBF parameters for 18Ni-300 MS were a layer thickness of 50 μm and an ED of 70 J/mm^3, resulting in a maximum relative density of 99.9% and excellent tensile properties (tensile strength of 1130 MPa and elongation of 10%).

2.2.1.5 Hatching Space

During the L-PBF process, the laser beam makes paths according to the chosen scanning strategy. The spacing between consecutive scan tracks is described as hatch spacing, as representation in Figure 2.7, taken from Hussain et al. (2021) [53]. The hatch spacing is determined based on the distance between the center of consecutive tracks and the width of the melt pool.

What will dictate good solidification of the material from the hatching space parameter is the extent to which the scan tracks/melt pool will overlap relative to each other. A high value of hatch space reduces the overlapping rate of the tracks, and if it is excessive, high gaps will form between the scan lines, so that the powder between the gaps will not be completely melted due to the lack of sufficient energy for the melting. This was confirmed by Mutua

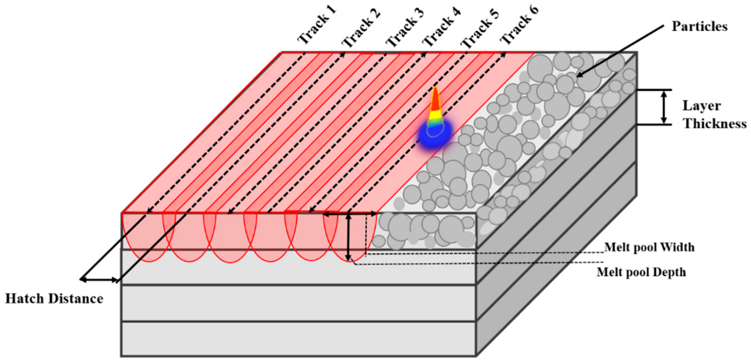

Figure 2.7 Schematic illustration of the hatch spacing representation in L-PBF process [53].

et al. (2017) [41], who varied the hatching space from 2.5 μm to 12 μm and observed an increase in relative density from 97.0% to 99.8%. However, increasing to a hatch spacing of 20 μm resulted in a decrease to 99.5%. Bai et al. (2020) [48] found the same trend of increasing material densification with increasing hatching space. In their study, there was a significant reduction in relative density from 94.65% to 90.53% when increasing the hatching space from 8.5 μm to 12 μm. It is explained that the overlap rate is also dependent on the laser diameter, such that hatching space smaller than the beam diameter would still enable overlaping, abruptly decreasing the relative density.

As explained in Section 2.2.1.2, the ED increases as the hatching space decreases. Therefore, slight modifications to reduce the space between tracks increases the flowability and distribution of the liquid metal, resulting in an increase in relative density. However, excessively small values of hatching space contribute to an increase in the laser's energy density, resulting in vaporization of the material and scattering of the powder, leading to low relative densities [3].

2.2.2 Influence of Powder Characteristics

The physical characteristics of the powder to be used in L-PBF processes also have a critical impact on the quality, homogeneity and mechanical properties of the manufactured components. Powder characteristics mainly depend on the selected material and the type atomization process. The powder characteristics include Particle Size Distribution (PSD), particle shape, chemical composition, internal porosity, and the presence of impurities and inclusions [47]. These powder properties affect their processability in the different MAM techniques and will impact the packing density, powder spreading and flowability (which define the rheological properties of the powders [14]).

The powder morphology dictates how the interconnection between each particle will be established. It also impacts the formation of voids upon powder melting [30]. The formation of these voids is also influenced by the penetration of the laser energy from the surface of the printed material to its bulk. The amount of transferred energy is intrinsically linked to the laser reflection and energy absorption by the powder, leading ultimately to the formation of a melt pool [54]. For large powder size, the laser penetration is weakened, which can lead to voids and poor particle adhesion during the material solidification. When the particle size is small, there is a greater propensity to agglomeration and friction which reduce the flowability of the powder [27]. In fact, an optimal powder size distribution is required to maximize the powder packing density. It is typically obtained by combining coarse and fine powders. Packing density affects laser penetration and thermal conductivity [54]. Low packing density leads to voids and pore defects in the powder bed. This was demonstrated by Abd-Elghany and Bourell [55] which found better tensile strength for higher packing density values of L-PBF-printed 304L stainless steel samples. Typical particle sizes used in these processes range from 10 to 60 μm [56].

In L-PBF processes, the powder packing density is related to its flowability during the powder layer spreading stage. According to the ASTM B213 standard [57], the flowability of the powder is measured using a standard funnel technique, such as a Hall-funnel, which has a wall angle of 60^o and an orifice diameter of 2.5 mm. Alternatively, there is another technique that involves the use of an equipment that analyzes the avalanche angle of the powder flowing in a rotating drum. In both techniques, the PSD and the particle shape directly influence the powder flowability. Spherical particles improve the flowability when compared to angular, satellite or irregular shape particles [58]. It is to be noted that smaller particle sizes improve both the relative density upon solidification and the surface quality since they are easier to melt (larger surface-to-volume ratio) [30]. Larger particle sizes typically lead to better tensile properties and hardness, but lead to poor printing repeatability [54].

Key characteristics of the powder to be printed vary according to the statistical distribution of particle size resulting from a given atomization process [54]. There are several methods for producing atomized powder which will impact the powder morphology, chemical composition and presence of defects. These methods include water atomization, gas atomization, plasma atomization and electrode induction-melt gas atomization [56]. For gas atomization processes, the powder particle shape is more spherical and its chemical composition is more uniform compared to a powder that is produced by water atomization. Inert gas atomization also produces denser particles. Irregular shape particles with higher oxygen concentration and surface oxide-skin produced by water atomization lead to more porous printed samples [31]. For all these reasons, monitoring batch quality is of utmost importance in order to avoid irregular morphologies, excessive particle sizes, impurities and entrained gas. For some alloyed powders (such as maraging steel), it is possible to recycle the excess powder while maintaining excellent mechanical properties of the printed parts (see for example the study Sun et al. (2021) [59] where they reused some powder material for 113 building cycles). However, care must be taken to avoid excessive exposure to air (which leads to powder oxidation), as well as the presence of impurities and contaminants that could adversely affect the printed material mechanical performance [30].

2.3 Maraging Steel

Maraging steel belongs to the class of ultra-high strength steels, developed using low carbon content and substitutional alloying elements to achieve precipitation strengthening. Its nominal chemical composition depends on the concentration of Ni (15-25%) and other alloying elements, with the carbon content limited to about 0.03% [7]. This composition promotes the formation of a soft martensitic matrix that can be hardened with post aging heat treatment. The soft martensite matrix contributes to easier machining operations, while the aging heat treatment promotes the formation of nanoprecipitates that inhibits the movement of dislocations in the martensitic microstructure upon mechanical loading [60]. The coupled effect between the martensitic matrix and the strengthening precipitates formed during the “aging treatment” (which material process gives the name “maraging” steel) produces a steel with high strength and good fracture toughness. This combination of mechanical properties is particularly suitable for injection mold tooling [56] as well as high-performance aircraft part applications (i.e. landing gear, structural chassis for helicopters, casings for rocket propulsion engines) [60].

There are several maraging steel grades on the market that can be used in MAM: the most common are 18Ni-300, 18Ni-250 and 18Ni-200. These grades vary in their content of Cobalt (up to 9% by weight) and Molybdenum (up to 5% by weight) as shown in Table 2.1. These two alloying elements contribute to the formation of intermetallic precipitates. More specifically, Co reduces the solubility of Mo in the martensitic matrix, promotes the formation of Ni_3Mo and Fe_2Mo precipitates, and ensures a uniform dispersion of these precipitates in the matrix. However, due to the scarcity and rising cost of Co, new Co-free maraging steels are being developed in an attempt to maintain the same mechanical properties by increasing the amount of Titanium instead. Also, Titanium is an essential alloying element, as it contributes to the formation of Ni_3Ti, or if combined with Aluminium (Al), to the formation of Ni_3Al and $Ni_3(Ti,Al)$ precipitates [7]. The beneficial effect of these alloying elements (i.e. Ni, Mo, Co and Ti) coupled to the absence of interstitial alloying elements (especially a low carbon content) makes maraging steel high mechanical strength materials which are suitable for welding and additive manufacturing processing.

Table 2.1 Nominal compositions of commercial maraging steels [2].

Standard grades	C (wt%)	Ni (wt%)	Mo (wt%)	Co (wt%)	Ti (wt%)	Al (wt%)
18Ni(200)	max 0.03	18	3.3	8.5	0.2	0.1
18Ni(250)	max 0.03	18	5.0	8.5	0.4	0.1
18Ni(300)	max 0.03	18	5.0	9.0	0.7	0.1
Cobalt-free 18Ni(200)	max 0.03	18.5	3.0	-	0.7	0.1
Cobalt-free 18Ni(250)	max 0.03	18.5	3.0	-	1.4	0.1
Cobalt-free 18Ni(300)	max 0.03	18.5	4.0	-	1.85	0.1

Iron-based maraging steel contains a relatively high Ni concentration (i.e. about 15 wt. %), which allows martensite to form under relatively low cooling rates. Thus, martensite in maraging steels is formed by cooling the material from the austenitizing temperature [7]. The solid austenite phase forms towards the center of the melt pool, between the solid and the liquid phase (i.e. the melt pool boundary). This solidification increases in response to the heat flow generated in the melt pool, causing the solidified austenite grains to be oriented in the [001] direction due to rapid cooling. At temperatures below the initial martensite start temperature (around 200 ℃), these solidified grains transform into a lath-shaped martensitic structure (see Figure 2.8). As a result of the high heat flow and rapid solidification at the melt pool boundaries, retained austenite can be formed mainly at this interface rather than inside the melt pool [61].

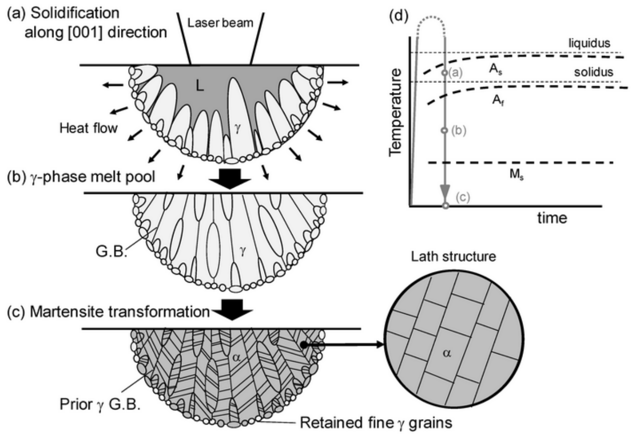

Figure 2.8 Schematic illustration of (a-c) formation process of microstructure and (d) schematic thermal history in L-PBF maraging steel [61].

Thus, the main constituents of the microstructure of maraging steel produced by L-PBF techniques exposed to aging treatments include lath martensite, nanoprecipitated intermetallics (such as Ni_3Mo, Ni_3Ti, Ni_3Al, Fe_2Mo_3), retained austenite (which remains after cooling from solution annealing temperatures) and reverted austenite (which is the reversion of martensite into austenite depending on composition and heat treatment) [7].

The energy transfer between the laser beam and the powder layer results in the formation of a melt pool. Subsequent heat transfers trigger heating/cooling phenomena and temperature gradients in the subsequent printed layers that impact the formation of microstructural heterogeneities. The solidification process (starting with the grain nucleation and growth), occurs in the direction of the heat flow. Elongated grains with a dendritic/cellular structure usually tend to form from the melt pool boundary towards the center due to heat loss. Depending on the thermal gradient, there is a shift from thin to coarse cellular structures [62]. Overall, these microstructural features (including grain orientations) depend directly on the selected L-PBF process parameters [42].

Since martensite transformation deviates significantly from an equilibrium phase transition, the effects of the various alloying elements on its driving force formation are not easily predicted from classical thermodynamics and need to be experimentally measured. Many studies [63–65] indicate that Ni, Mo, and Ti alloying elements in extra-low carbon steels reduce the martensite transformation temperature (M_s) and provide high austenite stabilization in cell boundary regions. The fine grain size characteristic of the rapid solidification of the L-PBF process also contributes to a reduction in M_s and thus more austenite retention [63]. Thus, up to around 10% retained austenite can be present in as-printed maraging

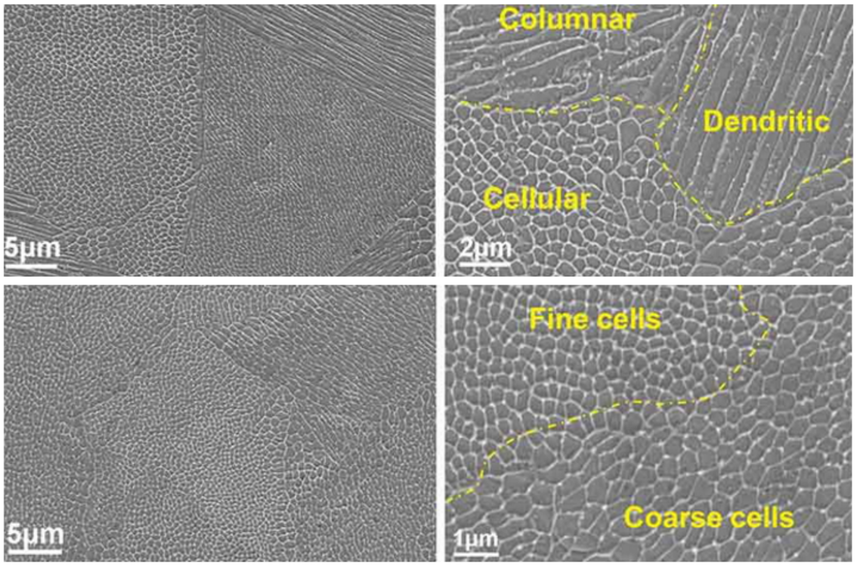

Figure 2.9 Representative SEM images taken from the horizontal (top panels) and vertical (bottom panels) cross-sections of as-built 18Ni-300 MS manufactured by L-PBF. The optimized printing parameters were P = 285 W, v = 960 mm/s and h = 110 μm, respectively [62].

steel samples [7]. The typical microstructure of L-PBF maraging steel is constituted of a fine cellular structure, columnar grains, dendritic structures and residual retained austenite [62] as presented in Figure 2.9).

Due to the potential solute micro-segregation, mechanical response anisotropy and residual stresses inherent of the L-PBF process, post heat treatments become imperative [7]. They allow to homogenize the martensitic matrix and to increase the fraction of intermetallic precipitates in order to achieve peak mechanical strength. The various heat treatments used in the industry for maraging steel processed by L-PBF will be discussed in the next section.

2.3.1 Post Processing Heat Treatment

The heterogeneities of the non-equilibrated microstructure obtained as a result of the fast solidification rate experienced during the L-PBF process lead to non-optimal strength and ductility when compared to conventional maraging steel parts. The presence of a homogenized martensitic microstructure with an optimal density of precipitates and retained/reverted austenite will depend on the chemical composition of the maraging steel as well as the heat treatment conditions.

In commercial processes, heat treatment consists of a first austenitizing step in which the material is heated to temperatures between 780 and 1020 °C for 1 hour per 25 mm section of the part. The material is then quenched to room temperature to avoid unprocessed austenite [2]. Due to the high Ni and low carbon content, the formation of ferrite and pearlite is inhibited which contributes to the formation of austenite in the Fe-Ni martensitic matrix with a fine-grained cubic lath martensite. This martensite is arranged in the form of several packets of laths parallel to each other. Thus, unlike carbon steels which form hard martensitic matrix, maraging steels form a relatively soft and ductile martensite which can be more easily machined [7]. High Solution Treatment (ST) temperatures are imposed to homogenize the distribution of alloying elements and to eliminate solute segregation. In L-PBF process, the presence of cellular structures and melt pool boundaries in the microstructure tend to disappear with such heat treatments [5]. As the temperature is increased, more cellular structures are eliminated. Nevertheless, the remaining phases consist of a high volume of fine lath martensite with residual retained austenite, which can even be reduced or decomposed after ST [3, 7].

After the Solution Treatment, the alloy undergoes an Aging process, which combined are called Solution Treatment + Aging (STA), at temperatures of around 450 to 560 °C for periods of 3 to 9 hours and then cooled in air. This promotes micro-segregation and facilitates the formation of reverted austenite as well as the precipitation of a high density of intermetallic nanoparticles such as Ni_3Ti. Depending on the chemical composition of the Fe-Ni maraging alloy and aging temperatures, Ti may be replaced by Al and Mo, forming intermetallics such as Fe_2Mo, Ni_3Al and $Ni_3(Ti,Al)$ [3]. These nanoprecipitates have different shapes such as 1) plate shape with a length of 9 to 22 nm, 2) needle shape or 3) spherical shapes with diameters of around 5 to 9 nm [3]. Tan et al (2018) [62] found needle-shaped Ni_3X (X= Ti, Al, Mo) nanoprecipitates with a diameter of 6-10 nm and a length of 15-50 nm in maraging steel processed by L-PBF after aging. The dimensions of these intermetallics can be modify by the aging treatment temperature and duration. A high density of nanoparticles is formed at temperatures below 500 °C. As the temperature or ageing time is increased, these nanoparticles get coarser until they dissolved in the matrix at temperatures above 590 °C [66]. This dissolution causes the Ni content to increase in the surroundings of the martensitic matrix.

The precipitation kinetics of these intermetallics are favored at aging temperatures up to 485 °C. Such aging treatments lead to a hardening of the alloy which reaches peak strengths before the austenite reversal reaction takes place. As the aging temperature is increased, the volume of reverted austenite becomes greater than the volume of retained austenite. Tan et al. (2018) [62] investigated the phase transformation of as-printed maraging steel using Differential Scanning Calorimetry (DSC) curves and concluded that there is an exothermic peak at around 456 °C related to the recovery of martensite and the precipitation of intermetallic phases, as well as a peak at around 572 °C which represents grain growth or the formation of austenite. After this temperature, there is a phase transition from martensite to austenite and a dissolution of the intermetallic precipitates.

2.3.2 Direct Aging Treatment

Unlike wrought maraging steels for which the industry has accepted standard heat treatments, L-PBF printed maraging steels still lack consensus on the heat cycle to be applied. This is mainly due to the fact that these heat treatments will depend on the L-PBF process parameters (since they modulate the presence of microstructural heterogeneities and elemental micro-segregations). Thus, several heat treatment conditions and cycles can be imposed to obtain distinct microstructures and resulting mechanical properties. The most common cycles are ST as well as STA treatment. Moreover, a novel thermal treatment cycle called DA is currently being studied in the literature and is the main topic of this research project. DA removes the ST stage, reducing the material processing lead time, while maintaining similar or even enhanced mechanical properties.

The final microstructure of the maraging steel is quite different whether DA or STA heat treatment is applied. Under DA conditions, Bai et al. (2019) [67] found that as the aging temperature increased the strip and the melt pool became blurred in the intercellular regions. Above 520 °C, the boundaries of the melt pool are dissolved and beyond 560 °C the cellular structures are almost broken. For STA samples, the martensite laths become fuzzy and they gradually disappear when the temperature reaches 560 °C. The phase assemblage of the printed material can also be altered by the applied heat treatment. Osman et al. (2023) [5] applied DA treatment at a temperature of 490 °C for 6 hours to 18Ni-300 MS samples printed by L-PBF. They found an increase from 9% to 13% in volume of austenite content due to the reversion of austenite stabilized by Ni micro-segregation. ST and STA samples exhibited nearly full martensitic microstructures. Tekin et al. (2023) [68] also reported on the phase fractions for different heat treatment. They observed an increase in the austenite content (in volume) from 3.4% in 18Ni-300 MS as-printed to 8.5% after aging at 490 °C for 6 hours. In STA, the austenite content decreased to 2.6%.

The selected DA temperature impacts both the type and density of nanoprecipitates present in the microstructure as well as the amount of retained/reverted austenite. For temperatures betwen 390 °C and 450 °C (a treatment called under-aging), cellular structures similar to as-printed with the presence of intermetallic precipitates are observed. For DA temperatures between 530 °C and 700 °C (a treatment call over-aging), a microstructure with thick boundaries and a high volume fraction of austenite is produced. Under these conditions, cellular structures disappear and the formation of Fe_2Mo is favored as seen on Figure 2.10. This process contributes to the reversion of martensite to austenite [66].

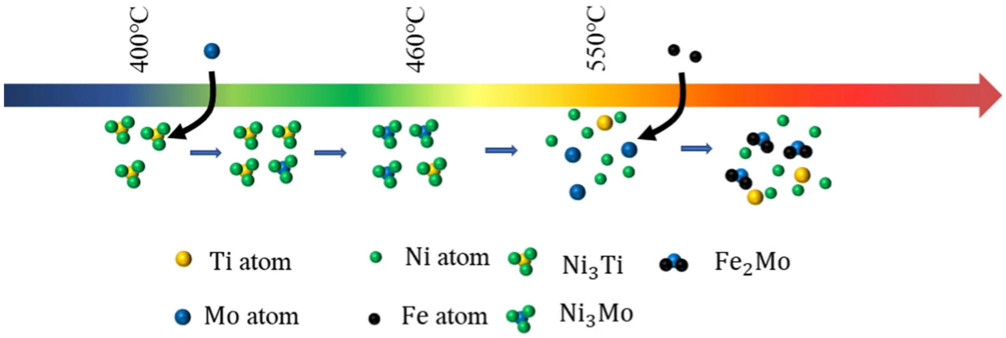

Figure 2.10 Types of intermetallics which precipitate as a function of the aging treatment for AM maraging steel [69]. Reproduced with permission from Springer Nature.

Martensite-to-austenite reversion occurs in specific regions such as cell boundaries, where high pre-existing concentrations of austenite-stabilizing elements are present. Thus, cell boundaries act as preferential sites for austenite nucleation and growth since segregation of Ni, Ti, and Mo increases austenite stability [64, 65]. With direct aging heat treatment, austenite reversion occurs predominantly from the expansion of retained austenite at cell boundaries, promoting rapid and partitionless growth of austenite throughout such sites [64]. Feitosa et al. (2024) [70] studied the competitive or cooperative interaction of reverse austenite and nanoprecipitates in 18Ni-350 maraging steel. They concluded that as the aging treatment occurs, austenite increases around the precipitates as they coalesce and partially dissolve. Overall, the final austenite volume fraction depends on the conditions of the direct aging heat treatment. As an example, Bai et al. (2019) [67] found that the initial austenite composition of a 18Ni-300 MS printed part by SLM was 6.2%. The amount increased to 8% at a DA temperature of 480 °C and reached 17.9% at a DA temperature of 560 °C. When setting the DA temperature to 520 °C and varying the holding time from 0 to 12 hours, these authors found that there is an increase in the austenite fraction as the holding time is extended. However, after 6 hours, there is no significant increase in the amount of austenite, concluding that aging time has a less significant impact on the microstructure compared to the aging temperature [67].

Yao et al. (2023) [64] studied the role of cellular structure in the reversion of austenite in maraging steel part built with SLM. Figure 2.11 taken from their study shows how the reversion of austenite occurs with or without retained austenite, based on 'in-situ' EBSD, SEM and TEM observations for undeformed and deformed samples that were directly aged at 480°C for 1 hour. It is noted that retained austenite plays a key role in the rapid cellular reversion. Also, the increase in Ti and Mo concentration in the cell boundary regions may act as an energetic driving force for the austenite growth. Thus, such chemical heterogeneities between boundary and interior regions may be indicative of austenite stabilization as direct aging occurs [64].

Santana et al. (2025) [71] studied two direct aging temperatures (i.e. 480°C and 540°C) on the behavior of solute migration to austenite regions. It was concluded that the higher the DA temperature, the greater is the Ni enrichment at the cell boundaries and the less Mo segregation is observed. Such elemental enrichments in these regions enhance the stability of austenite, acting as a soft phase that hinders crack propagation. However, if not properly tuned, it can quickly transform into hard new martensite that aids crack propagation [65]. **Thus, the study of various DA heat treatments will contribute towards a better understanding of the austenite stability and the improvement of mechanical performance of L-PBF parts.** The exploration of optimized DA heat treatment conditions was performed by Yin et al. (2018) [66]. They concluded that an aging treatment of 490 °C for 3 hours achieved peak mechanical strength for SLM maraging steel. Their finding reveals that temperatures above or below this optimal condition may impair the strength properties of the material since there may be an increase in reverse austenite

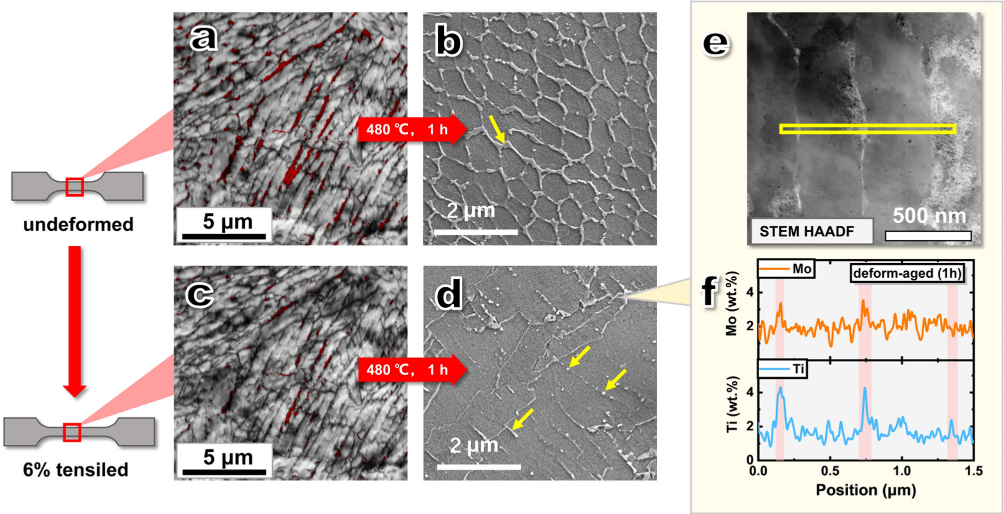

Figure 2.11 EBSD map images of (a) undeformed SLM-fabricated 18Ni-300 MS sample and (c) deformed SLM-fabricated sample (6% engineering tensile strain) from the same region as (a). SEM images of (b) undeformed and (d) deformed samples after direct aging at 480°C for 1 hour. Austenite grains are illustrated by yellow arrows. (e) TEM images of deformed sample after direct aging for 1 hour. (f) Distribution of Ti and Mo within the yellow rectangle in (e) [64].

and the presence of different precipitates in the microstructure. The temperature of 490 °C shows a balance of high nanoprecipitate density and low volume fraction of reverse austenite formation, which allows for maximum mechanical strength values. The following section will discuss the mechanical properties of 18Ni-300 MS alloys under different heat treatment conditions.

2.4 Mechanical Properties of AM maraging steel Printed Parts

2.4.1 Tensile Properties

The average values for Yield Strength (YS) and Ultimate Tensile Strength (UTS) for as-built 18Ni maraging steel processed by AM are around 926 MPa and 1110 MPa respectively [7]. When applying a solution treatment at 820-840 °C for up to 2 hours, these tensile properties can reach values in the range of 950-1080 MPa with Elongation (El) of around 10-14%. Moreover, this heat treatment reduces residual stress and eliminates cellular, columnar structures and melt pool boundaries, facilitating the movement of dislocations [3]. For samples exposed to a solution treatment (815-840 °C for 0.5-2 hours) + aging (460-500 °C for 4-8 hours), the ultimate tensile strength increase to around 1800 to 2160 MPa while the elongation is reduced to 1.50-5.60%. By comparison, DA treatment at 460-500 °C for 3-12 hours allows to maintain the UTS around 1726-2217 MPa while decreasing the production lead time of the material [3]. In this case, the elongation reaches values between 1.3% to 8.3%, which is slightly lower than conventional alloys (such alloys typically reach on average 7% elongation [2]). Figure 2.12, taken from Guo et al. (2022) [3], shows the elongation vs UTS relationship for several 18Ni-Maraging steel grades for different heat treatment approaches and those conventionally produced after STA treatment.

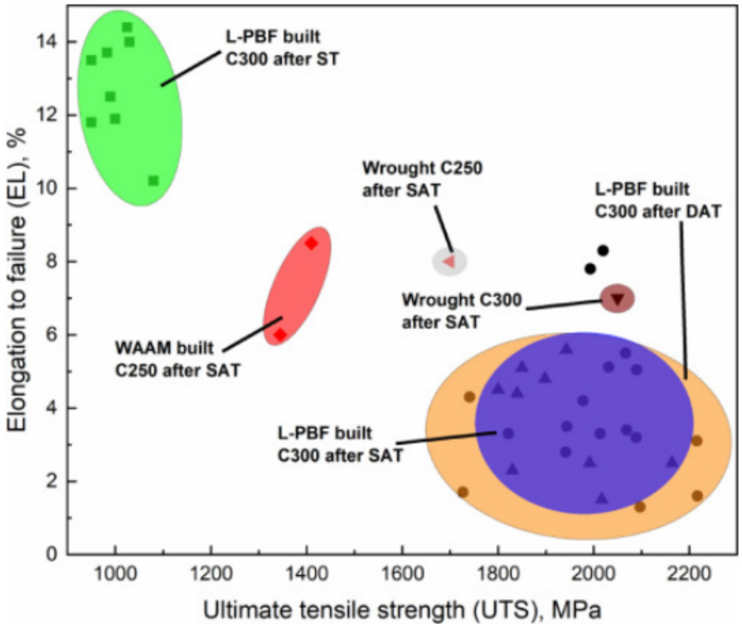

Figure 2.12 ELxUTS relationship of L-PBF and Wire Arc Additive Manufacturing (WAAM) 18Ni-Maraging steel grades after post-processing heat treatments and those of conventionally produced alloys after STA treatment [3].

Figure 2.12 illustrates how the heat treatment applied to maraging steels needs to be properly selected in order to reach optimal tensile properties of the printed component in service. In general, the strategy is to produce a material with high mechanical strength while maintaining good ductility and a uniform microstructure. One ultimate objective is also to shorten production cycle time. Tekin et al. (2023) [68] printed 18Ni-300 MS by L-PBF and attempted to compare the two heat treatment approaches, i.e. STA (820 °C for 1 hour + 490 °C for 6 hours) and DA (only 490 °C for 6 hours). Their results showed a ductility which is 70-80% higher for DA treatment compared to STA at the expense of a reduction in tensile strength of around 5%. This is due to the formation of retained austenite and reverted austenite during the direct aging process. The presence of reverted austenite, formed during the aging treatment, has a beneficial effect on the mechanical toughness of maraging steels. During plastic deformation, when uniaxial tension is applied, a TRansformation-Induced

Plasticity (TRIP) effect occurs. This effect transforms the reverted austenite into fresh martensite. TRIP steels also benefit from the dynamic Hall-Petch effect which promotes deformation-induced grain refinement. These new grain boundaries acts as obstacles to the movement of dislocations [72]. Thus, as plastic deformation progresses in the material, new martensite is formed by the TRIP effect. This martensite has less defects and precipitates. As a result, the material can absorb more strain energy which enhances ductility while increasing strength through grain refinement [5].

The TRIP mechanism is impacted by factors such as the grain size and the Stacking Fault Energy (SFE) of the austenite, the strain rate and the volume fraction of phases [72]. A mechanical response of maraging steels is only effective when there is sufficient stable austenite to trigger the TRIP effect as well as enough time to accommodate for the deformation. The volume fraction of reverted austenite is controlled by the temperature and duration of the aging treatment [5]. **It is therefore necessary to investigate the best thermal conditions to heat treat maraging steel in order to tune the martensite-to-austenite volume ratio to obtain high strength while achieving good ductility.**

Bai et al. (2019) [67] investigated different temperatures and durations of ST, STA and DA treatments for L-PBF printed maraging steel. DA treatments were explored within the range of temperature between 400 to 560 °C for 6 hours. These authors found that for DA heat treated samples, there is an increase in strength due to the presence of intermetallic precipitates. As the aging temperature increases, the strength decreases as a result of the growth of these precipitates which become too large. The increase in austenite volume with aging temperature improves elongation but reduces tensile strength. The optimal heat treatment condition according to these authors was the DA at a temperature of 520 °C for 6 hours. It led to a ultimate tensile strength of 2126 MPa and an El of 6.5%. In order to better visualize all the data found in the literature related to the aging treatment applied to AM maraging steels, Figure 2.13 reports the UTS (a) and elongation (b) data values for direct aging treatment temperatures applied for 5-6 hours.

From this figure, it can be noticed that most of the literature focuses on aging temperatures between 480 to 500 °C. This is a temperature which allows peak strength performance through the presence of a high density of nanoprecipitates in the microstructure. On the other hand, very limited attention has been given to temperatures above 500 °C up to 560 °C, aiming to achieve optimum relationship between UTS and elongation, based on the presence of nanoprecipitates combined with reverted austenite content capable of triggering TRIP mechanisms during mechanical loading. **For maraging steel, a good ductility of the material at the expense of a low variation in strength would be of interest**

for injection molding part applications which require energy absorption upon operation.

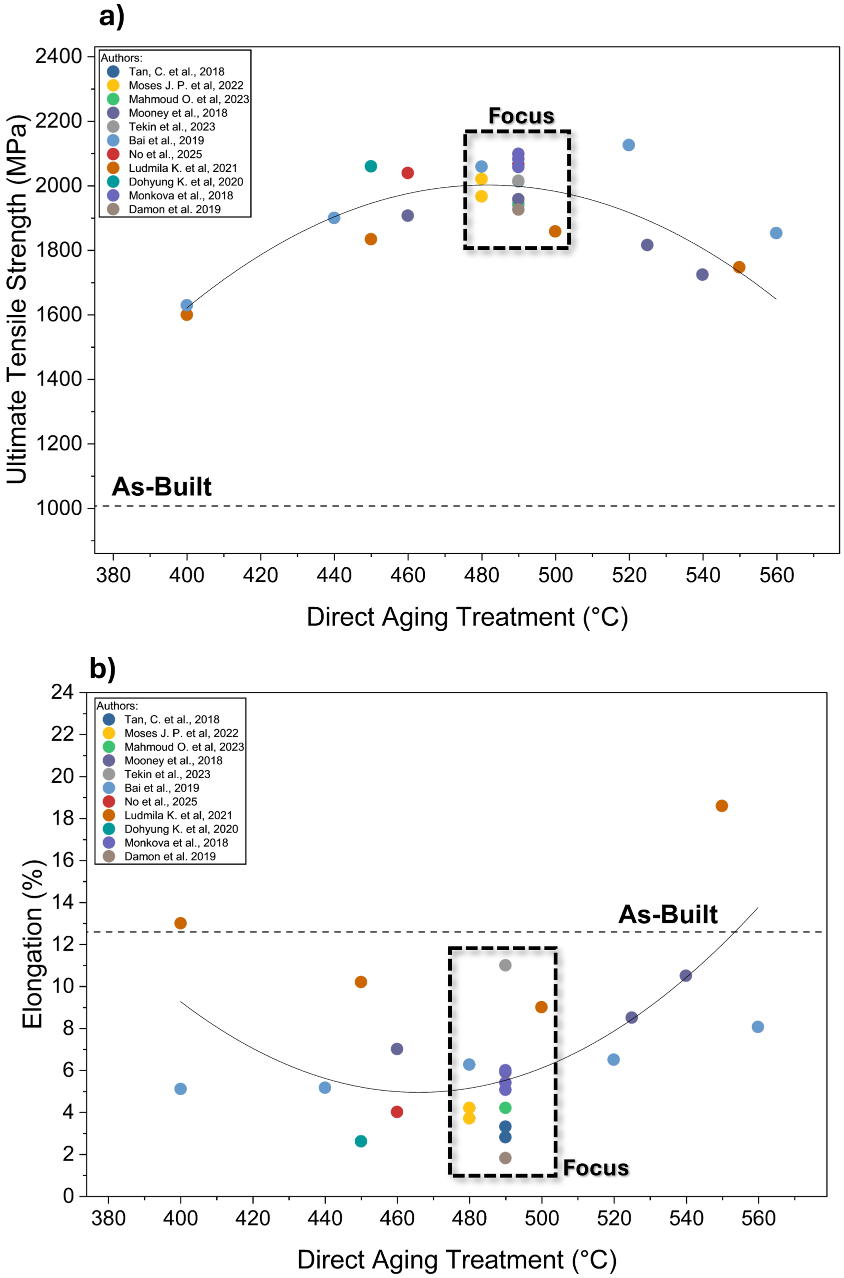

Figure 2.13 Graphs a) shows the UTS data values (MPa) and b) the elongation data values (%) for AM maraging steel after direct aging treatment between 400 °C and 560 °C for 5-6 hours [4, 5, 38, 62, 67, 68, 73, 74]. Black dashed line refers to literature research focus. Solid black line corresponds to polynomial fitting.

2.4.2 Hardness

As for all the other mechanical properties, the hardness of maraging steel components manufactured by L-PBF is directly related to the process parameters. Densification plays an important role in achieving high and consistent hardness. The average hardness values for as-printed 18Ni-300 MS are in the range of 350 Hardness Vickers (HV) to 400 HV [7]. Different build printing orientations can exhibit high variations in hardness for the same process parameters. Post heat treatments contribute to homogenizing the microstructure resulting in a more uniform hardness distribution [3].

After solution treatments, the hardness tends to decrease to values around 262 HV as shown by Tan et al. (2018) [62]. These authors performed a ST at 840 °C for 1 hour. A subsequent aging treatment at 490 °C for 6 hours leads to a significant hardness increase of up to 589 HV. In fact, the literature shows an increase in hardness with aging treatment to values around 600 HV depending on the temperature and duration parameters [7]. Bai et al. (2019) [67] performed DA and STA treatments at different temperatures and durations for L-PBF-printed maraging steels. They noticed that there is a significant increase in hardness at temperatures between 480 °C to 520 °C, reaching a peak hardness of 653 HV when applying a DA heat treatment at 520 °C for 6 hours. Beyond this temperature, the microhardness decreased to 580-560 HV due to the presence of soft reverted austenite. They also concluded that the solution treatment on STA samples has practically the same effect on hardness compared to DA samples, showing additional evidence that this step is not significant for the tuning of the mechanical properties. The hardness values for L-PBF maraging steel parts vary between 549-746 HV for DA treatments and between 531 to 649 HV for STA treatments [3]. Higher aging temperatures tend to reach peak hardness for shorter aging times. At high temperatures and high aging times, hardness tends to continuously decrease due to the intermetallic dissolution and the reversion of austenite [7]. These hardness values are close to the ones of conventional steels after standard heat treatment, which vary between 505 and 649 HV [3].

2.4.3 V-Notch Charpy Impact Test

The toughness of maraging steels is an important mechanical property for many industrial applications to avoid catastrophic failures. It relates to the energy absorption of the material during multi-axial impact loading applications at high velocity rates. In some instances, it can be evaluated at low or high temperatures, which is of prime importance for example in injection mold part applications. The absorbed energy can be measured using Charpy and Izod tests according to the ISO 148-1 [75] and ASTM E23 standards [76]. In these tests, the specimen is strategically placed in the apparatus to receive the blow of a moving mass. The transferred energy of the moving mass needs to be sufficient to fracture the specimen in the presence of a notch. The instrument then measures the energy absorbed as a result of the fracture of the notched specimen.

As already reported in Table 2.1, maraging steels have a low C content combined to high Ni, Mo and Co concentration that allow to reach high mechanical strength after optimal heat treatment. This is because a high volume of nanoprecipitates in the martensitic microstructure combined with small fraction of austenite at the peak strength is obtained. Such a heat treated microstructure has a reduced elongation values which also affect the toughness of the material. As a reference point, the 18Ni-250 maraging steel cast by vacuum induction and solution heat treated at 815 °C for 1 hour followed by an aging treatment at 480 °C for 5 hours, has an Charpy impact energy at room temperature of 37 Joules [2]. For maraging steels produced by AM, process parameters such as ED and build direction directly influence their toughness. The densification of the material is also extremely important for this property. Hatos et al. (2024) [77] found that as-built maraging steel L-PBF specimens produced with a laser power of 150 W, scanning speed of 600 mm/s and ED of 125 J/mm^3 reach 99.97% density and 119 J of absorbed energy at room temperature. Specimens with high level of porosity (as a result of the use of non-optimal process parameters) had the lowest absorbed energy values, reaching only 10 J [77]. This provides evidence that porosity is one of the most important microstructural features that influence the toughness of additive manufactured parts.

Typically, there is a decrease in the absorbed energy values from as-built to heat-treated maraging steels because of the increase of mechanical strength. Tan et al. (2018) [62] investigated the Charpy impact energy of a 18Ni-300 MS in as-built and heat-treated conditions. They obtained an impact energy value of around 67.5 J coupled with a high anisotropy for the as-built state. After a heat treatment at 490 °C for 6 hours, the absorbed energy drastically dropped to 13.8 J with reduced anisotropy. Kempen et al. (2011) [50] did the same investigation and obtained values of 42 J for as-built and 6 J for treated samples at 490 °C for 5 hours. Figure 2.14 shows the Charpy impact energy at room temperature found in the literature for different temperatures of direct aging (DA) treatment applied to AM 18Ni-300 MS samples for 5 to 6 hours.

From this figure, it can be seen that the most commonly studied direct aging temperatures are between 480 to 500 °C. This is the temperature range where the Charpy impact energy is the lowest. This is due to obtaining a peak strength coupled to a poor ductility. Bai et al. (2019) [67] analyzed different direct aging temperatures (i.e. 400-560 °C) for 6 hours.

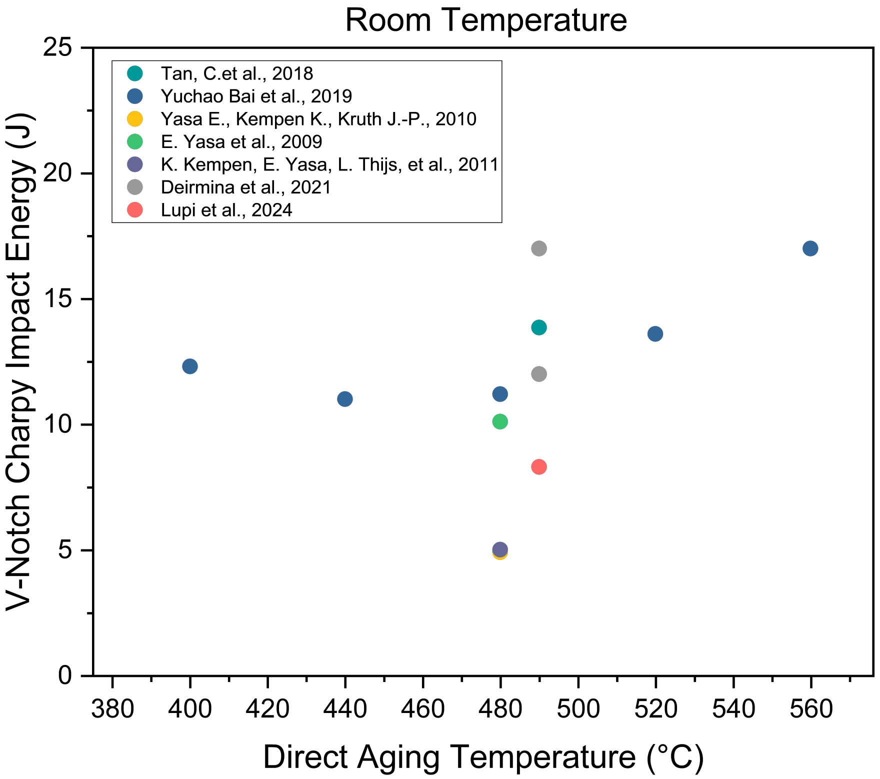

Figure 2.14 Effect of Direct Aging (DA) treatment for 5-6 hours on the Charpy Impact Energy of 18Ni-300 MS at room temperature [50, 62, 67, 78–81].

They observed that the impact toughness decreased from around 12.5 J to 11.2 J as the heat treatment temperature is increased from 400 to 480 °C. As the temperature further increased to 560 °C, the energy absorption reaches a high value of 17 J. This can be explained by the fact that for a DA treatment at 490 °C, there is a high density of intermetallic nanoparticles that reduce the ductility of the material, leading to a lower toughness value. As the temperature increases, the nanoparticles become coarser and dissolve while the austenite reverses, positively contributing to the material impact toughness.

It is clear that the existing literature focuses on impact tests at room temperature since the impact toughness tests are relatively simple and easy to make in these conditions. **There has been limited focus on the impact toughness behavior of maraging steels manufactured by additive manufacturing at low or high temperatures, which is of utmost importance for several applications (such as injection molding parts and aerospace applications).** The Ductile-Brittle Transition Temperature (DBTT) behavior for AM-printed 18Ni-300 MS has not been found in the literature. It is therefore essential to develop DBTT behavior curves for both as-built and post-heat-treatment conditions, especially for direct aging heat treated samples. By applying different DA temperatures, the behavior of the DBTT curve will be influenced by the presence of intermetallic nanoparticles as well as the reversion of austenite. Tuning DA temperatures between 500 °C and 560 °C could be crucial for achieving higher toughness responses at critical temperatures without excessively degrading mechanical strength, making it a great solution for several applications.

CHAPTER 3 RESEARCH OBJECTIVES

3.1 Main Objective

The main objective of this project is **to explore the impact of direct aging treatment (490 °C, 510 °C, 530 °C, and 560 °C for 6 hours) on the tensile properties and impact toughness behavior of 18Ni-300 Maraging Steel produced by Hybrid Additive/Subtractive Manufacturing.**

3.2 Specific Objectives

Here are the specific objectives of this project:

- Manufacture 20 rectangular prismatic-shaped coupons using the Laser Powder Bed Fusion technique under optimized process parameters to obtain high-density parts.
- Perform direct aging treatment at different temperatures of 490 °C, 510 °C, 530 °C, and 560 °C for 6 hours to modulate the microstructure of 18Ni-300 maraging steel according to the imposed conditions.
- Characterize the bulk density of the as-printed sample to verify the relative density according to the optimized parameters for the L-PBF process.
- Quantify the phases present in the as-built samples and for all directly aged conditions based on X-ray Diffraction analysis.
- Characterize the microstructure of as-built and aged samples by relating and quantifying the presence of austenite and the features present in the matrix according to the applied aging temperature.
- Perform room temperature tensile tests on triplicate as-built specimens and all imposed aging conditions.
- Characterize local surface deformations just before fracture for As-Built and aged samples.
- Perform V-notch Charpy impact tests at different test temperatures for all conditions studied in this project and develop a ductile-brittle transition temperature (DBTT) curve for each imposed condition.
- Characterize the tensile and impact Charpy fractography surface after specimen rupture.

CHAPTER 4 MATERIALS AND METHODOLOGY

This section defines the specifications of the powder material as well as the methodology applied for the manufacturing of 18Ni-300 maraging steel (18Ni-300 MS) printed parts using a hybrid additive-substrate manufacturing technique. In addition, it provides details on the direct aging heat treatment processes performed and the subsequent characterizations and mechanical tests conducted. Figure 4.1 below describes the applied methodology of this master's project, highlighting the main steps that comprise the L-PBF manufacturing and the heat treatment selected to reach the research objectives.

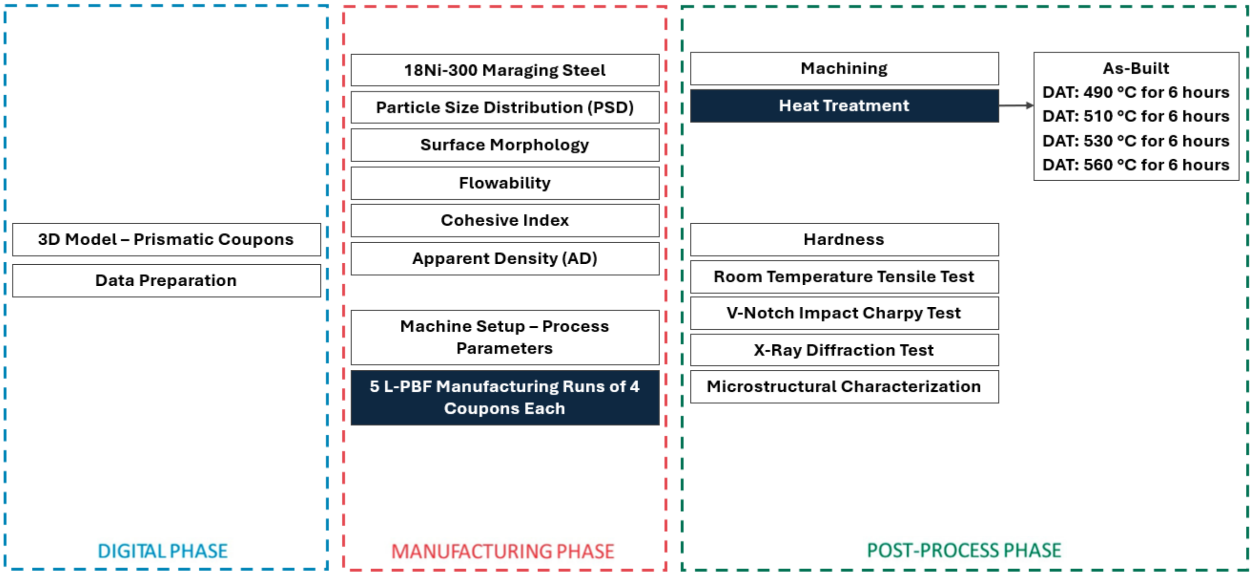

Figure 4.1 Schematic diagram illustrating the sequence of steps applied in the project according to the main phases of L-PBF manufacturing.

This methodology was developed in collaboration with the National Research Council of Canada (NRC-CNRC). NRC provided the materials, consumables and most of the equipment required for this project, as well as the staff's expertise regarding the L-PBF manufacturing equipment, heat treatment furnace, tensile testing equipment and sample characterization equipment.

4.1 Materials

The 18Ni-300 maraging steel powder used in this project was supplied by Sandvik Osprey. It was atomized with inert nitrogen gas, achieving a powder particle size between 50

μm and 20 μm. The batch provided was Nº 24D0446, with the chemical composition (wt%) shown in Table 4.1 below:

Table 4.1 Chemical composition (wt%) of 18Ni-300 maraging steel powder used in the present project.

Element	Composition (wt%)
C	0.01
Ni	17.9
Co	8.9
Mo	5.0
Ti	0.8
Cr	0.2
Al	0.10
Si	0.07
Mn	0.05
O	0.04
N	0.03

The particle size distribution of the powder measured by Sandvik from a Malvern Mastersizer laser diffraction analyzer resulted in a D10 (10th percentile) of 21.8 μm, D50 (median) of 33.1 μm and a D90 (90th percentile) of 50.2 μm. An additional characterization of PSD was carried out in this project to validate the particle size distribution employed during the manufacture of the parts, since there could be humidity retention or PSD inconsistencies after handling and shipping operations of the powder. The PSD of the powder was measured in this work using a NANOTRAC FLEX Nanoparticle Size Analyzer based on the dynamic light scattering technique. This powder analysis resulted in a D10 (10th percentile) of 23.45 μm, a D50 (median) of 33.63 μm, and a D90 (90th percentile) of 53.24 μm. The PSD was therefore similar to the one provided by the supplier showing a relatively large particle size batch.

The surface morphology of the powder was characterized using a tabletop NANOS Scanning Electron Microscope (SEM) using Secondary Electron (SE) and Backscatter Electron (BSE) beam with a filament voltage of 15 KeV. The static flow behavior of the powder was measured using Hall flowmeter funnel, according to ASTM B213 standard [57]. The flowability behavior procedure consists of weighing 50.0 g of powder into a clean weighing dish, then closing the nozzle at the bottom of the funnel. After this, the weighted powder sample was carefully poured into the funnel of the flowmeter. At the same time, the stopwatch was started and the funnel's discharge hole was opened. The stopwatch was stopped as soon as the last powder came out of the orifice. The elapsed time was recorded with a precision of about 0.1 s. The test was repeated four more times and the average value was calculated.

The Apparent Density (AD) of the powder was measured using Hall flowmeter funnel according to ASTM B212 standard [82]. The test consists of weighing the empty density cup on the balance and setting the tare weight of the balance to zero. Then, the powder portion was carefully loaded into the funnel of the flow meter, allowing it to flow into the 25 cm^3 density cup through the discharge orifice. Once the powder has completely filled the cup and there is no more powder flowing through the funnel, using a spatula with the blade held perpendicular to the top edge of the cup, the powder is leveled at the same height as the top of the density cup. Any powder stuck to the external wall of the cup was wiped off and then the filled density cup was transferred to the balance and weighed with a precision of about 0.1 g. The process was repeated four more times. The apparent density AD_H is calculated using the following formula, where m is the measured mass from a filled cup that has a volume of 25 cm^3:

$$AD_H = \frac{m}{v} = \frac{m}{25cm^3}[=]\frac{g}{cm^3} \tag{4.1}$$

The cohesive index of the powder particles was measured using a Granudrum ® rotating drum system. The method is based on the use of a horizontal rotating cylinder having transparent walls also called the drum. This drum is half-filled with 100 g of the powder sample. This drum then rotates around its axis at an angular speed between 2 to 30 rpm. A camera takes pictures for each angular speed. In this work, 40 images of the drum were captured at an interval of 1 frame/s for each revolution per minute. For each rotation speed, the flow angle is calculated from the average position of the powder interface and the cohesive index is calculated from the fluctuations of this interface.

4.2 Methodology

As presented in Figure 4.1, the first steps of the additive manufacturing process are to create the 3D model of the printed part and to prepare the data and parameters that will be used during the printing process. SolidWorks software was used to model the 3D object and convert it into an STL file. The 3D model of an assemblage of rectangular prismatic-shaped coupons was chosen. It allowed printing all the samples to be further characterized and mechanical tested on one single build plate. Cutting and machining operations were subsequently performed to obtain the final samples. The 3D model was divided into 720 fixed-thickness digital layers of 50 μm. These files were then uploaded into a Matsuura

LUMEX Avance-25 printing machine system. These layers were aligned based on the center of the build plate.

An initial test with this specific powder batch was carried out in order to verify the spreading homogeneity of the powder by the recoater on the build plate. We also evaluated the heat dissipation based on the selected process parameters. It was found that as the recoater spread the powder over the build plate, some blank lines appeared in the powder layer area. Upon closely observing the movement of the recoater, it became apparent that a cluster of particles was hindering the spreading of powder, as schematically shown in figure 4.2.

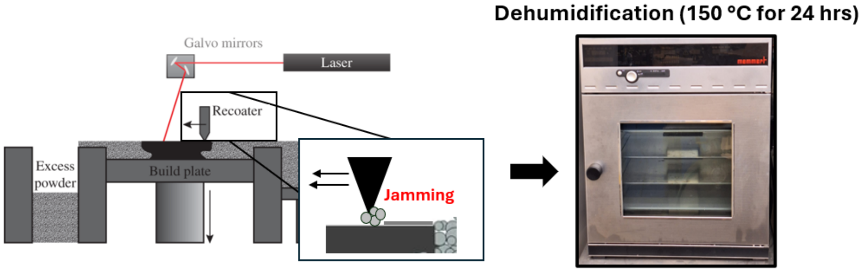

Figure 4.2 Schematic illustration showing the jamming behavior of the recoater when using raw powder, shown on the left. Memmert VO 400 Drying Oven used for the dehumidification process, shown on the right (modified from [25]).

Our initial hypothesis was that the powder may have absorbed moisture during handling before it arrived to the NRC facility. Also, it was determined that the powder batch had a significant fraction of both large and small particles. The combination of these two factors may have contributed to the formation of clusters during the powder spreading step. To overcome this issue, the 18Ni-300 MS powder was dehumidified in a Memmert VO 400 Drying Oven at a temperature of 150 °C for 24 hours. This procedure was performed before all subsequent printing runs to ensure that the powder was completely dry throughout the process, as well as to improve the flowability of the powder during the process, as will be discussed in section 5.

The Hybrid manufacturing of our samples was conducted in this Matsuura LUMEX Avance-25 system using the 18Ni-300 MS powder. This equipment allows the coupling of a L-PBF printing with a high-speed milling. A total of 20 rectangular prismatic-shaped coupons with dimensions of 75 mm (X) × 25 mm (Y) × 36 mm (Z) were printed on a 4140 steel build plate with dimensions of 175 mm (X) × 125 mm (Y) × 30 mm (Z). For this project, a total of 5 printing runs were performed with the 18Ni-300 MS powder batch. The schematic design of the coupons can be seen in Figure 4.3. Milling was performed after the

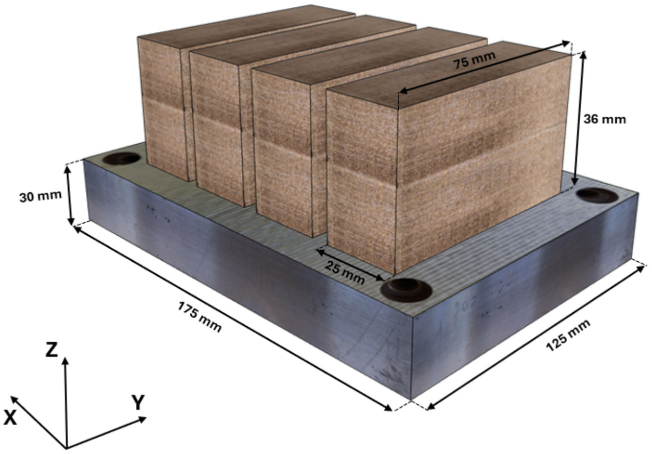

Figure 4.3 Schematic design of the coupons that were printed and machined using the Matsuura LUMEX Avance-25 system.

printing of each layer at a subtraction rate of 2000 mm/min for the horizontal top surface. This strategy ensured a correct leveling of each layer. It also allowed to remove traces of poorly fused powder and to reduce the temperature of the coupons being printed. The build plate was demagnetized using a surface demagnetizer to achieve a suitable magnetic field of <0.2 Gauss. The build plate temperature was set to 50 °C. The working chamber was filled with nitrogen gas to prevent oxidization of the molten pool during laser melting.

The process parameters used in each L-PBF print were based on previous work done by the NRC team. Sarafan et al. (2021) [43] investigated the effect of different process parameters on the physical and mechanical properties, roughness and microstructure of 18Ni-300 MS samples using a hybrid manufacturing Matsuura LUMEX Avance-25 system. Based on their findings, the best combination of process parameters was a laser power of 320 W with an ED of 76.2 J/mm^3. These parameters allowed to reach a relative density of over 99% with peak mechanical strength and elongation for as-built condition. Osman et al. (2023) [5] conducted further research, narrowing the process window by only varying the laser power level (240 W, 320 W, and 380 W) to obtain high-density parts and subsequently comparing the effects of STA and DA heat treatment cycles on the resulting microstructure and mechanical properties. They concluded that DA samples marginally reduced YS and UTS by about 7% compared to STA samples but increased ductility by up to about 34% through TRIP effects, which could be triggered by the austenite content of about 13.4% for the DA sample. This project aims to extend the analysis by setting the optimized process parameters found by Sarafan et al. (2021) [43] and Osman et al. (2023) [5] while focusing on the post-processing heat treatment steps. More specifically, a particular emphasis was put on the impact of the direct aging temperature on the resulting microstructure and mechanical properties. A bi-directional laser scanning strategy with 90° rotations after every layer was used for our L-PBF printing at a power of 320 W. This laser power was used for both the rastering/infill and contouring passes. Details of the L-PBF printing process parameters for the infill and contour applied to this project are shown in Table 4.2.

Table 4.2 Process parameters for L-PBF printing applied in the project.

Parameters	h (μm)	t (μm)	d (μm)	v (mm/s)	P (W)	ED (J/mm^3)
Infill	120	50	200	700	320	76.2
Contour	120	50	200	1400	320	38.1

4.2.1 Printing Stage

Before starting each printing run, the build plate was clamped inside the machine. The dimensions of the build plate were configured in the machine to ensure that the print build is centered and aligned (Figure 4.4 - Step 1). We also needed to ensure that the recoater would not touch the building plate during the powder spreading for each layer. An adjustment was made to the machining tool integrated into the printing machine to maximize the machine service life. We also needed to ensure that the machining tool would not touch in excess the sample build or the build plate during the printing process. Aluminum plates were placed around the build plate to reduce the amount of powder used during the spreading process by the recoater. The recoater and the print zone were thoroughly cleaned to avoid any external powder particles coming into contact with the print. Figure 4.4 shows the L-PBF printing execution steps that were conducted to guarantee a consistent high quality of the printed coupons.

After the machine cabin was closed, the chamber was filled with nitrogen until an oxygen level below 1% was measured. Once filled with inert gas, the printing process could begin. The printing process involved the spreading of the powder over the build plate area followed by the laser powder melting in the determined print area. This created print lines that alternate in direction by 90° (Step 2). After the laser melted the 50 micron layer covering the printing area in a bidirectional scan, the machining tool passed over the entire printed layer, ensuring a uniform surface without bumps and poorly fused particles. Then the recoater was passed again, spreading the powder over the build plate area and starting a new layer printing. This process was repeated 720 times (i.e. until the print was completed).

As the printing evolves, the amount of the 18Ni-300 MS powder in the container decreased. As a direct consequence, the printer needed to be stopped every 4/5 hours to

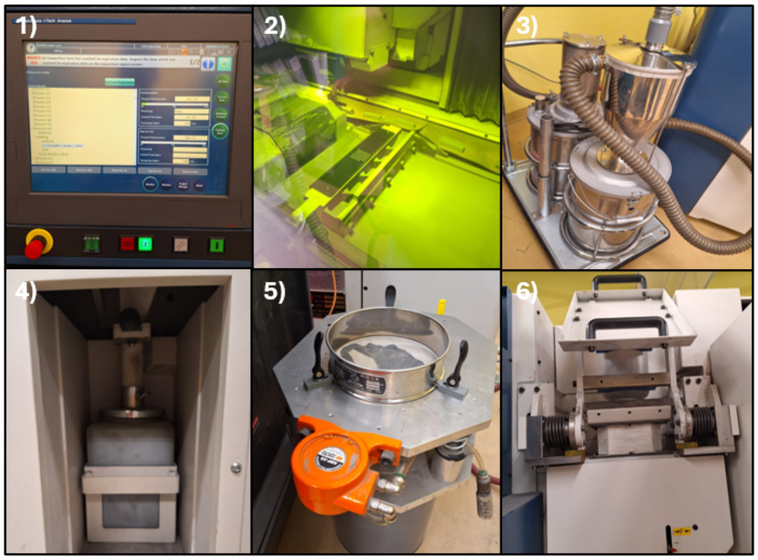

Figure 4.4 L-PBF printing execution steps. Configuration of L-PBF process parameters (Step 1). Execution of the printing process (Step 2). Cleaning of the machine (Step 3). Removing the powder from the baskets (Step 4). Powder sieving process (Step 5). Loading the machine with the sieved powder (Step 6).

refill and clean the machine (Step 3). The printing machine also has a system for collecting unused powder. The excess powder falls into baskets for subsequent reuse (Step 4). The powder in these baskets passes through a sieve with a 75 mesh to remove particles that may come from the milling. It also allows to deagglomerate the particles (Step 5). After this sieving process, the powder was poured into the container and loaded into the Lumex (Step 6). A safety apparatus was used to prevent particles from being breathed when handling the powder.

When the print was finished, the powder around the printed coupons were removed using a vacuum pump. The aluminum plates were removed and the build plate with the printed coupons was detached from the machine (Figure 4.5-a). The machine was cleaned for a new run. An Electro-discharge Machining (EDM) (FANUC Robocut C400iB) with a 0.2 mm diameter brass wire was used to separate the coupons from the build plate. The coupons were then cut into rectangular samples to be subsequently machined according to the geometries chosen for the mechanical tests and characterizations (Figure 4.5-b).

After machining (and before performing subsequent heat treatments and characterizations), 10x10x2 mm samples were cut from the coupons. A 100-grit abrasive grinding step was performed to polish and smooth the initially rough surfaces. These samples were used for Archimedes density measurements using A&D BM-500 density measurement kit. The

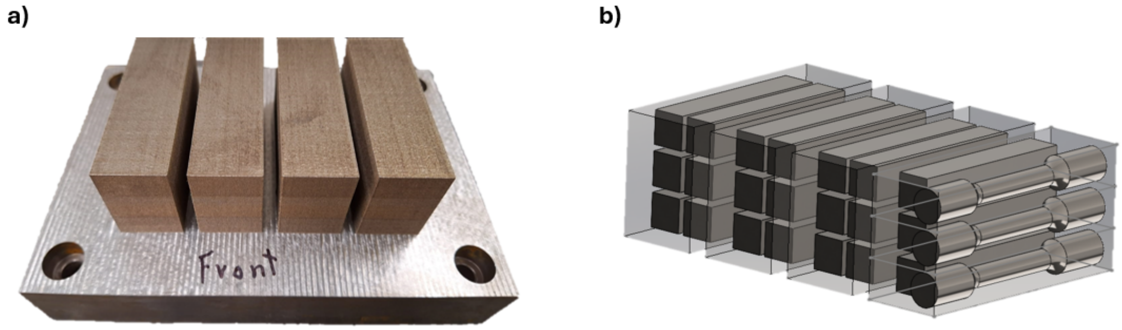

Figure 4.5 Coupons printed attached to the build plate (a) for each L-PBF printing run. Tensile and charpy planned specimens geometry for each coupon printed (b).

Archimedes method was based on the ASTM B311-17 standard [83]. The test consists of weighing the sample in air using an analytical balance and recording its weight as “mass A.” The sample is then removed and the balance is reset to zero. The sample is then carefully placed in a pan suspended in water on a beaker and weighed again as “mass B.” The water temperature is then recorded at the time of the Mass B measurement using a thermometer. Care was taken to ensure that the suspension support and the sample were free of air bubbles. The test was repeated 5 times for each sample. The density measurements are discussed in Section 5. The Archimedes density calculation is performed using the following equation:

$$D = \frac{Mass\ A \times Density_{(air-free\ water)}}{Mass\ A - Mass\ B} [=] \frac{g}{cm^3} \tag{4.2}$$

4.2.2 Samples Geometry

Tensile and impact specimens as well as samples for hardness, X-Ray Diffraction (XRD) and microstructural analysis were extracted from the four L-PBF coupons. One of the four main coupons was machined to obtain 3 specimens for tensile tests and 3 specimens for Charpy impact tests. The other 3 coupons were machined to obtain 18 specimens for Charpy Impact tests as well as 3 small samples for hardness, microstructural analysis and phases quantification. The layout of the samples and specimens that were machined from the coupons can be seen in Figure 4.6.

In total, 5 build plates having 4 coupons each were printed by L-PBF in the course of this project. Each build plate was associated with a specific direct aging heat treatment temperature. **This overall printing and machining strategy gave a total of 15 tensile specimens, 105 Charpy impact specimens and 15 samples for the remaining characterization analyses.**

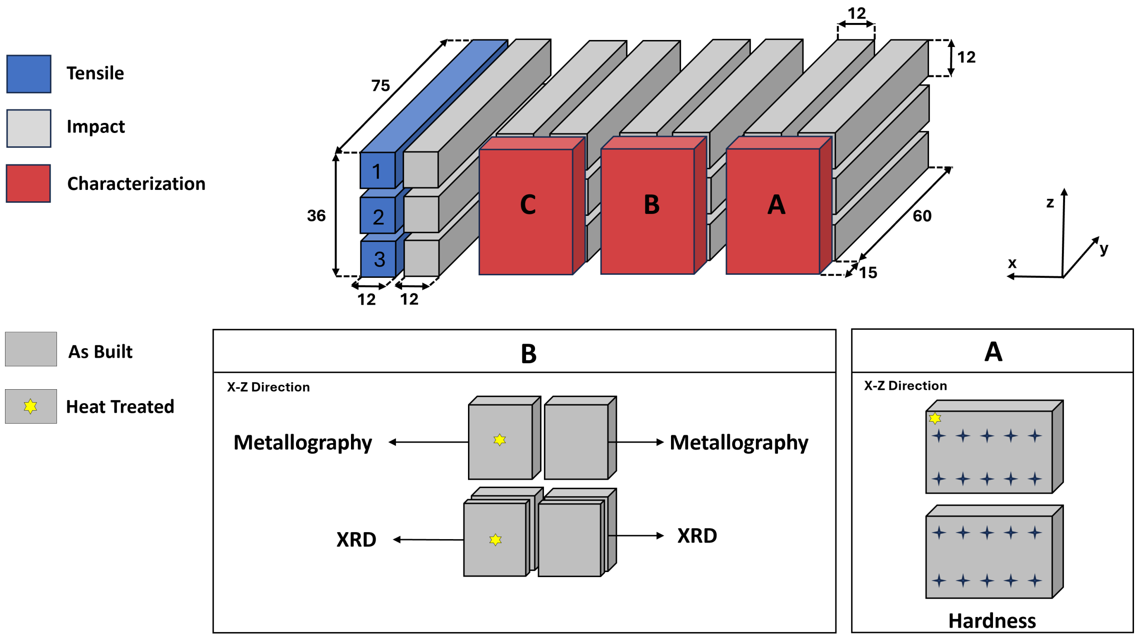

Figure 4.6 Coupon cutting geometry of each L-PBF printing run for subsequent machining of samples for mechanical testing and microstructural characterization.

4.2.3 Heat Treatment

As discussed in Section 2.3.2, the existing literature focuses on the temperature and duration of heat treatment (whether studying STA or DA heat treatments) to achieve peak mechanical strength. This temperature was identified to be around 480 to 500 °C [4,38]. The present study focuses on direct aging temperatures that maintain good mechanical strength while seeking an increase of the elongation and toughness properties of the material. These targeted properties are essential for high impact energy absorption applications. The proposed heat treatment process and metallurgical state of our specimens were as followed:

- As built.
- Direct Aging (DA) treatment at 490 °C for 6 hours, followed by air-cooling to room temperature.
- Direct Aging (DA) treatment at 510 °C for 6 hours, followed by air-cooling to room temperature.
- Direct Aging (DA) treatment at 530 °C for 6 hours, followed by air-cooling to room temperature.

- Direct Aging (DA) treatment at 560 °C for 6 hours, followed by air-cooling to room temperature.

The machined samples (used for characterization and mechanical testing) were packed in ultra-thin stainless-steel heat-treating foil envelopes before each heat treatment performed in a Vulcan 3-550 Three-Stage Burnout Furnace. Inside these envelopes, the samples are placed with an Omega's Wireless RTD Thermocouple type K to continuously measure the temperature throughout the heat treatment process. White paper strips were also placed in these envelopes to consume excess oxygen and prevent excessive oxidation of the samples. The envelopes were then tightly sealed to prevent air from entering and placed in the furnace. The heat treatments were then conducted according to the selected DA condition for 6 hours and then air-cooled to room temperature, as shown in Figure 4.7.

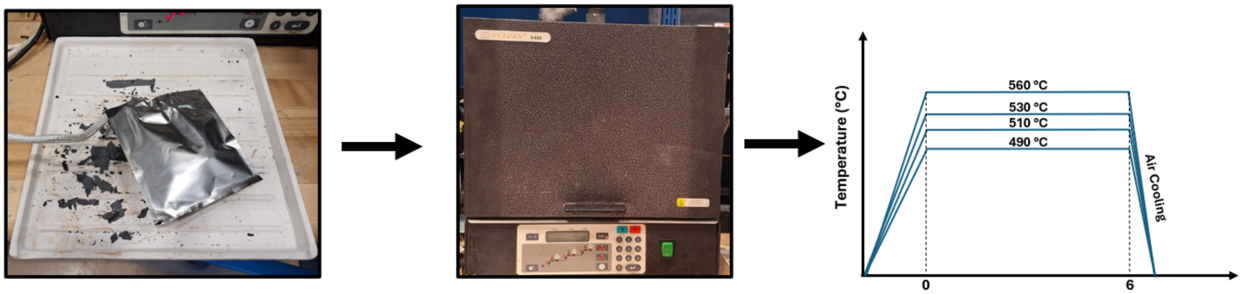

Figure 4.7 Procedure for performing direct aging heat treatment under different conditions on samples for characterization and mechanical testing.

4.2.4 Microstructural Characterization

Samples were prepared from section B for microstrutural characterization as shown in Figure 4.6 (for both the as-built and heat-treated conditions). They were prepared for microscopic inspection by hot mounting in Bakelite containing carbon filler (Struers PolyFast) for easier SEM examination. A polishing protocol was performed with successively finer grain Silicon Carbide (SiC) papers of #180, #320, #500 and #1200 grit for 5 min each. A single-stage fine grinding process was conducted using an MD-Largo disk and 9 μm diamond suspension for 3 min with an alcohol-based lubricant. Subsequently, the samples were polished using 3 μm diamond suspension and lubricant with an MD-Dac cloth for 3 min and a final polishing using 1 μm diamond suspension and lubricant with an MD-Nap cloth for 5 min. The complete metallography procedure was performed using a semi-automatic Struers Tegramin grinding and polishing machine.

Some samples were chemically etched by immersion in a 2% vol. Nital solution (Nitric Acid in Ethanol) for 1 min to observe specific features of their microstructure. A VHX-7000 Digital Microscope and a JEOL JSM-7600TFE SEM coupled with a field emission gun (FEG) were used for the microstructural characterization. The amount of austenite content in the sample was quantified using an XRD technique. The samples were chemically polished according to ASTM E975 [84]. The samples were cut into 10 x 10 mm sizes with 1 to 2 mm thickness. Their surface was mechanically polished to SiC #1200 paper. The samples were immersed in a solution of 30% HCl (Hydrochloric Acid) + 30%HNO_3 (Nitric Acid) + 40% H_2O (Water) in volume for 10 minutes while being magnetically stirred. The samples were washed and rinsed with water. This aqueous surface dissolution treatment was intended to remove the surface residual stresses that can alter the crystallographic orientation of the austenitic phase caused by the polishing process. The diffraction data for the as-built and heat-treated samples were obtained with a Miniflex Benchtop Rigaku X-ray diffractometer with a Cu-anode, operating at a voltage of 15 kV in X-Ray Fluorescence (XRF) reduction mode. Diffraction patterns were acquired in the angle range (2θ) from 3° to 120° at scanning step of 0.01° and speed of 0.1°/min. The XRD results were analyzed according to the Rietvield method [85] using the Crystallography Open Database for austenite (COD ID #7204807) and martensite (COD ID #1100108) to quantify the phases.

4.2.5 Room-Temperature Tensile Testing

In accordance with the principles guided by the ASTM E8/E8M standard [86], the tensile specimens were machined in a subsize round dog-bone shape with a gauge length of 24.0 mm and a diameter of 6.0 mm. Three tensile specimens were machined along the Build Direction (BD) from the manufactured prismatic coupons (75x36x12 mm^3) for the as-built and for each DA temperature (i.e. 490 °C, 510 °C, 530 °C and 560 °C). The geometry of the tensile specimen can be found in Figure 4.8. Tensile tests were performed for 15 tensile specimens (i.e. 3 samples for each heat treatment condition) at room temperature using a 250-kN MTS testing frame equipped with a laser extensometer. In addition, a non-contact optical 3D deformation measurement system, commonly referred to as Digital Image Correlation (DIC) Aramis® was used to measure elastic and plastic deformation during the tensile tests. For the laser extensometer measurements, one side of the specimen diameter was marked with two pieces of retro-reflective tape at each end of the service area in order to define the gauge length for measurement during the uniaxial tensile loading. For the DIC system measurements, the opposite surface of the specimen was sprayed with white paint to produce a uniform bright background. A black speckled paint with a high-contrast random pattern was then applied. This measurement technique is based on a pixel-speckle correlation

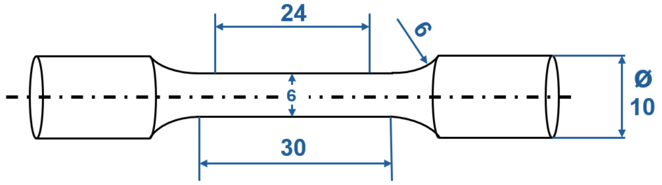

	Specimen Dimension (mm)
Gauge Length	24.0
Diameter	6.0
Radius of fillet, min	6.0
Length of reduced section, min	30.0

Figure 4.8 Subsize round dog-bone shape tensile specimens based on the E8/E8M standard [86].

obtained during the tensile test. The DIC system's accuracy is affected by the quality of the speckle pattern, thus the pattern recognition algorithm precision was verified before the final tests to ensure an accurate strain recording in the gauge length zone.

During the tensile tests, the constant speed of the uniaxial load exerted by the crosshead was set to 0.4 mm/min, ensuring a quasi-static loading at a strain rate of $10^{-4}s^{-1}$. Tensile properties such as the 0.2% YS, UTS, El and the Young Modulus (E) were evaluated for each heat treated condition using the results of three replicates. After all the tests were completed, the load data were collected from the tensile test system to calculate the engineering stress. Firstly, the data from the laser extensometer were used to calculate the strain. Unfortunately, some inconsistencies were found in the strain values which did not match the data collected from the DIC. One of the hypotheses behind the inconsistencies was that slippage happened during the tensile load induced by an inadequate gripping of the round specimens. This resulted in inaccurate strain measurements in the elastic region when using laser extensometer data. For these reasons, the DIC system was used to collect the strain data. In addition, the DIC system generated valuable deformation distribution maps based on the Force-Strain correlations. This allowed us to evaluate the localized strain and the location of the crack initiation site for each sample during tensile loading.

4.2.6 Impact Charpy Tests

Impact Charpy tests were performed at 6 different temperatures (i.e. -100 °C, -50 °C, 0 °C, 25 °C, 100 °C and 200 °C) in order to develop a DBTT curve for our maraging steel. One triplicate sample was preserved in the eventuality that a measurement needed to be discarded. Therefore, a total of 105 Charpy impact specimens were machined in accordance with the E23 standard [76]. According to this standard, Charpy specimens must have a length of 55 mm as well as a height and a width of 10 mm (see Figure 4.9). The impact toughness tests were carried out using a Tinius Olsen Impact testing machine. Liquid nitrogen and ice were used for low-temperature testing while a furnace adjacent to the impact testing machine was installed for high-temperature testing. Samples were soaked for at least 5 minutes at the desired temperature to ensure temperature homogeneity. Each sample was then rapidly transferred to the machine and broken in accordance with the ISO 148-1 standard [75]. The fracture surfaces of the specimens obtained after the impact Charpy and the tensile tests were observed using Optical Microscope (OM) and SEM (using SE and BSE mode with a filament voltage of 15 KeV). These microstructural observations were used to examine the failure characteristics of the 18Ni-300 MS in the presence of different defects (such as pores and inclusions).

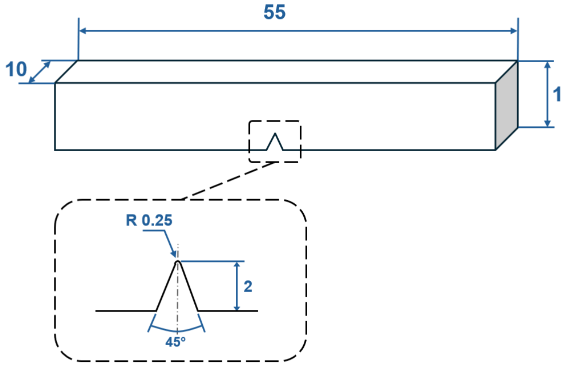

	Specimen Dimension (mm)
Length of Charpy Specimen	55.0
Width	10.0
Thickness	10.0
Radius of notch, Type V	0.25

Figure 4.9 Geometry of the impact Charpy specimen based on the E23 standard [76].

4.2.7 Hardness

As shown in Figure 4.6, section A of the first coupon was used for hardness measurements (for both the as-built and heat-treated conditions). A Vickers microindentation technique was used to measure the hardness of each specimen according to the ASTM E384 standard [87]. The samples were mounted in Bakelite with a polished surface (mirror-finished) and placed in the Struers DuraScan 80 hardness tester (Ballerup, Denmark). The hardness distribution was evaluated in the X-Z direction using a total of 28 indentations distributed over the surface area of the sample with a force of 500g. An indentation spacing of 2 mm (see Figure 4.10) and a dwell period of 12 seconds were used. A 60x objective lens was used to analyze the indentations.

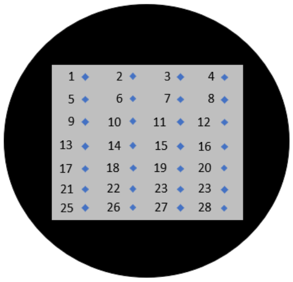

Figure 4.10 Vickers microhardness distribution across the surface area of the sample (X-Z Direction).

CHAPTER 5 RESULTS AND DISCUSSION

5.1 Physical Properties of the 18Ni-300 Maraging steel

Before starting the additive manufacturing process using 18Ni-300 maraging steel (18Ni-300 MS), it was necessary to verify that the physical properties of the dehumidified powder were suitable for printing. Table 5.1 provides the Apparent Density (AD) and flowability behavior of the powder used for printing. The density measurements were repeated five times with different randomly selected powder samples from the container to ensure acceptable reproducibility.

Table 5.1 Apparent density and Flowability (50 g) characteristics of 18Ni-300 maraging steel from batch Nº 24D0446 used for L-PBF printing. The standard deviation and average were calculated and are presented.

Powder Sample (18Ni-300 Maraging Steel)	Apparent density (g.cm^{-3})	Flowability (s)
1	4.06	18.90
2	4.06	18.56
3	4.04	18.99
4	4.04	19.09
5	4.04	18.98
Mean	4.05 ± 0.01	18.90 ± 0.2

The apparent density values presented in this table confirm the homogeneity of the powder (low data dispersion). The particle packing showed consistent AD. The wide size particle distribution that can reach up to about 53 μm (according to the PSD results presented in Chapter 4) is believed to be at the origin of this behavior. Sarafan et al. (2021) [43] performed the same tests and obtained 4.28 g/cm^3 of apparent density, 52 μm of D90 from PSD measurement and 23 s of flowability using the Hall funnel with 18Ni-300 MS powder from the same supplier. Comparing the results obtained from both studies, it can be seen that the flowability tests obtained in the present work were better, which may positively contribute to the powder flowing properties during the L-PBF process. An optimal particle size distribution along with spherical particles increase AD property. This results in an improved solidification during the L-PBF process as concluded by Tan et al. (2017) [88]. For similar particle size distributions, higher apparent densities were obtained in the work of Sarafan et al. (2021) [43] when compared to our study. Less uniform particle morphologies may have contributed to the lower AD in the present study as it will be discussed next.

The powder morphology and size distribution were observed via an SEM using secondary electron imaging with a voltage of 15 KeV. A typical SEM-SE image for the powder used in this work is presented in Figure 5.1. Maraging steel particles are characterized by a predominantly spherical morphology as a result of the nitrogen gas atomization process used to produce this powder. Larger particles (diameter around 60 to 70 μm) can also be observed. These large particles exhibit a more elongated and irregular shape. Some particles also exhibit satellite features. Although the gas atomization process tends to produce spherical particles, collisions between particles during the solidification process of molten/semi-molten particles can form irregularly shaped particles. Irregular particles increase surface friction. This leads to a tendency for mechanical particle interlocking upon flowing, resulting in a low packing density. The presence of these irregular and satellites particles may be indicative of the low apparent density of the powder batch used in this work. Moreover, these irregular-shape particles may have contributed to the obstruction of the recoater and the heterogeneous powder spreading during the preliminary tests without dehumidification steps.

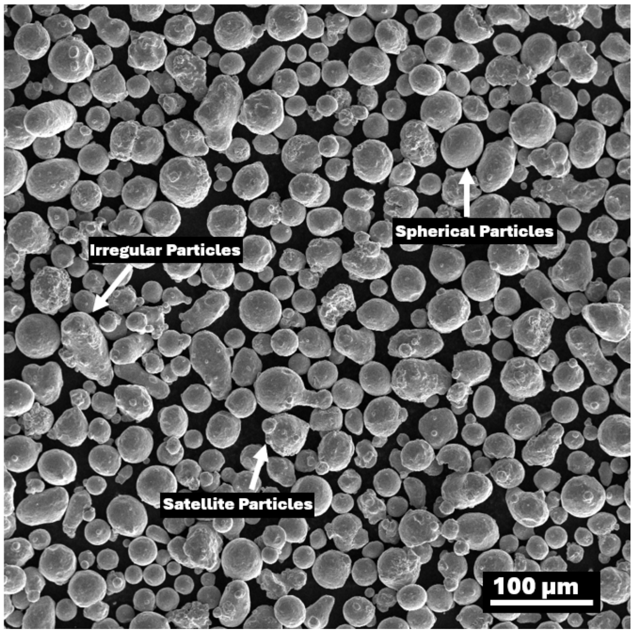

Figure 5.1 SEM-SE image showing the morphology of the 18Ni-300 MS powder.

The cohesion index of the powder particles was measured using the GranuDrum rotating drum system (as discussed in Chapter 4). The average location of the interface between the atmosphere and the powder bed at each angular velocity was determined by the integrated GranuDrum software. It also evaluated the cohesion index of the powder. A powder with a cohesion index below 24 exhibit free-flowing behavior. This results in better dispersion of the powder and the formation of a uniform and homogeneous deposited layer [43].

As the cohesion index is lowered, there is an improvement in the flowability properties of the powder which affect the layer formation process. Figure 5.2 shows the particle cohesion index for the 18Ni-300 MS powder before and after the dehumidification process at 150 °C for 24 hours. The figure also reports the cohesive indexes measured in the work by Sarafan et al. (2021) [43].

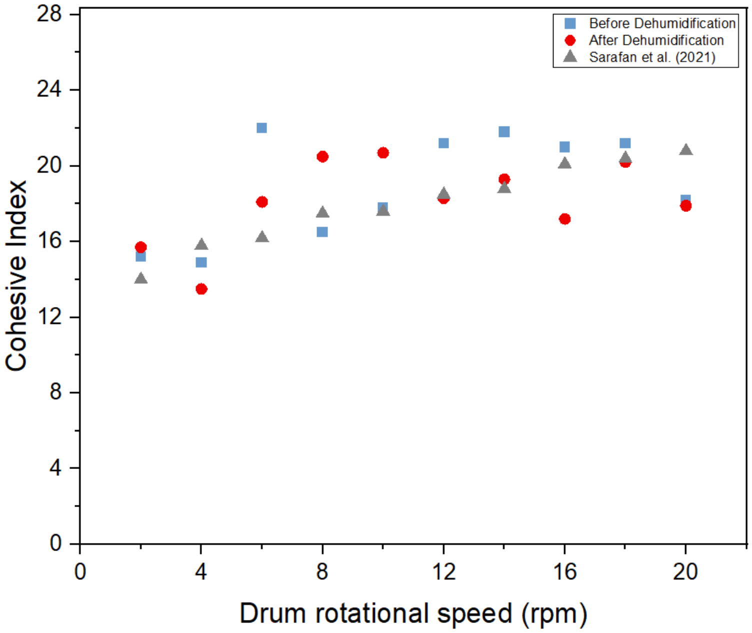

Figure 5.2 Cohesive index of 18Ni-300 MS powder versus the drum rotation speed for samples before and after dehumidification process and its comparison with the literature [43].

Prior to the dehumidification process, the cohesion index was below 24. It remained close to or above 20 for most rotation speeds. After dehumidification, there was a decrease in the cohesion index values and an improvement in the flowability of the material. This degradation in the flowability of the as-received powder may be related to moisture retained in the powder during the delivery handling process. Indeed, when compared to the batch of Sarafan et al. (2021) [43], the dispersion results in the present work is relatively high, reaching values above 20 for speeds of 8 and 10 rpm. This could be explained by the reduced flowability of the powder due to the mechanical interlocking of satellite particles and large irregular particles still present in the dehumidified powder. The dehumidified powder was used in all L-PBF printing runs. Homogeneous powder layers were created by the recoater with this dehumidified powder. Each 50 micron layer was dispersed homogeneously atop the build plate/previous layers, without the visually presence of empty lines or discontinuities. This validated the dehumidification process we applied prior to each print.

The Archimedes density of the as-printed coupons was measured according to ASTM

B311-17 standard [83] before performing the direct aging heat treatments. As discussed in Chapter 4, the samples from each print were tested five times. The theoretical density value of 8.1 g/cm^3 was used in equation 4.2 [2]. Table 5.2 shows the measured relative densities based on weighing the mass of the sample in air (Mass A) and by weighing the mass with the sample placed in a pan suspended in water in a beaker (Mass B) and air-free water density.

Table 5.2 Average Archimedes density and its standard deviation for 18Ni-300 maraging steel samples from each L-PBF printing run. Mass A represents the mass of the sample weighed in ambient air, and Mass B represents the mass of the sample placed in a pan suspended in water in a beaker.

Sample	**Mass A**	**Mass B**	**Temperature (°C)**	**Density$_{Air/Free\ Water}$**	**Density (g/cm^3)**	**Relative Density (%)**
1° Run	9.9868 ± 0.0003	8.7419 ± 0.0004	22	0.9978	8.0046 ± 0.0037	**98.8227 ± 0.0460**
2° Run	10.3506 ± 0.0003	9.0610 ± 0.0008	22	0.9978	8.0086 ± 0.0047	**98.8714 ± 0.0576**
3° Run	10.1109 ± 0.0001	8.8506 ± 0.0007	21.5	0.9979	8.0058 ± 0.0043	**98.8368 ± 0.0535**
4° Run	10.3882 ± 0.0025	9.0948 ± 0.0004	21.5	0.9979	8.0145 ± 0.0131	**98.9444 ± 0.1618**
5° Run	10.8744 ± 0.0002	9.5197 ± 0.0004	21.5	0.9979	8.0099 ± 0.0019	**98.8872 ± 0.0234**
Average						**98.8725 ± 0.0478**

The relative densities obtained for the as-printed samples were fairly high, reaching maximum values of 98.94% for the fourth run. Comparing the standard deviation datasets for all runs, the densities measured by Archimedes can be considered statistically equivalent. This demonstrates the consistency of the L-PBF printing technique using the same process parameters. As a comparison, the density of the L-PBF printed sample obtained in the work of Sarafan et al. (2021) [43] for a laser power of 320 W reached 8.07 g/cm^3, with a relative density of 99.6% using the same process parameters and equipment. Mutua et al. (2017) [41] analyzed several process parameters for the same Matsuura LUMEX Avance-25 machine. The parameters considered optimal in their study are compatible with those used in the present project. They achieved a maximum relative density of 99.8% for a laser power of 300 W. Beyond 300 W, the relative density decreased to 99.2% for a maximum laser power of 400 W [41]. Since the L-PBF process parameters for obtaining maximum relative densities are similar to the ones reported in the literature, the physical characteristics of the powder may have significantly influenced the final relative density of the printed coupons. The presence of a wider range of particle size distribution, as well as the presence of irregular and satellite particles, could contribute to the formation of isolated pores during the densification of the material.

5.2 Hardness Vickers

Samples from section A (Figure 4.6) of one coupon from each printed run were used for hardness Vickers measurement. Figure 5.3 shows the average hardness Vickers calculated from the 28 indentations performed for the As-Built (AB) case and for each DA heat treatment condition, referred here as Direct Aging at 490 °C (DA490), Direct Aging at 510 °C (DA510), Direct Aging at 530 °C (DA530), Direct Aging at 560 °C (DA560).

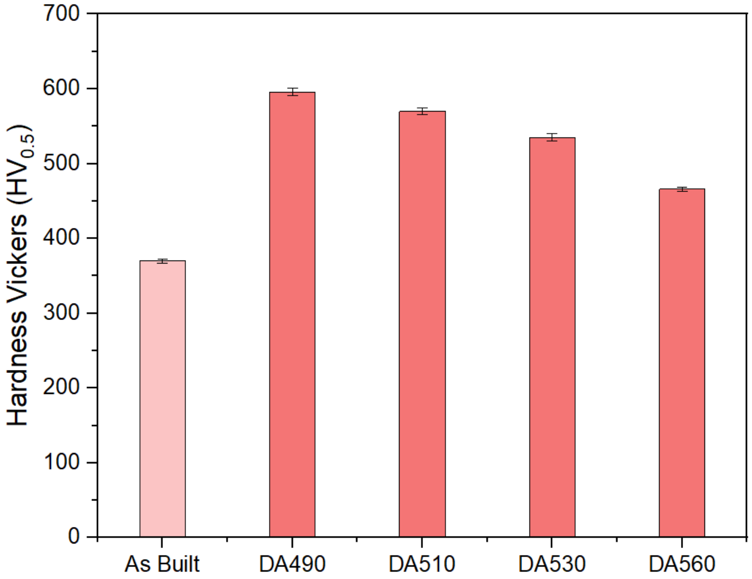

Figure 5.3 Average hardness Vickers for the As-Built (AB) condition and for the different direct aging treatments studied (490 °C, 510 °C, 530 °C and 560 °C for 6 hours).

Sample AB showed the minimum average value of 370 ± 3 HV. This low hardness results from a fine soft martensitic microstructure with cellular and dendritic mesostructures, achieved through rapid cooling in the L-PBF process. After direct aging treatment, hardness values significantly increase due to the precipitation of intermetallic nanoparticles in the martensitic matrix [38]. DA490 results in peak hardness, reaching a value of 596 ± 5 HV, where high strengthening effect takes place. As the direct aging temperature increases (DA510, DA530 and DA560), the hardness value decreases to 570 ± 4 HV, 535 ± 5 HV, and 466 ± 3 HV, respectively. At high aging temperatures, austenite reversion is likely to occur, which, combined with retained austenite remaining from the solidification process and coarsening/dispersion of nanoprecipitates in the matrix, can lead to a decrease in the hardness of the material [38]. The microstructural impact on the mechanical properties of 18Ni-300 MS will be discussed in Section 5.4. It is to be noted that the data were reported as the average of the 28 indentations since there were no major variations in hardness across the area represented by the indentations as shown in the Figure 4.10. The optimal L-PBF process parameters contributed to a higher densification and, consequently, to a consistent hardness across the entire test area.

Figure 5.4 reports the average hardness results obtained in this work compared with hardness Vickers data from the literature for different direct aging treatment temperatures applied for 6 hours [5, 38, 67, 89]. The data for AB sample obtained in this work agrees with those reported in the literature, supporting the fact that the L-PBF process was successful in achieving a maximal densification of the material.

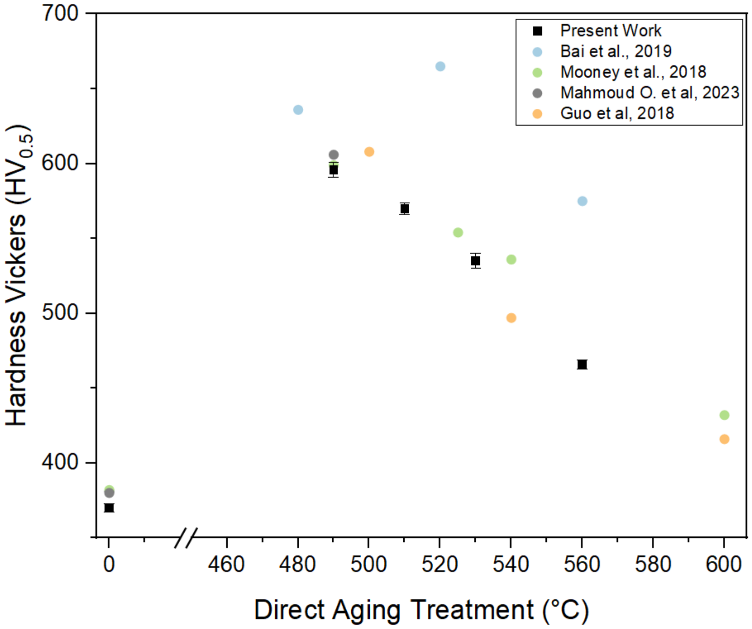

Figure 5.4 Comparison of present work with hardness Vickers (500 gram load) data collected from the literature as function of direct aging temperature for 6 hours [5, 38, 67, 89].

Direct aging at 480 to 500 °C is the most commonly reported heat treatment in the literature since peak hardness and strength are obtained under these conditions (Figure 2.13). The hardness of the DA490 sample was similar to those published in the literature for hardness Vickers measured with a 500g load. Increasing the DA temperature causes the hardness values to follow the same declining trend reported by most authors. This is an indication that the heat treatments were performed correctly in the present work. It is to be noted that only the work of Bai et al. (2019) [67] shows a hardness peak at a higher temperature of 525 °C. This high hardness also had an impact on the tensile mechanical properties as will be discussed in Section 5.5. Nevertheless, it can be considered an isolated case.

5.3 Phase Proportion Quantification

The as-built and heat treated samples were chemically polished and placed in the Rigaku Miniflex diffractometer as discussed in Section 4.2.4. Figure 5.5 shows the XRD patterns for the AB and heat treated conditions between 35 and 120° diffraction angles. The figure highlights the main peaks associated with the presence of martensite and austenite. The quantification of the austenite phase content based on XRD patterns and calculated from Rietveld refinement method are presented in Figure 5.6.

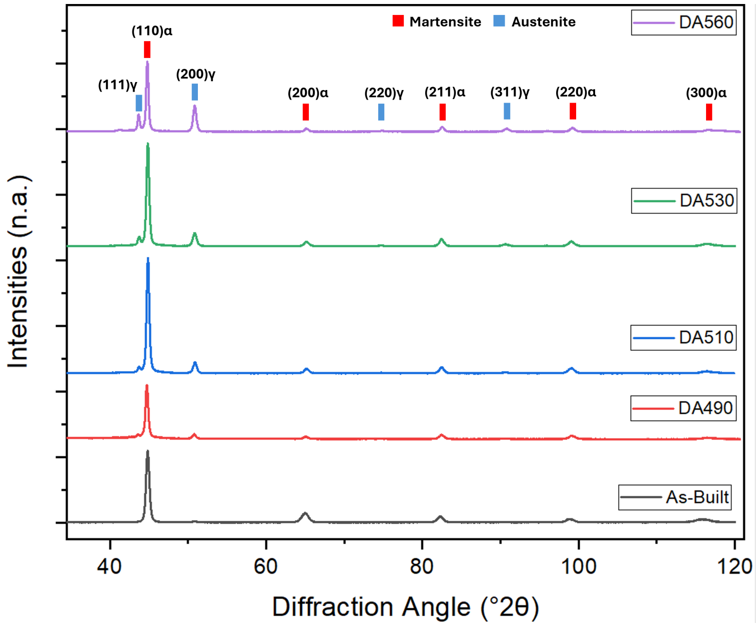

Figure 5.5 XRD patterns between 35 and 120° for 18Ni-300 maraging steel in AB and directly aged conditions at 490 °C, 510 °C, 530 °C, and 560 °C for 6 hours. Red stripes are martensite diffraction pattern and blue stripes are austenite diffraction pattern.

According to this figure, the as-built sample exhibits an almost fully martensitic microstructure. The major $\gamma(111)$ and $\gamma(200)$ diffraction peaks of austenite are barely visible in the XRD pattern. Likewise, the quantification of austenite content for the as-built sample was around 1.66% vol. There was almost no retained austenite in the microstructure after rapid solidification of the melt pool, inherent to the MAM process. The austenite diffraction peaks intensified after DA treatment, especially the $\gamma(111)$ and $\gamma(200)$, compared to the AB condition. The austenite content rises as the DA temperature increases due to the reversion of austenite in the microstructure. Austenite volume fraction reached 18% vol. and 30% vol. for the 530 °C and 560 °C conditions respectively (see figure 5.3). There is also a slight difference in austenite content between 490 °C and 510 °C, (i.e. 11 and 13% in volume respectively). These findings are consistent with those reported in the literature [4, 67, 68]. Many authors observed a gradual increase in the austenite fraction while increasing DA temperature. Interestingly, the literature includes the work of Osman et al. (2023) [5] which used the same Matsuura Lumex printing machine.

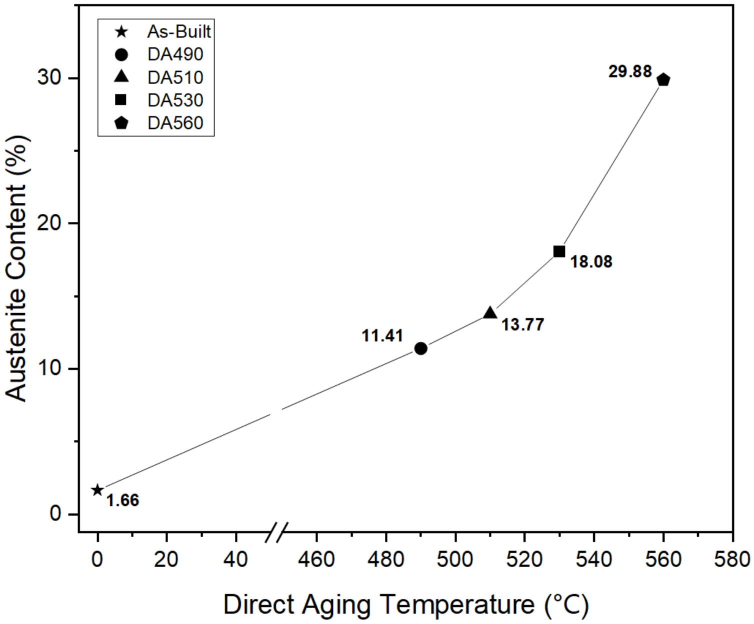

Figure 5.6 Quantification of austenite content calculated from Rietveld refinement for AB and directly aged conditions at 490 °C, 510 °C, 530 °C, and 560 °C for 6 hours.

Thermodynamic simulations can be used to predict the fraction of ferrite, austenite and intermetallics which should form in a fully equilibrated system. Assuming that martensite fraction correlates with the ferrite fraction (which is a crude assumption considering that martensite is a metastable phase of higher Gibbs energy when compared to ferrite), these thermodynamic calculations may give some indications about the thermodynamic driving force for the formation of austenite and precipitates as a result of direct aging. Thermodynamic equilibrium calculations performed with the FactSage 8.4 in the 450 °C to 600 °C temperature range for the chemical composition of the 18Ni-300 MS alloy studied in the present project are presented in Figure 5.7. These equilibium calculations indicate that the austenite content increases as the temperature rises. From a kinetic perspective, this phase transformation is driven by the martensite-austenite reversion which is promoted by the diffusion of austenite/gammagene elements such as Ni [64]. According to this figure, only the Ni_3Ti intermetallics form at equilibrium in this temperature range. At equilibrium, this alloy should contain approximately 3% vol. at aging temperature between 490 to 500 °C. As the austenite content increases, the Ni_3Ti content decreases as its dissolution in the matrix occurs.

DA treatment are completed by cooling the sample in air by convection which is not an infinitely slow cooling rate. It is not expected that the cooled samples would reach an equilibrium state. Therefore, only martensite, austenite, and perhaps Ni_3Ti are expected to

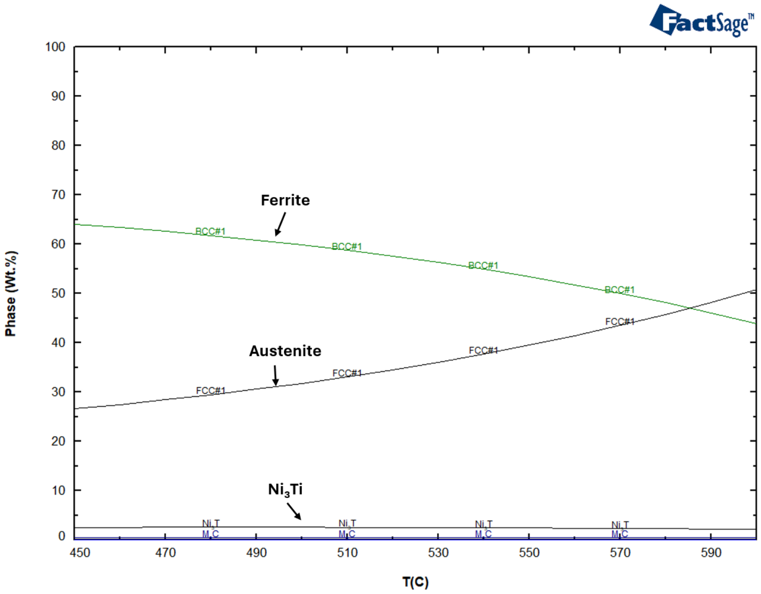

Figure 5.7 Equilibrium phase diagram simulation calculated by FactSage 8.4 in the temperature range of 450 and 600 °C for the chemical composition of the 18Ni-300 maraging steel.

form in the metastable equilibrium. The austenite fraction evaluated from the XRD measurements is lower than predicted by thermodynamic calculations. Moreover, the intermetallic fraction was so small in our heat treated samples that we could not detect them by XRD. Additional characterization techniques such as the Transmission Electron Microscopy (TEM) to identify their presence should be considered in the future.

According to our analysis, the microstructural design for austenite reversion can be more effective through direct over-aging treatments, since the cellular structure and retained austenite are removed when performing ST treatment. Therefore, fine-tuning DA temperature can bring benefits to improve toughness through austenite stability and its influence on the microstructure during deformation, as will be discussed in the following sections.

5.4 Microstrutural Characterization

The main microstructural features of the as-built and directly aged L-PBF printed 18Ni-300 MS samples can be examined in Figure 5.8. For the AB sample (Figure 5.8(a)), the melt pool boundaries caused by the change in scanning orientation are clearly visible. The scanning strategy pattern by rotating overlapping melt tracks by 90° are also distinguished. The calculated bead height from these images was between 70-100 μm, with a bead width of 120-140 μm. These measurements are directly related to the defined printing process parameters (such as layer thickness and hatch space). The printing parameters were adjusted to homogenize heat distribution while adjusting the dimensions of the melt pool.

The melt pool boundaries were preserved with minor changes to the lath martensitic microstructure in DA at temperatures of 490 °C (Figure 5.8(b)) and 510 °C (Figure 5.8(c)). As the temperature rises to 530 °C (Figure 5.8(d)) and above, decomposition of the melt pool boundaries and the scanning lines inherent to the printing process can be observed. As described in the previous sections, a reversion of the martensitic structure to austenite occurs, which cannot be observed under optical microscopes. Nevertheless, an almost homogeneous microstructure for DA at 560 °C (Figure 5.8(e)) is obtained, in which the long strips and cellular structures of the martensite packet become blurred. Cell walls appear thicker and discontinuous, as will be corroborated in the SEM images at higher magnification.

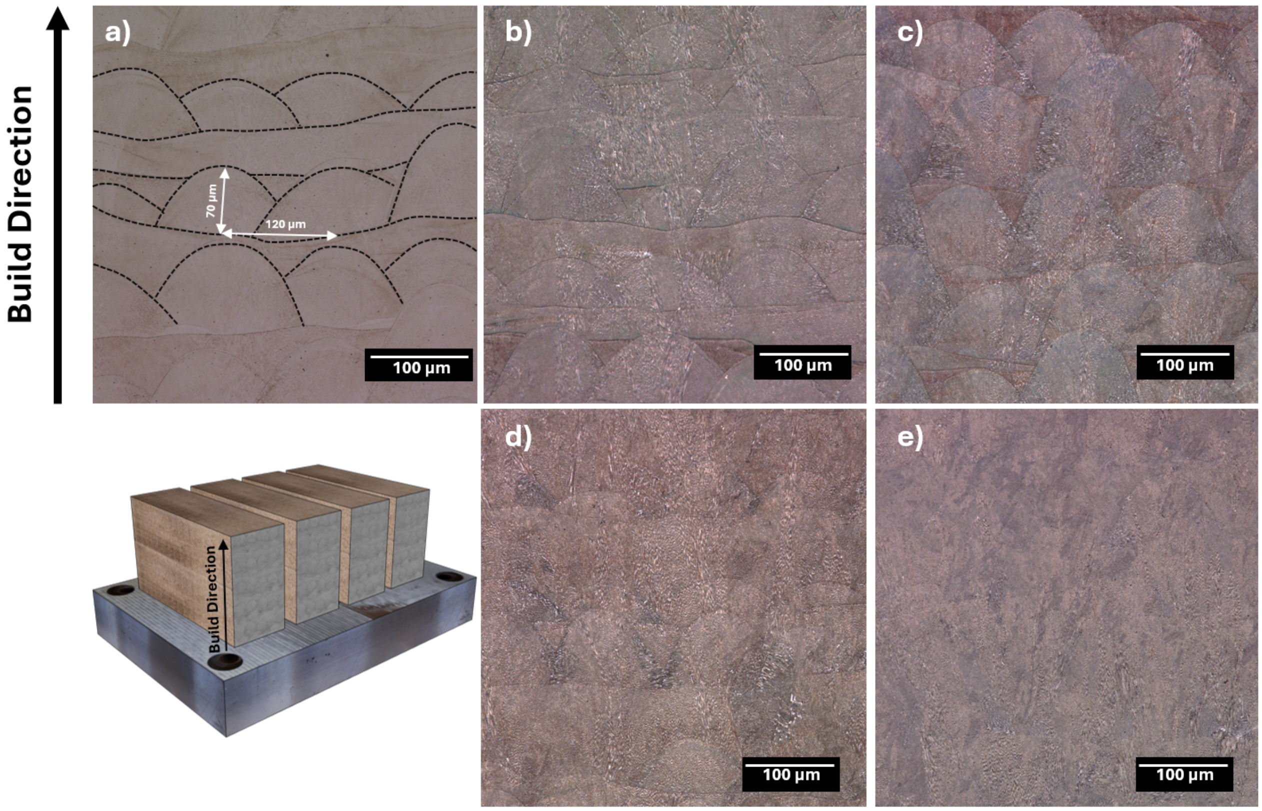

Figure 5.8 Optical microscopy (OM) images of 18Ni-300 maraging steel (x500): (a) As-Built condition; (b) DA at 490 °C for 6 hours; (c) DA at 510 °C for 6 hours; (d) DA at 530 °C for 6 hours; (3) DA at 560 °C for 6 hours.

Figure 5.9 shows the microstructure of a 18Ni-300 MS sample printed by L-PBF at high magnification using backscatter electrons (BSE) mode. This SEM operating mode allowed to increase the contrast between heavier and lighter elements. Figure 5.9(a) shows the as-built condition with a predominantly martensitic microstructure with fine cellular and columnar structures. Epitaxial growth can be observed, which is characteristic of grain nucleation and growth according to the heat flow generated in the melt pools. Also, the high thermal gradient and rapid solidification inherent to the L-PBF process (in the order of 10^6-10^8 °C/s) promoted the solidification of supersaturated phases enriched in alloying elements. A fine martensitic structure and residual retained austenite is formed as previously validated by [5, 90]. Direct aging treatment caused a transformation of the fine martensitic structure into coarser lath martensite, as well as a change in the distribution of alloying elements in the phases present in the maraging steel.

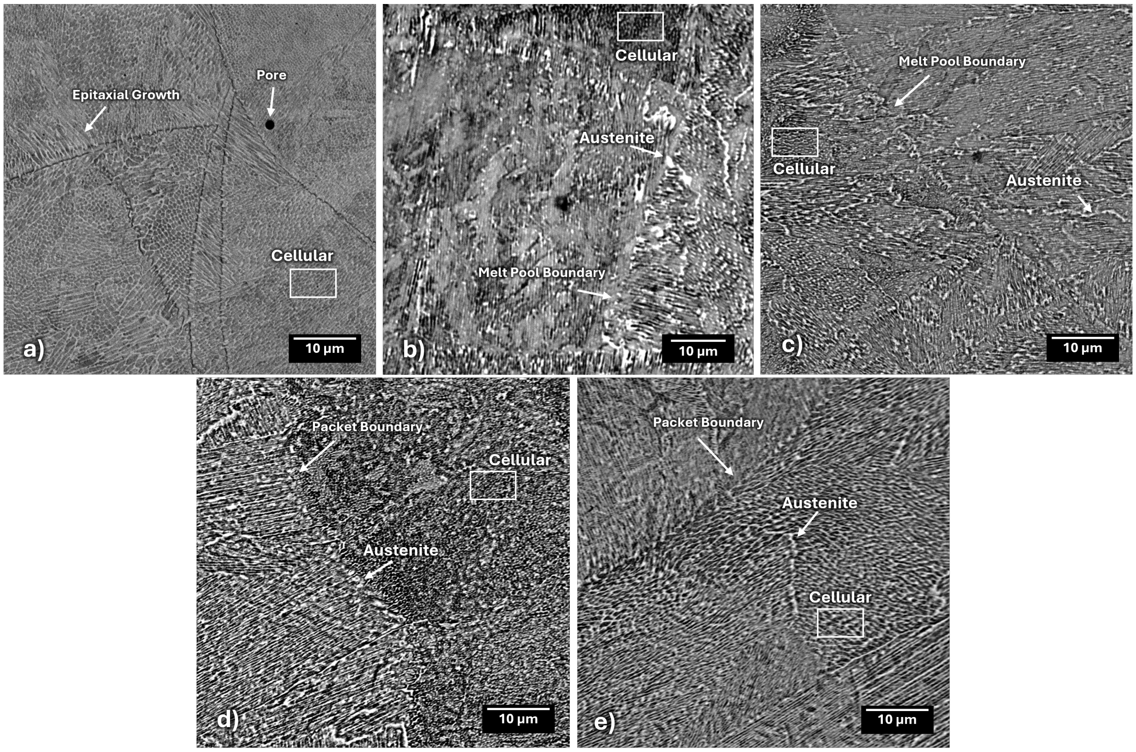

Figure 5.9 SEM-BSE images (15 KeV) of 18Ni-300 maraging steel: (a) As-Built condition; (b) DA at 490 °C for 6 hours; (c) DA at 510 °C for 6 hours; (d) DA at 530 °C for 6 hours; (3) DA at 560 °C for 6 hours.

As shown in Figure 5.9(b), the lath-shaped martensite becomes more visible, with the presence of discontinuous cellular and columnar structure boundaries after a DA treatment at 490°C. Such discontinuities can be related to the solute migration promoting the precipitation of Ni-rich intermetallic phases, as well as the transformation of martensite phase into austenite at the cell boundaries. As the aging temperature increases to 510 °C (Figure 5.9(c)), 530 °C (Figure 5.9(d)), and 560 °C (Figure 5.9(e)), the melt pool boundaries gradually disappear. Also, cellular structures and packet boundaries become more prominent and discontinuous due to the thickening of the cellular and columnar structures. This microstructural distinction indicates potential austenite reversion due to solute migration at cell interfaces, columnar structures, packet boundaries, and melt pool boundaries. For the sample aged at 560 °C, there is a coarser and thicker cellular and columnar structures when compared to the sample directly aged at 530 °C. This is mainly due to the formation of austenite in the boundary regions with greater segregation of elements such as Ti, Mo, and Ni. Austenite reversion can occur from the growth of retained austenite or the growth of new nucleated austenite sites. Thus, since retained austenite is preferentially located at chemical heterogeneous cell boundaries, it provides a fast pathway with high driving force for austenite reversion [64].

Figure 5.10 shows the Energy-Dispersive X-ray Spectroscopy (EDS) line scanning in a region of cellular structures at the studied aging temperatures. Segregation of elements (mainly Ni, Mo, and Ti) is observed in the cellular structure boundary areas for all aged conditions. It is reported in the literature that Ni is a well-established stabilizing element of austenite, while Mo and Ti reduce the martensitic transformation start temperature (M_s) for this steel, thus promoting the formation of austenite [3, 64, 74]. For sample DA490, solute migration is minimal, with only minor variation in Ni and Mo composition at the cell boundaries. The chemical heterogeneity across cell boundaries and matrix becomes more pronounced, (with Ni, Mo, and Ti composition more prominent in cell boundary regions) as the DA temperature increases. Thus, the solute migration of these elements to the cell boundary can be observed, indicating the potential formation of reverted austenite. This cellular structure becomes thicker and more prominent with increased heat treatment, from a cellular boundary length of 0.11-0.17 μm for 490 °C to 0.20-0.45 μm for 560 °C.

In summary, the as-built microstructure exhibits a lath-like martensitic matrix with high dislocation density. Retained austenite phase are found along the build direction at the melt pool boundaries [61]. Upon aging heat treatment, a change in composition at the martensite-austenite interface is reported. Locally, there is a diffusion-controlled process of segregation of elements (Ni, Mo, and Ti) in retained austenite regions, forming chemical heterogeneity at the cell and lath boundaries. Providing enough time promotes a matrix with rich and depleted regions, which will eventually lead to martensite-austenite reversion. This heterogeneity provides a fast path for austenite reversion to occur along the boundaries of cell and lath structures that already contain retained austenite, as concluded by Conde et al. (2019) [91] and Yao et al. (2023) [64].

These findings support the observations presented in Figure 5.10. This figure shows a potential segregation of Ni, Mo and Ti while depletion of Fe at cell boundaries for directly aged samples. Unfortunately, it was not possible with the microscopic techniques employed

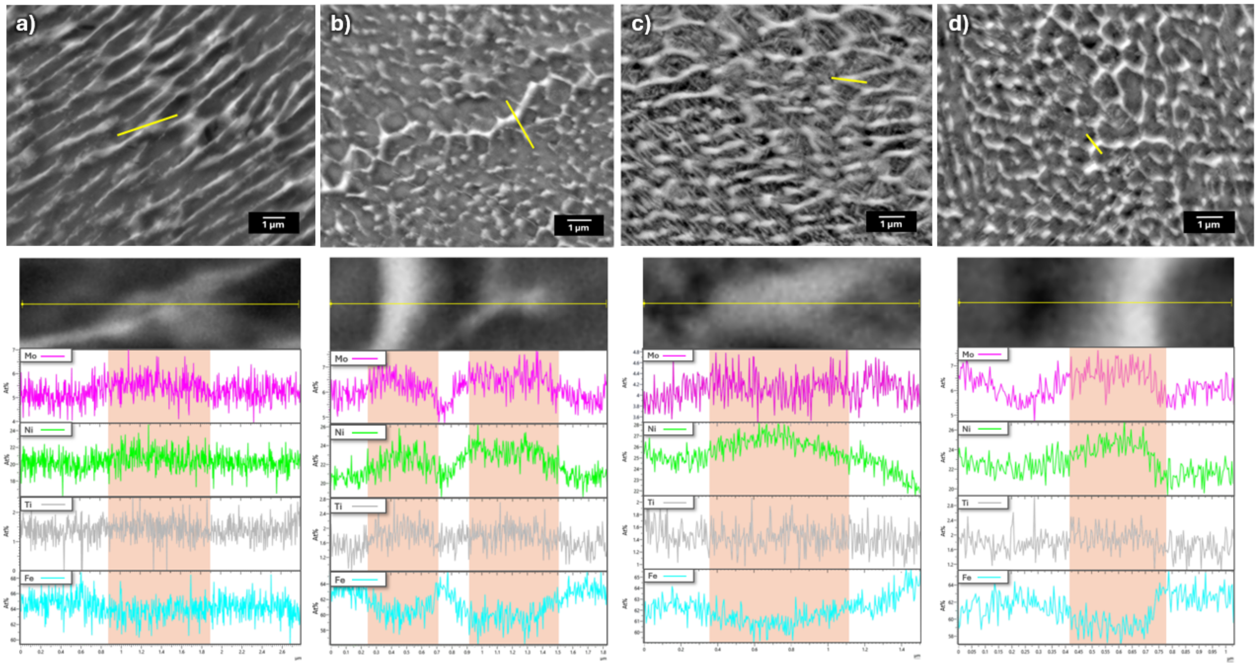

Figure 5.10 SEM-SE images (15 KeV) and EDS line scanning in a cellular structure region found in the 18Ni300 maraging steel microstructure aged for 6 hours at temperatures of a) 490°C, b) 510°C, c) 530°C, and d) 560°C. Mo, Ni and Ti and Fe profiles are extracted from the yellow lines crossing the cellular microstructures in maraging steels. Regions within cell boundaries are highlighted in pink.

in this project to observe and quantify the presence of the nanoprecipitates that lead to an increase of the material strength. At lower direct aging temperatures (such as 490 °C and 510 °C), Ni_3(Ti, Al, Mo) nanoprecipitates normally range from 20 to 60 nm in length and 5 to 8 nm in width [68]. At higher temperatures, these intermetallics become thicker until they dissolve in the matrix at 550 °C [69]. The partial dissolution of precipitates at high aging temperatures contributes to the growth of austenite through the diffusion of elements during the dissolution process. This “cooperation” between an increase in austenite content and the dissolution of precipitates leads to a decrease in the hardness of the material. It also increases the toughness of the material. More complex techniques such as TEM would be necessary to identify and quantify the presence of these precipitates, which would require greater time and expenditure to accomplish these findings. The presence of these nanoprecipitates is well reported in the literature as a major contributor to the enhanced strength properties found in L-PBF manufactured 18Ni-300 MS [7, 38, 64, 67]. The relationship between nanoprecipitates and austenite content in the microstructure, whether competitive or cooperative, in determining the mechanical properties of the material is still under discussion in literature [70]. Indeed, the mechanical results achieved here support the presence and impact of these intermetallics as will be discussed in the next section.

5.5 Room Temperature Tensile Properties

Figure 5.11 shows the triplicate tensile curves at room temperature for each DA temperature. It highlights the differences in mechanical behavior under uniaxial traction of all these metallurgical states. When compared to as-built conditions, direct aging heat treatments proved to be effective in increasing the strength of L-PBF printed samples. An increase of around 96% and 76% for YS and UTS respectively can be reached when comparing DA490 to the as-built condition. This increase comes at the expense of a drastic reduction in fracture strain, reaching a 65% decrease for DA490 sample.

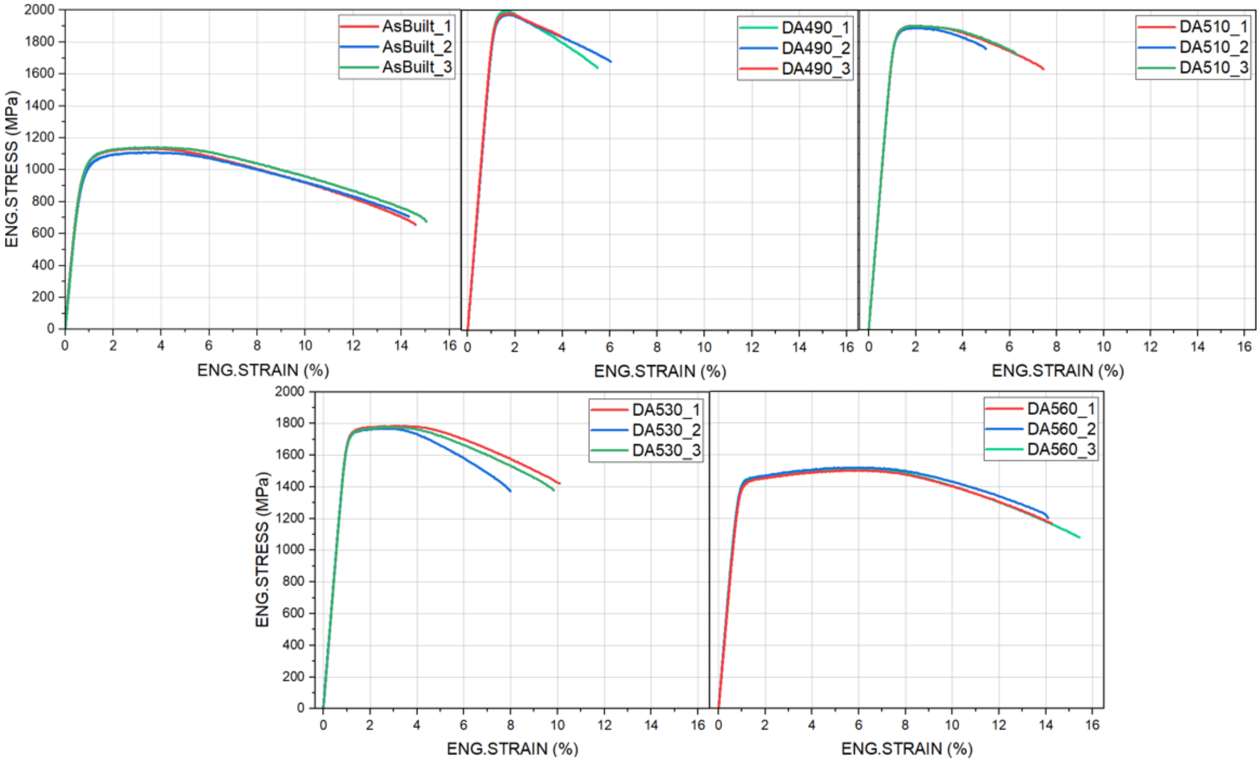

Figure 5.11 Stress-strain curves for triplicate samples at each DA temperature applied to L-PBF printed 18Ni-300 maraging steel.

The elastic behavior of the triplicates for all samples is consistent and within the expected range. A Young Modulus of approximately 160 GPa for the as-built state and of 180 GPa for all aged samples are obtained. This disparity between the Young modulus of the AB sample compared to aged conditions were also observed in other works [38, 41, 50], in which it was not fully explained. Nevertheless, one of the contributing factors reported for the increase in elastic response could be the presence of intermetallic precipitates, which limit the movement of dislocations in the metal structure [41, 50]. In the plastic deformation regime, at least one of the triplicates fell slightly outside of the expected behavior for each DA temperature. There was minor fluctuation that resulted in low fracture strain values for one of the triplicates for DA490, DA510, and DA530. This small variation will be further explained in Section 5.6 (a section referring to tensile fractography and to the exploration the features present on the fracture surfaces). Furthermore, the samples showed a reduction in the tensile strength of the material as the aging temperature is increased. This also had an impact on the fracture strain of the material, which increased significantly, reaching 15.44% for sample DA560.

A more representative graph to report the stress-strain curve for each DA temperature is plotted in Figure 5.12. This figure shows the average engineering stress-strain curve for each condition studied in the present project. Table 5.3 contains data on YS, UTS, E, and global fracture strain (El) properties taken from average stress-strain curves in the AB state and after each DA heat treatment. The local fracture strain was obtained from the DIC measurements, which were calculated just before the samples fractured. The average curves were calculated based on the separation of the data from each sample into three regions: 0 to YS, YS to UTS, and UTS to fracture. Each region is therefore normalized to obtain a fixed number of points for all triplicate curves. The average stress/strain values are then calculated point by point and concatenated to compose the average curve.

The Young's modulus response for all heat-treated samples was similar, ranging from 171 to 181 GPa. Beyond the elastic deformation domain, there is a significant difference in the plastic deformation behavior of the different materials. The YS and UTS of DA490 to DA510 decreased by about 5%, with an increase in overall fracture strain of 21%. There is a minor difference (about 2% vol.) in austenite content between the sample aged at 490 °C and the one aged at 510 °C. In both cases, it is believed that the heat treatment did not help in significantly triggering the TRIP mechanism to enhance the ductility of the material.

Table 5.3 Average tensile properties data and its standand deviation for L-PBF printed 18Ni-300 Maraging steel in AB state and after direct aging treatment.

				Fracture Strain (%)	
Sample	**Yield Strength (MPa)**	**Ultimate Tensile Strength (MPa)**	**Young Modulus (GPa)**	**Local**	**Global**
As-Built	988.94 ± 16.90	1128.64 ± 13.72	156.94 ± 1.62	115.84	14.69 ± 0.36
DA490	1942.85 ± 10.69	1981.38 ± 9.78	181.66 ± 1.25	29.51	5.15 ± 0.90
DA510	1848.09 ± 5.77	1898.86 ± 6.00	179.74 ± 1.05	31.21	6.24 ± 1.00
DA530	1721.48 ± 6.28	1777.19 ± 6.18	179.06 ± 1.05	60.70	9.30 ± 0.94
DA560	1404.52 ± 8.25	1510.92 ± 7.41	171.60 ± 3.13	68.13	14.60 ± 0.60

The strength-ductility relationship becomes more evident as the direct aging temper-

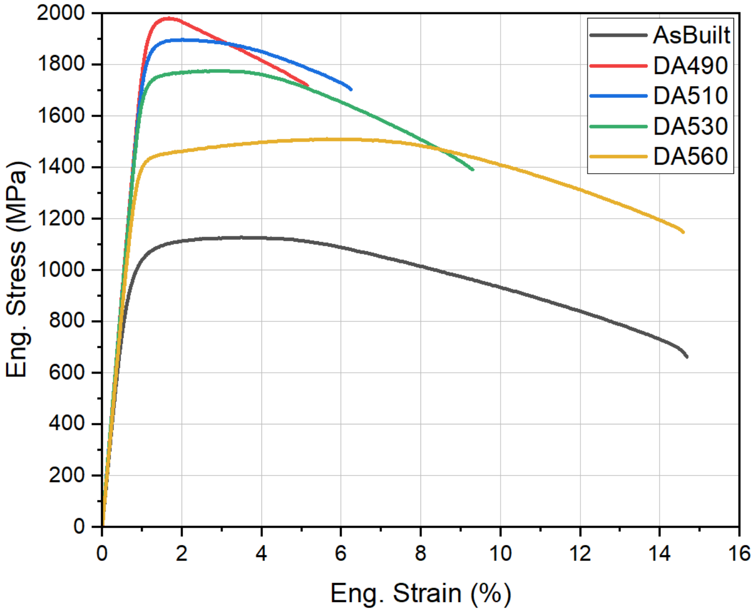

Figure 5.12 Average Stress-strain curves for AB state and each DA temperature applied to L-PBF printed 18Ni-300 maraging steel.

ature increases. When comparing DA490 with DA530 there was a small decrease of around 10-11% in YS and UTS but a significant increase of 81% in the global El. In this case, there is a greater difference in the austenite content, around 7%, which may have contributed to the improvement in the ductility of the material based on the TRIP mechanism.

For the DA560 sample, the average elongation significantly increased reaching 14.60%, similar to the as-built condition. This is accompanied by a decrease of the YS to 1404 MPa and of the UTS to 1511 MPa. This high plastic deformation behavior could be related to the presence of a significant austenite content in its microstructure, i.e. around 30% vol. (as calculated from XRD results). This potentially enables the transformation of austenite into fresh martensite during tensile deformation at room temperature. Despite DA530 and DA560 having relatively low strength values compared to the peak strength in DA490, such direct aging heat treatment should be considered as an interesting option for modulating the microstructure of maraging steel for plastic molding tooling applications. Such high temperature DA heat treatments offer better mechanical strength than the AB material, while maintaining similar ductility, thus contributing to the material's toughness.

Figure 5.13 shows the average values of all the collected data from the literature for UTS (a) and elongation (b) as a function of the direct aging temperature for 5-6 hours [4, 5, 38, 62, 67, 68, 73, 74]. A comparison is made with the results obtained in the presented project. Firstly, this figure demonstrates that our data are consistent with those reported in the literature. The trend line shows that beyond 490 °C, UTS noticeably drops while El increases correspondingly as the direct aging temperature is increased. Most data coming from the literature for temperatures above 500 °C are coming for single sources. This explains why there is more dispersion in the data and why some average values slightly deviated from the trend line (represented by the solid black line in these graphs). **As datasets above this temperature are currently limited in the literature, this study is of utmost importance for better understanding the mechanical response behavior of this maraging steel under high temperature DA treatments.** This is particularly noticeable at higher DA conditions such as 530 °C and 560 °C, where the coupling of UTS and El proves to be appealing for industrial application requiring a compromise between strength and plastic deformation (i.e. relatively high strength while allowing high plastic deformation).

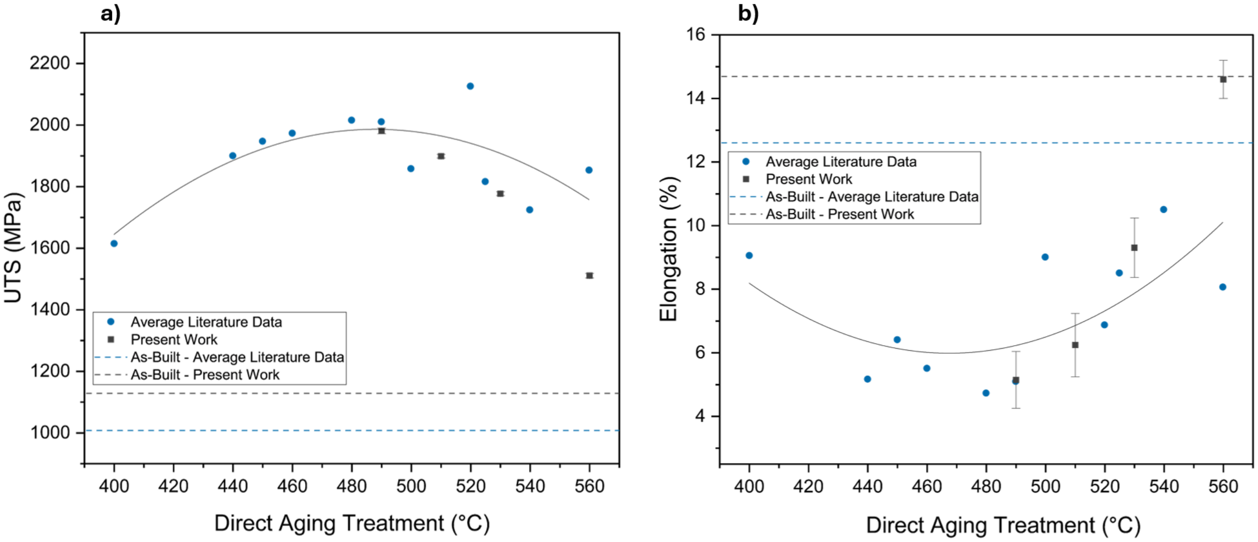

Figure 5.13 Comparison of present work with average UTS and Elongation data collected from the literature for each direct aging temperature for 5-6 hours [4, 5, 38, 62, 67, 68, 73, 74]. Solid black line corresponds to polynomial fitting.

The plasticity improvement due to the TRIP effect at high DA temperatures can be seen from the strain hardening perspective. Figure 5.14 shows the instantaneous strain hardening coefficient (n_i) in relation to true strain (ε) for each DA temperature associated to each average true stress-strain curves. For DA490, the strain hardening coefficient value decreases sharply as true strain increases. This indicates that there is almost no strain hardening mechanism contributing to plastic deformation in this case. In fact, this DA heat treatment resulted a hard martensitic matrix with minimal austenite fraction. This exceptional hardness and resistance could be associated with the presence of second-phase intermetallic

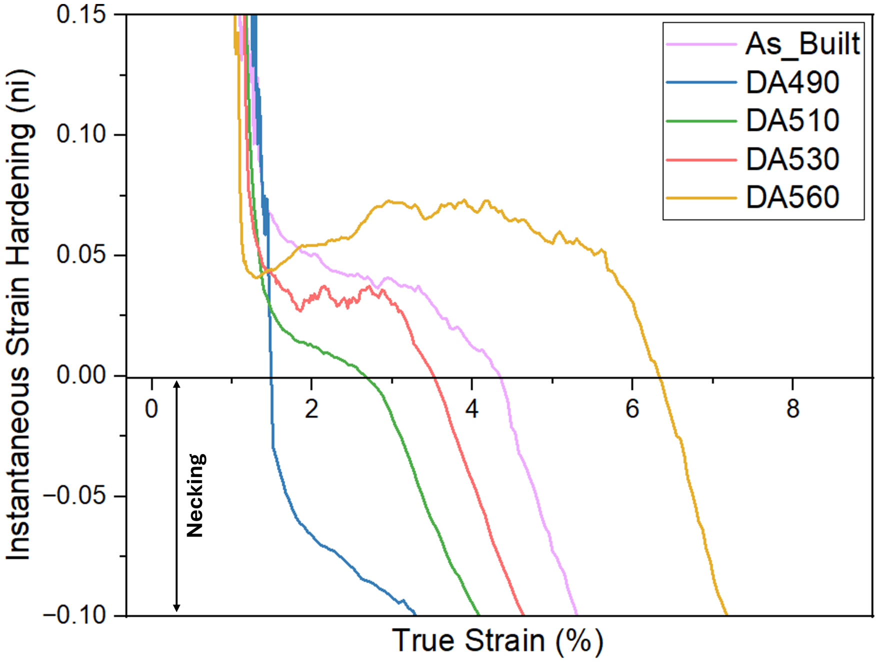

Figure 5.14 Instantaneous strain hardening coefficient as a function of true strain for 18Ni-300 MS samples in AB condition and aged from 490 to 560 °C.

precipitates that introduces mechanisms that hinder the movement of dislocations. These mechanisms are impacted by the type of intermetallics, their size and strength. Their presence typically results in an increased resistance at the expense of the elongation [38]. As the DA temperature increases, there is a noticeable increase in the strain hardening coefficient curve until it reaches positive coefficient values. One possible explanation for this outcome could be the contribution of the TRIP effect. It transforms both the austenite formed upon solidification (i.e. retained austenite) and during the aging state (reverted austenite) into fresh martensite upon plastic deformation. By maintaining a high strain hardening coefficient, this effect postpones the critical point where deformation becomes localized, ultimately delaying the onset of failure [92].

This becomes more evident when comparing the AB sample with the DA560 condition. Both samples have virtually the same elongation. However, the evolution of the strain hardening coefficient, $dn_i/d\varepsilon$, is showing an opposite behavior. For the AB sample, which has an almost fully martensitic microstructure (i.e. only about 1.6% austenite in volume), $dn_i/d\varepsilon < 0$. For the DA560 sample, $dn_i/d\varepsilon > 0$ for a portion of the plastic region between YS and UTS. This shows that a hardening mechanism such as TRIP could be playing a crucial role in the plasticity behavior. In this case, the high austenite content available for transformation in this sample (about 30% vol.) is at the origin of this behavior. For DA490 condition, there is a drastic decrease in the strain hardening coefficient up to the fracture of the sample. As for DA510, DA530 and DA560, these heat treated samples gradually show higher recovery in the strain hardening coefficient before the necking regime. Thus, the combined effect of intermetallics dispersion and of the high fraction of austenite contribute to strain accommodation until UTS.

The strain distribution during uniaxial tensile testing was evaluated in depth using the DIC technique. For all AB and DA samples, the strains distribution along the surface remained nearly uniform during the elastic and uniform plastic deformation stages. Figure 5.15 shows the surface strain distribution just before fracture, showing the maximum magnitude of local strain. Sample AB shows a large necking region along its diameter near the fracture area which exhibits a large strain map (reaching approximately 116% of local fracture strain). For the DA490 sample, necking is less prominent due to the higher strength and lower elongation of the material, since the potentially high presence of nanoprecipitates

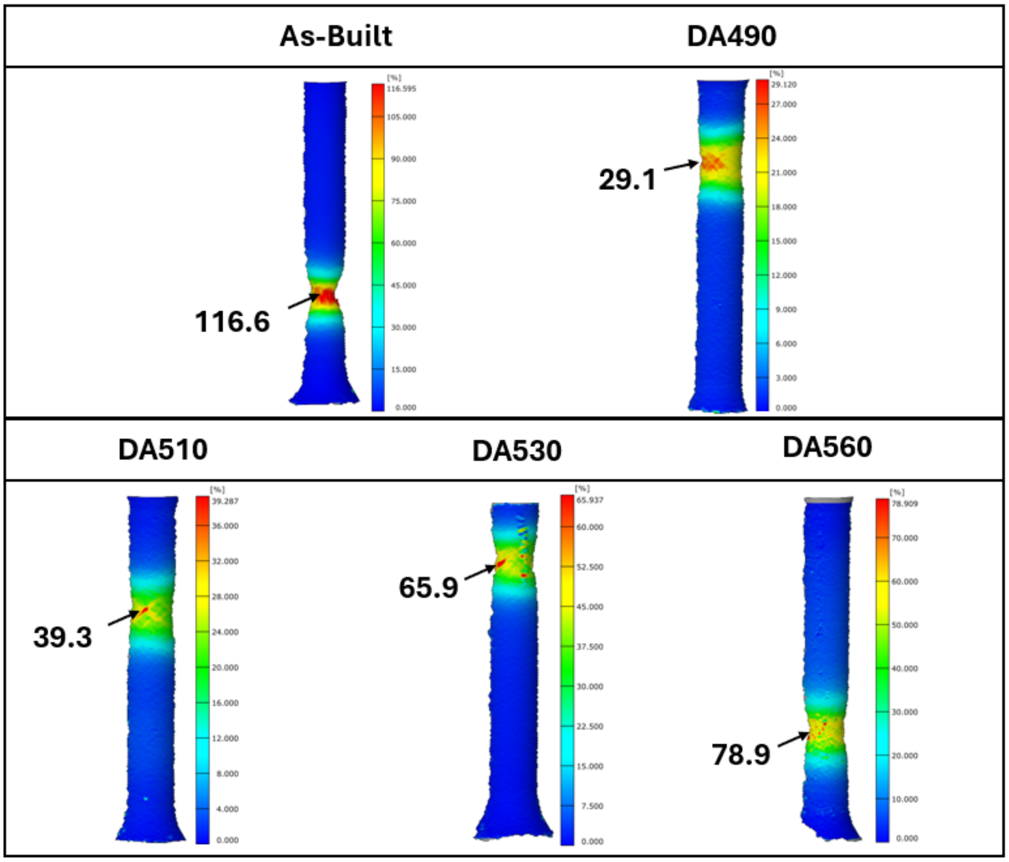

Figure 5.15 Distribution of the surface strains just before fracture for the AB and directly aged 18Ni-300 MS samples processed by L-PBF (one sample is presented per condition for better visualization).

in the matrix can block the dislocations motion [3]. As soon as the material reaches its UTS quickly after yielding, it lacks the ability to further strain-harden. Thus, the strain distribution region still forms a strain band for the DA490 sample. This indicates a high stress concentration across the necking diameter, characterized by rapid localized failure. As the DA temperature increases, the stress concentration becomes more prominent at specific spots along the strained region. For the DA560 sample, the presence of small strain spots distributed along the strain range is very clearly noticed. As soon as plastic instability begins, a neck forms, causing the local strain rate to increase relative to the rest of the specimen. Such material may exhibit strain rate sensitivity, in which this high local strain rate increases the local flow stress, providing a critical buffer that allows deformation to spread to adjacent regions with lower strain rates. Thus, extending the total elongation and promoting localized stress concentration sites that may promote fracture initiation. Local strain also increases from 29.1% to 78.9% as the aging temperature increases. This indicates that the material has increased its plastic response during tensile loading. This shift from fracture initiation in a deformation band prior to fracture to specific stress concentration points shows that our maraging steel, when exposed to lower aging temperatures, cannot withstand greater deformations. In fact, small surface defects are sufficient to create a stress concentration region capable of abruptly fracturing the material. At higher aging temperatures, the resulting material accommodate the strain, potentially due to the TRIP effect, by providing strain hardening through phase transformation, and strain rate sensitivity mechanism that enables strain rate-dependent strengthening.

In general, the reported results show that direct aging plays a significant role in the strength-ductility relationship of the material. The DA530 and DA560 samples proved to be good candidates for obtaining high strength while exhibiting good elongation properties (which properties can be of interest for injection molding and aerospace applications). These properties can be attributed to the rapid cooling rate associated with the L-PBF process. Such ultra-high solidification rate promotes solute segregation. This, in turn, stabilizes austenite at room temperature after printing. As the printed microstructure is aged, Ni_3(Ti, Mo, Al) intermetallics potentially enhance strength by dislocation movement hindrance. By increasing the DA temperature, the presence of retained austenite and solute segregation increases the kinetics of austenite reversion. The greater austenite stability (due to solute migration) combined with plastic deformation applied during quasi-static tensile testing can potentially result in the transformation of reverted austenite into fresh martensite. The TRIP effect is further enhanced by the greater fraction of austenite in the microstructure. This ultimately results in greater strain accommodation, thus improving the plastic response of the material.

5.6 Tensile Fractography

The broken specimens after tensile tests were observed using SEM to perform a fracture surface analysis. The samples with the worst performance regarding strength/elongation were selected to investigate the origin of data variance among triplicate measurements. Figure 5.16 shows the fracture surface of the as-built and aged sample at 490 °C, respectively. It can be observed that the as-built sample undergoes significant plastic deformation, with a reduction in cross-sectional area. The fracture appears as a 45-degree shear surface at the specimen boundaries, characteristic of ductile deformation of the material. In addition, dimples were found on the fracture surface, which develop from the coalescence of small voids present in the material structure. EDS analysis of particles (yellow arrows) present in the surface revealed a chemical composition consisting mainly of O, Ti, Al, and Fe for both metallurgical states. This may indicate the presence of oxides in as-built and heat-treated samples in 18Ni-300 MS.

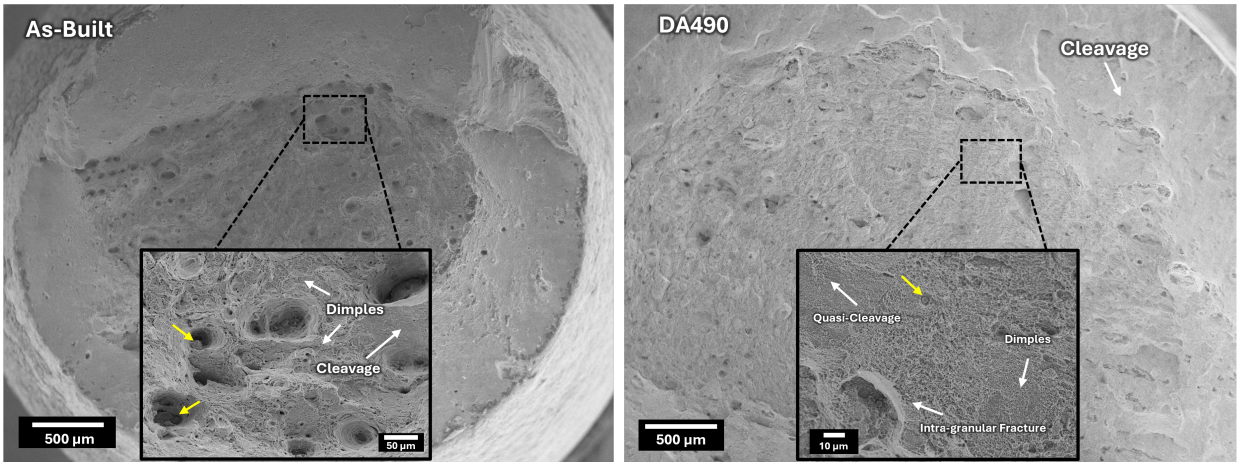

Figure 5.16 Fracture surface analysis for As-Built and direct aged at 490°C samples (DA490), respectively. Yellow arrows indicate inclusions found on the surface of the sample.

After aging at 490 °C (Figure 5.16 - right panel), mechanical resistance increases to the maximum. This significantly affects how plastic deformation occurs. Necking is almost imperceptible with nearly no prior plastic deformation. Thus, the surface is characterized as being flat and smooth, with few dimples in the fracture structure. Intragranular fractures are also noted due to the rapid propagation of cracks promoting faceted surfaces. Some minor oxide inclusions (yellow arrows) were found scattered throughout the fracture structure of the samples, which could promote crack propagation by disruption of cohesion between matrix-inclusion.

Figure 5.17 shows the surface fractography of DA510 and DA530 samples, respectively. For DA510 sample, crack propagation through voids is visible, indicated by the red arrow. The crack initiated on the surface of the specimen. This zone has a higher tendency to contain defects and imperfections (such as surface rugosity) that can act as initiation points for crack propagation. A clearly visible pore path (likely an L-PBF printing defect which may have been caused by poor powder distribution and inadequate powder bed fusion) can be seen on this figure. This well-defined void path for the crack to propagate is likely the main factor that caused this specimen to have the lowest elongation value and a different mechanical response. Ti and Al oxide inclusions were also found in this sample. For DA530 sample (figure 5.17 - right panel), a large inclusion (around 50 μm) is visible on the surface of the sample diameter, with a main chemical composition of O, Ti, Al and Fe. This indicates that an oxide rich in Ti and Al likely contributed to the crack initiation that caused premature failure when compared to the other triplicates for this heat treatment condition. A greater reduction in diameter and a more pronounced plastic deformation can be detected by DIC measurements for this sample as well.

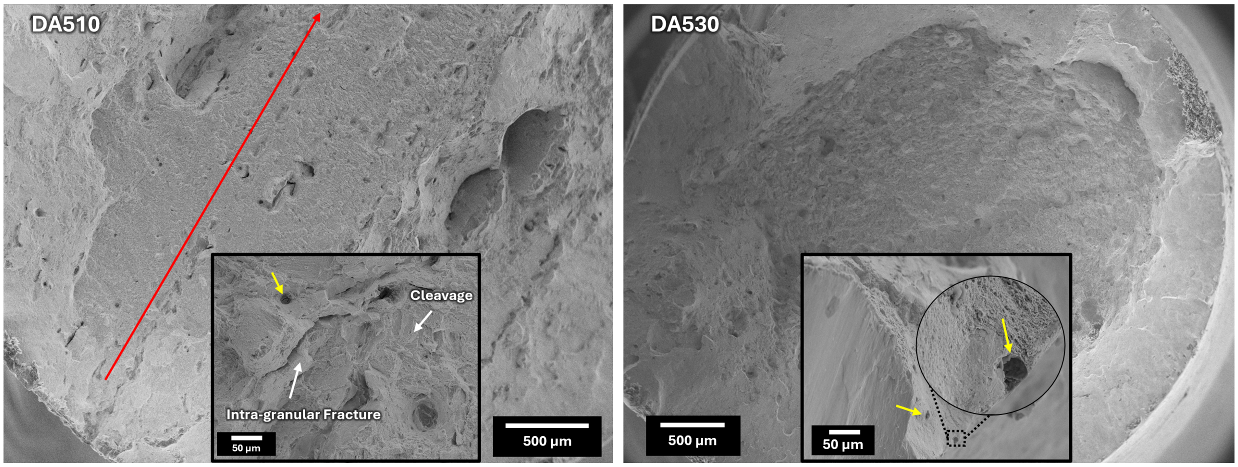

Figure 5.17 Fracture surface analysis for direct aged at 510 °C (DA510) and 530 °C (DA530) samples, respectively. Yellow arrows indicate inclusions found on the surface of the sample. The red arrow indicates the void path from the surface to the center of the fracture.

For the sample aged at 560°C (Figure 5.18), plastic deformation is significant, with pronounced necking characteristics. The fracture surface shows dimples, indicative of the material's plastic response. Inclusions were observed with EDS analysis pointing to (Ti, O, Fe, and Al)-rich oxides. These oxides are also present in the microstructure of the polished samples characterized by OM and SEM. These oxides were already observed and reported in the literature for 18Ni-300 MS powders printed by L-PBF. Fluctuations in the inert shielding environment during the AM process can trigger oxidation of Ti and Al, which have lower oxidation thresholds than other alloying elements in maraging steels [81, 93]. Due to the lower density of these Ti-Al oxides compared to the molten alloy, they moved upwards (i.e. they float) until they reach the surface, where they accumulate at the peripheries of the melt tracks. With the remelting of subsequent layers and rapid solidification, the growth and agglomeration of oxides is hindered and thus they are retained as small inclusions in the steel [59].

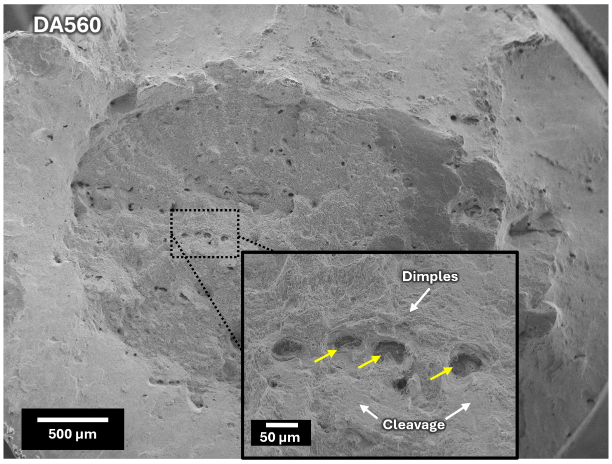

Figure 5.18 Fracture surface analysis for direct aged at 560 °C (DA560) 18Ni-300 maraging steel sample. Yellow arrows indicate inclusions found on the surface of the sample.

5.7 V-Notch Impact Charpy Test

Table 5.4 summarizes the average absorbed energy (J) of the triplicate samples for each Charpy impact test temperature for the as-built and heat-treated conditions. The soft and heterogeneous microstructure of the as-built sample clearly affected Charpy impact energy across the entire temperature range. At temperatures of -100 °C, martensite becomes brittle, creating new crack initiation sites that propagate rapidly through the matrix. As the test temperature increases, the material absorbs more energy and better accommodates impact stresses. A high standard deviation was observed in the as-built state for temperatures between 0 °C and 200 °C. This was due to manufacturing microstructural heterogeneities and the presence of porosities in the microstructure. As-printed additively manufactured structures are highly dependent on the porosity present in their structure. They significantly influence the energy absorbed by the material during impact tests. The Charpy impact energy at room temperature (25 °C) obtained in this work is consistent with the values found in the literature for the 18Ni-300 MS alloy with 1% porosity and similar printing process parameters [77]. This is a clear indication that process parameters must be optimized to achieve minimum porosity, while heat treatment homogenizes the microstructure and improves mechanical properties.

Table 5.4 Average V-Notch Charpy Impact energy data and its standard deviation for L-PBF printed 18Ni-300 Maraging steel in AB condition and after direct aging treatment.

	Charpy Impact Energy (J)					
Sample	**-100 °C**	**-50 °C**	**0 °C**	**25 °C**	**100 °C**	**200 °C**
As-Built	31.64 ± 0.78	45.65 ± 2.07	67.79 ± 8.89	79.54 ± 7.47	93.55 ± 10.24	86.32 ± 14.50
DA490	7.23 ± 0.78	10.39 ± 2.07	11.98 ± 1.41	11.30 ± 1.57	10.39 ± 0.85	9.49 ± 0.00
DA510	8.13 ± 0.68	11.07 ± 0.39	12.20 ± 0.68	12.65 ± 1.04	11.52 ± 0.68	10.39 ± 0.78
DA530	9.72 ± 1.41	11.07 ± 1.71	13.78 ± 1.04	14.24 ± 1.36	14.24 ± 1.17	14.46 ± 0.39
DA560	9.72 ± 0.39	13.11 ± 1.96	16.95 ± 1.36	17.85 ± 1.04	20.79 ± 0.39	24.63 ± 1.04

After direct aging heat treatment, Charpy impact energy drastically decreases, reaching its lowest value at a test temperature of -100 °C for a sample heat treated at 490 °C. Under these conditions, there is a high density of nanoprecipitates and minimal austenite fraction. This microstructure results in peak hardness and strength at the expense of material toughness. At cryogenic temperatures, the material becomes extremely brittle, delivering low absorbed energy values due to rapid crack propagation. Figure 5.19 shows a comparison between the Charpy Impact Energy obtained under the DA conditions imposed in the present project and those reported in the literature for Charpy tests performed at room temperature. It is evident that our results are consistent with those reported in the literature for the DA temperature ranging from 490 to 560 °C. The measured maximum absorbed energy value at room temperature reaches 17.85 J. This corroborates the finding that under overaging heat treatment conditions, the microstructure becomes softer, likely as a result of the dissolution of nanoprecipitates in the matrix. This is accompanied by a high volume fraction of austenite, which is beneficial for the toughness of the material (even though it reduces its strength).

The Charpy test is highly dynamic in nature. It has a high impact loading rate when compared to quasi-static tensile tests. As a result, samples shows low absorbed energy values and a different behavior when studied via Charpy tests. This difference indicates that the austenite has minimal impact on plastic deformation, while it promptly transforms into martensite (immediately passing into the unstable phase of crack propagation) during high impact loadings. The greater Charpy impact energy of the DA560 samples can be explained mainly by the dissolution of the nanoprecipitates in the microstructure which increases the matrix softness. Unstable austenite can then quickly transform into brittle martensite during the initial deformation stage. This introduces new sites for crack nucleation, decreasing the absorbed energy. **Future research should analyze the differences in TRIP mechanisms between tensile and impact tests for directly aged maraging steels**.

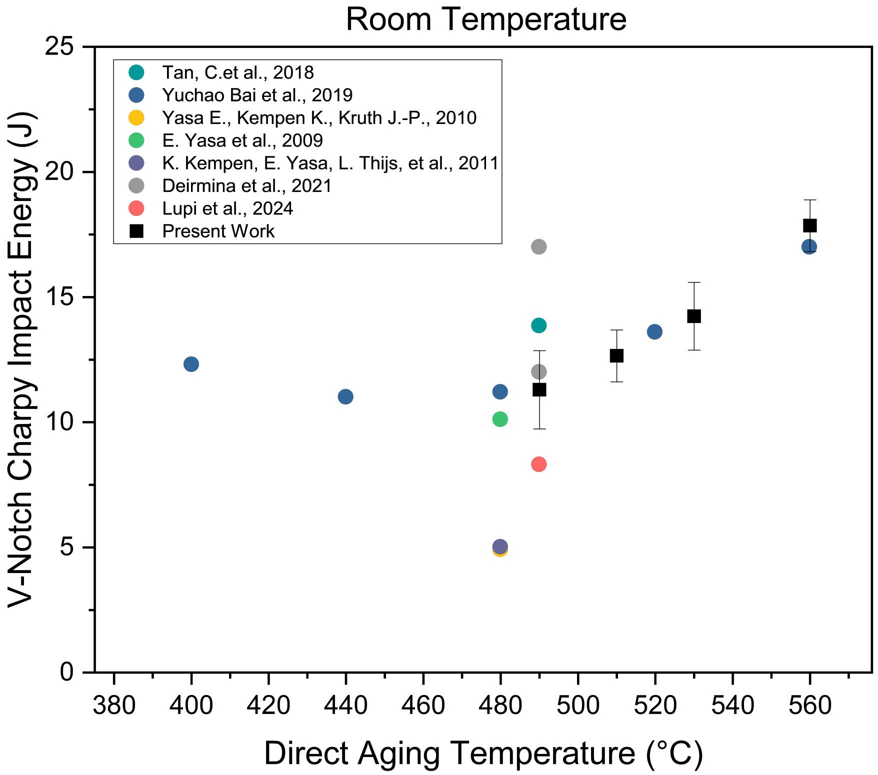

Figure 5.19 Comparison between present work and literature data for Charpy Impact Energy under different with Direct Aging temperatures for 5-6 hours [50, 62, 67, 78–81].

Post-mortem investigations of tensile and impact specimens should be performed. More specifically, one should determine the relationship between austenite fraction and stability with TRIP mechanism. Recent research has been conducted in this direction. As an example, Li et al. (2024) [65] investigated the impact of the chemical heterogeneity of austenite on the cryogenic toughness of L-PBF maraging steel. In their work, they managed to increase the impact toughness by tuning the austenite stability.

Figure 5.20 shows the fracture surface of the room temperature impact samples for each DA condition. The fracture started at the root of the notch for all specimens. This is due to the stress concentration of the pendulum hitting the sample in this zone. For the as-built sample, significant and relatively symmetrical shear lip surfaces can be identified from the yellow dashed line drawn on the image for better visualization. These shear lip surfaces are formed when the material is able to absorb a great amount of energy as it deforms due to shear stress. The shear lip surfaces are not as pronounced for directly aged samples (which also have lower toughness). The fracture surface of the samples are smooth and flat. This is characteristic of a brittle fracture in which the crack rapidly propagated. It is also evident from this figure that the shear lip surface increases as the direct aging temperature increases.

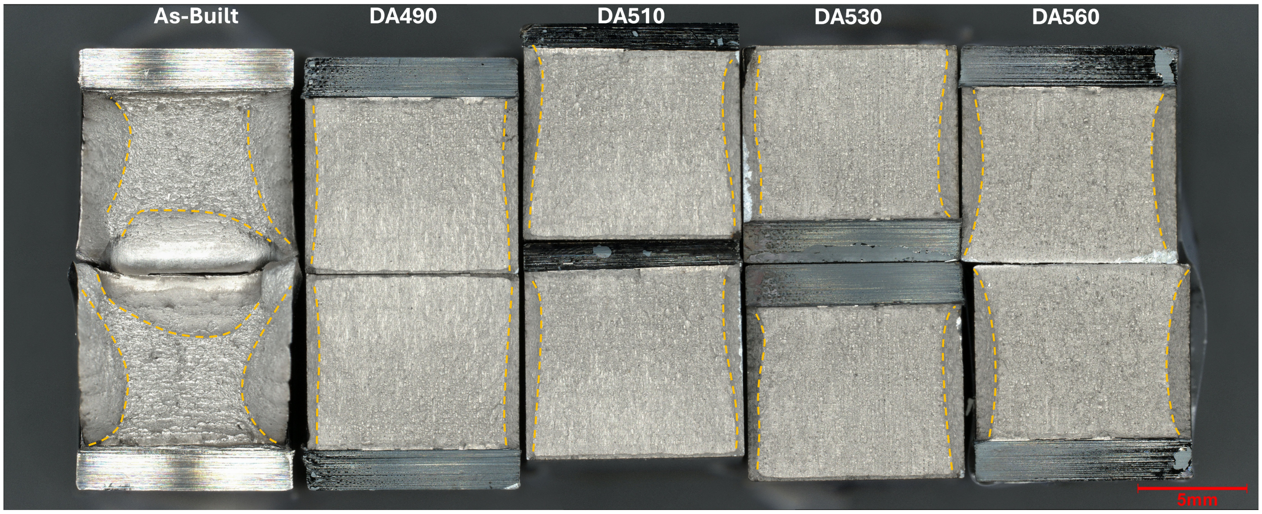

Figure 5.20 Fracture surface from Charpy impact specimens at room temperature test of LPBF-printed maraging steel. Yellow dashed line added for visual ease of the shear lip surfaces.

The DA560 sample allowed greater energy absorption, despite having most of its fracture surface smooth and flat.

Figure 5.21 shows the Charpy impact energy as a function of the test temperature for the as-cast and directly aged L-PBF 18Ni-300 MS samples. Data were fitted according to Boltzmann-like functions. It can be observed that the as-built sample presents the maximum impact toughness combined with low strength (see tensile test results). These results for the as-built sample are caused by its soft martensitic microstructure. Even at cryogenic temperatures, its Charpy impact energy reach values of around 31 J (even by having a brittle structure). The DBTT of the as-built sample occurs around -21 °C. It reaches a maximum Charpy impact energy of 93.55 J at 100 °C. For the DA490, DA510, and DA530 directly aged samples, the DBTT gradually shifts to lower temperatures of -62.5 °C, -61.9 °C, and -34 °C, respectively. At cryogenic temperatures, all aged samples performed similarly, reaching a maximum absorbed energy of about 10 J. At temperatures above 0 °C, samples DA490, DA510, and DA530 performed better. They absorb more energy despite being already in their ductile plateau. The DA560 sample had the best toughness performance among the heat-treated samples, with a DBTT of -1.33 °C. At cryogenic temperatures, this sample performs similarly to the DA490 and DA510 samples tested under high temperatures. This heat treatment is therefore a good option for maraging steel applications that require toughness at low temperatures. This heat treated material performed well at high temperatures as well. It reached values above 20 J for test temperatures of 100 °C and 200 °C (which

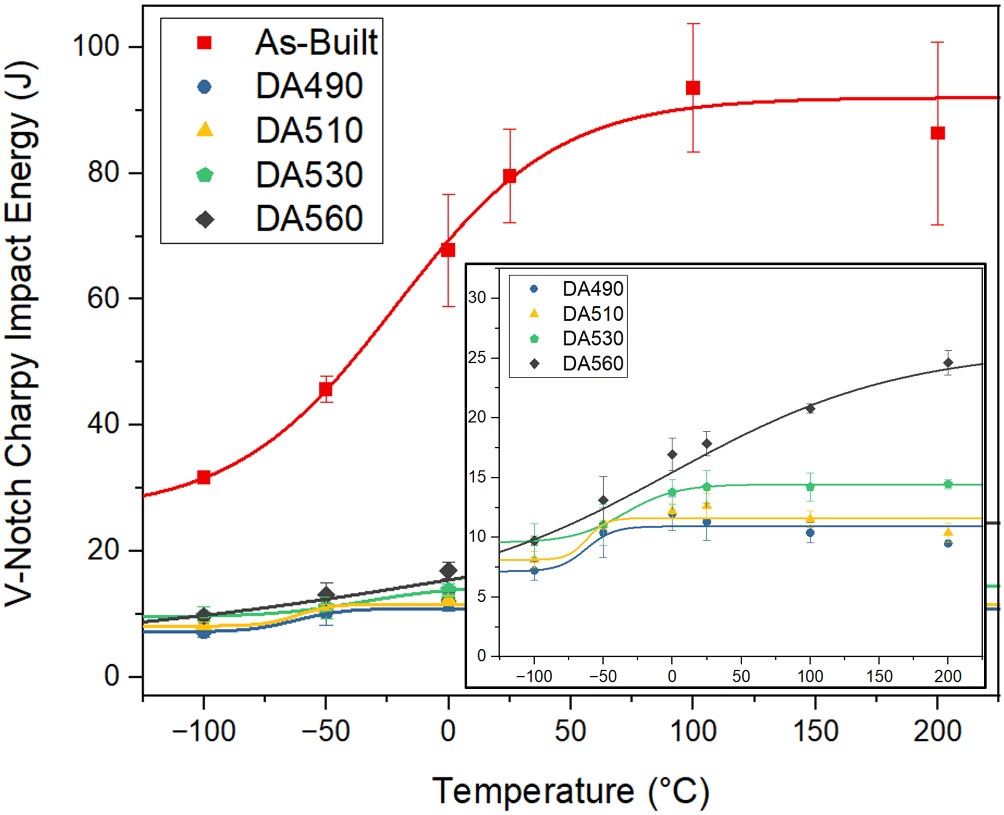

Figure 5.21 Charpy Impact Energy of the LPBF-printed 18Ni-300 MS directly aged samples as a function of temperature. The curves were fitted according to the Boltzmann function.

may be beneficial for plastic injection molding applications operating at high temperatures). As discussed earlier, the rapid transformation from unstable austenite to martensite at the beginning of the fracture stage allows for rapid crack propagation and lower absorbed energy values. At high temperatures, the crack usually settles more into the displacement. This requires more energy to propagate the crack thus increasing the material impact toughness. It is also worth mentioning that considerable difference in absorbed energy between quasi-static tests and high-rate impact tests are observed. As a result, fracture mechanisms and their relation with the material microstructure differ. This is an important topic that could be further explored in future research.

To date, there is no study in the literature which reports the Charpy impact energy at different test temperatures for 18Ni-300 MS manufactured by L-PBF for directly aged samples. **This is therefore the first scientific work that provides these DBTT curves.** Although these values are relatively low when compared to maraging steels manufactured by conventional processes (37 J at 25 °C [2]), our results show good agreement with the literature for L-PBF printed maraging steels applied at room temperature. We are therefore confident in the quality of the results we are providing to the literature. The DBTT curves prove to be a good benchmark for industry reference for low/high temperature applications. Based on this study, future investigations may be conducted to improve the toughness of the material by fine-tuning both the L-PBF process and the heat treatment parameters to trigger the TRIP effect to a larger extent. This could open opportunities for achieving an optimal strength-toughness ratio for different maraging steels.

In summary, increasing the DA temperature from 490°C to 510°C did not prove to be highly effective and is not recommended. It resulted in minimal improvement in toughness for both the tensile and the impact Charpy properties. This is due to the small differences in austenite fraction available to boost the TRIP effect. Higher direct aging temperatures seem promising. DA530 and DA560 showed a favorable strength-toughness ratio, making them suitable candidates for achieving greater toughness at the expense of small reduction in tensile strength. DBTT also shifted to higher temperatures and higher energy absorption values under these conditions. Care must be taken when trying to control the material microstructure with heat treatment since toughness properties of the 18Ni-300 MS alloy are strongly dependent on the loading rate.

CHAPTER 6 CONCLUSION

Modulating direct aging parameters has emerged as an effective strategy for increasing the toughness of maraging steel through the control of the presence of nanoprecipitates and the growth of reverted austenite. This can be achieved through a diffusion-controlled heat treatment process involving the segregation of elements (such as Ni, Mo, Ti) in the boundary regions of the columnar and cellular structures of the martensitic matrix. This chemical heterogeneity between the matrix and the boundary regions increases the stability of reverted austenite. It ultimately leads to greater material toughness as a result of the TRIP effect occurring under stress loading (a topic of great interest in literature). The current literature emphasizes on the diffusion mechanisms in the maraging microstructure and its impact on tensile properties. Limited attention is given to the impact toughness and the role of the TRIP effect. In fact, to our knowledge, there are no ductile-brittle temperature transition curves in the literature reported for the 18Ni-300 MS alloy manufactured by L-PBF and directly aged.

To this end, the mechanical behavior of tensile and impact strength at direct aging temperatures between 490 °C and 560 °C could be further explored. In this study, 20 rectangular prism-shaped coupons were manufactured from 18Ni-300 MS powder using L-PBF technology integrated with high-speed milling. Based on optimized process parameters using a bidirectional laser scanning strategy with a 90° rotation after each printed layer, the coupons were manufactured and subsequently machined. The main objective of this project was to verify the impact of direct aging treatment (490 °C, 510 °C, 530 °C, and 560 °C for 6 hours) on tensile properties and impact toughness behavior of the material.

An in-depth investigation was conducted based on the printed coupons, analyzing the relative density of the as-built sample, quantifying phase fractions based on XRD measurements, and performing microstructural characterization to identify the relevant metallurgical features present in each studied condition. In addition, hardness and tensile tests were conducted to verify the quasi-static mechanical properties of the printed materials and to relate them to their respective microstructure. Charpy impact tests were also performed to construct a Ductile-Brittle Transition Temperature curve for additively manufactured maraging steel.

6.1 Summary of Works

A summary of the main findings is provided below.

- The 18Ni-300 MS powder used in this project had an apparent density of 4.28 g/cm^3 and a flowability of 23 s, demonstrating flowability properties that help in powder dispersion during printing. However, the presence of large irregular particles may have contributed to the obstruction of the powder during powder spreading by the printer during trials without powder dehumidification.
- The particle cohesion index proved to be a good parameter for indicating the need for powder dehumidification before each printing, thus improving free flow behavior. There was a decrease in the cohesion index after dehumidification, with a small dispersion values caused by mechanical interlocking of satellite particles and large irregular particles. Thus, the dehumidification process resulted in better dispersion of the powder for the formation of a uniform and homogeneous layer.
- After printing, the relative densities for the printed samples were relatively high, reaching a maximum of 98.94%. The presence of a wide particle size distribution and irregular particles contributed to the formation of pores during material densification. This may have affected some tensile specimens that showed high dispersion of elongation values, caused by crack propagation in the direction of a well-defined pore path.
- As-built samples presented an average hardness value of 370 ± 3 HV, consistent with the literature. This hardness is the result of a fine soft martensitic microstructure, characterized by rapid solidification. With direct aging, the hardness reaches a peak of 596 ± 5 HV at 490 °C. With an increase in direct aging temperature, hardness follows a decreasing trend until reaching a minimum of 466 ± 3 HV at 560 °C, due to the increase in austenite content, which made the microstructure softer. Optimized printing process parameters contributed to a good solidification and consistent hardness values across the entire hardness test area.
- The AB microstructure has a predominantly martensitic matrix (approximately 1.66% in vol. of austenite), with fine cellular and columnar structures and melt pool boundaries. These are characteristic features of a high thermal gradient during the solidification process. The DA490 sample already shows partial dissolution of the cellular structures due to the migration of solutes and the formation of austenite at the cell interfaces and melt pool boundaries. There was an increase in austenite content up to

11.41% vol. due to the reversion of martensite to austenite. With the increase in aging temperature, the austenite volume reached up to 29.88% vol. for sample DA560, with the disappearance of the melt pool boundaries but thickening of cellular and columnar structures boundaries.

- Segregation of elements (mainly Ni, Mo and Ti) was observed in the cell interface regions for all directly aged samples. This chemical heterogeneity between the matrix and boundary regions provides a fast path for austenite reversion. It was observed that the cell boundary length ranged from 0.11-0.17 μm for 490 °C to 0.2-0.45 μm for 560 °C. However, it was not possible to properly identify the hard nanoparticles precipitated in the matrix due to their nanometric size, requiring more sophisticated characterizations methods.

- Compared to the AB state, the heat-treated samples proved to be effective in increasing the strength of the L-PBF printed samples, achieving 96% and 76% increase in YS and UTS compared to the AB condition. However, this increase comes at the cost of a drastic reduction in fracture strain, especially for the DA490 sample with maximum strength. The strength-ductility relationship becomes more evident as the direct aging temperature increases. There was a reduction of about 10-11% in YS and UTS comparing DA490 with DA530, but a significant increase of around 81% in elongation, driven by an increase in austenite content of about 7%. For DA560, there was a 24% reduction in UTS compared to DA490, but an massive increase to 14.60% in elongation. This high plastic behavior originated from the higher austenite content (reaching about 30% in these heat treatment condition). This behavior becomes more evident when analyzing the instantaneous strain hardening coefficient (mainly for the DA530 and DA560 samples). In this case, the recovery of the hardening coefficient occurs more pronouncedly. This shows that a hardening mechanism such as TRIP is likely playing a crucial role in the plasticity behavior, mainly for the deformation accommodation up to the UTS. As a result, direct aging temperatures of 530 °C and 560 °C could be attractive candidates for a good strength-toughness ratio, particularly for quasi-static aerospace applications and tooling manufacturing, exhibiting better strength than as-built samples while maintaining similar elongation.

- The Charpy impact energy at room temperature of our maraging steel for the as-built condition is consistent with values found in the literature (reaching 79 J). At high temperatures, it reached maximum values of around 93 J, with a predominantly ductile fracture with prominent dimples on the fracture surface. With direct aging, impact resistance drastically decreased, reaching the lowest value of 11 J for the room temperature test after a heat treatment at 490 °C. This could be explained by the high density of nanoparticles and the small fraction of austenite. The DA560 sample obtained the highest absorbed energy for the room temperature impact test among all the aged samples (i.e. about 18 J). This could be explained by the dissolution of the nanoprecipitates and the higher austenite content. These data are consistent with findings in the literature, confirming the good methodology applied in this project.

- Based on the Charpy impact energy curves of the aged LPBF-printed maraging steel samples as a function of temperature, the DBTT of sample AB occurs at -21 °C. For directly aged samples, such as DA490, DA510, and DA530, the DBTT shifts to lower temperatures of -62.5 °C, -61.9 °C, and -34 °C, respectively were obtained. These samples reached a plateau of absorbed energy after 0 °C, with the highest value for sample DA530 reaching about 14 J. Sample DA560 showed the best performance in terms of resistance among the heat-treated samples, with a DBTT of -1.33 °C. At cryogenic temperatures, this sample performs similarly to the DA490 and DA510 samples at high temperatures. Likewise, this condition performed well, reaching values above 20 J for test temperatures of 100 °C and 200 °C. However, there is a considerable difference in the energy absorbed between quasi-static tensile tests and high-speed impact tests, in which the fracture mechanism and its interaction with the microstructure differ. In the case of the impact test, unstable austenite rapidly transforms into martensite, contributing to a minimal TRIP effect. In any case, these DBTT curves are a good benchmark for the industry to understand the behavior of maraging steels printed by L-PBF under aged conditions, which can become a reference for future investigations to achieve an optimal strength-toughness ratio for this material.

6.2 Limitations

Some limitations of the study need to be addressed, as follows:

- The geometry of the coupons was defined based on the number of testing and characterization samples required. The build plate area was limited to the direct printing of 105 impact specimens and 3 tensile samples. Therefore, prismatic coupons were used and subsequently machined.
- The presence of nanoprecipitates in the microstructure of the directly aged samples could not be clearly observed and quantified. As reported in the literature, more complex characterization techniques such as TEM would be necessary to quantify the size, morphology, and chemical composition of the nanoprecipitates, since the SEM

equipment employed in this project does not have sufficient resolution to characterize these precipitates. Due to the limited time frame and budget of this project, the focus was solely on analyzing the presence of martensite and austenite in the microstructure of the material.

- In addition, Electron Backscatter Diffraction (EBSD) techniques could have been used to investigate the crystallographic structure of the analyzed microstructure, providing information on the presence of austenite and martensite for each aging condition studied. However, due to equipment availability and limited project deadlines, such characterizations were not performed.

- Due to furnace limitations and sample availability, it was not possible to test Charpy impact test at higher temperatures (i.e. above 300 °C) to confirm the ductile / brittle temperature plateau.

- The laser extensometer was initially intended as a means of measuring the deformation of tensile specimens during tensile loading. Due to gripping issues involving the cylindrical specimens during the initial stages of deformation, the data from the triplicate specimens were inconsistent among each other. Therefore, only the strain data obtained by DIC was considered for engineering strain calculations, which were consistent with the predictions.

6.3 Future Research

Firstly, a more detailed analysis of the influence of intermetallic nanoprecipitates on the microstructure of L-PBF-printed maraging steel could be investigated by analyzing particle size, composition, and how it affects dislocation pile-up as tensile and impact stresses occur. This could also be linked to the Orowan strengthening mechanism, analyzing the contributing factors for each relevant stage of deformation. A study could be conducted to evaluate strategies for increasing the stability of austenite in order to improve the impact toughness of maraging steels while maintaining high tensile strength. In-situ or post-mortem analyses could be performed to determine the percentage of austenite in the specimen as tensile stress is applied or after fracture. Cryogenic or high-temperature tensile tests can be performed to evaluate the mechanical behavior of maraging steel under critical conditions. Finally, new heat treatment strategies such as cyclic solution and two-step aging processes can be explored to achieve better strength-toughness relationship for printed maraging steel.

REFERENCES

[1] O. Diegel, J. Kowen, and T. Wohlers, “Wohlers Report 2024,” Wohlers Associates, Tech. Rep., 2024. [Online]. Available: https://wohlersassociates.com/product/wr2024/

[2] ASM International, *Properties and selection: Irons, steels, and high performance alloys*, 10th ed. ASM Handbook, 1 1990, vol. 1.

[3] L. Guo, L. Zhang, J. Andersson, and O. Ojo, “Additive manufacturing of 18% nickel maraging steels: Defect, structure and mechanical properties: A review,” *Journal of Material Science and Technology*, vol. 120, pp. 227–252, 3 2022. [Online]. Available: https://doi.org/10.1016/j.jmst.2021.10.056

[4] M. J. Paul, Y. Muniandy, J. J. Kruzic, U. Ramamurty, and B. Gludovatz, “Effect of heat treatment on the strength and fracture resistance of a laser powder bed fusion-processed 18Ni-300 maraging steel,” *Materials Science and Engineering A*, vol. 844, p. 143167, 4 2022. [Online]. Available: https://doi.org/10.1016/j.msea.2022.143167

[5] M. Osman, S. Sarafan, P. Wanjara, F. Bernier, S. E. Atabay, J. Gholipour, M. Molavi-Zarandi, J. Soost, and M. Brochu, “Effect of heat treatment on the microstructure and mechanical properties of 18NI-300 maraging steel produced by Additive–Subtractive Hybrid Manufacturing,” *Materials*, vol. 16, no. 13, p. 4749, 6 2023. [Online]. Available: https://doi.org/10.3390/ma16134749

[6] J. Li, D. Zhan, Z. Jiang, H. Zhang, Y. Yang, and Y. Zhang, “Progress on improving strength-toughness of ultra-high strength martensitic steels for aerospace applications: A review,” *Journal of Materials Research and Technology*, vol. 23, pp. 172–190, 1 2023. [Online]. Available: https://doi.org/10.1016/j.jmrt.2022.12.177

[7] U. Kizhakkinan, S. Seetharaman, N. Raghavan, and D. W. Rosen, “Laser powder bed fusion additive manufacturing of maraging steel: A review,” *Journal of Manufacturing Science and Engineering*, vol. 145, no. 11, 8 2023. [Online]. Available: https://doi.org/10.1115/1.4062727

[8] T. Wohlers and T. Gornet, “History of Additive Manufacturing,” Wohlers Associates, Tech. Rep., 2016. [Online]. Available: https://wohlersassociates.com/wp-content/uploads/2022/08/history2016.pdf

[9] ASTM 52900, *Additive manufacturing general principles terminology.* West Conshohocken, PA, USA: ASTM Standard, 2012.

[10] F. Calignano, M. Galati, and L. Iuliano, “A metal powder bed fusion process in industry: Qualification considerations,” *Machines*, vol. 7, no. 4, p. 72, 11 2019. [Online]. Available: https://doi.org/10.3390/machines7040072

[11] E. Atzeni and A. Salmi, “Economics of additive manufacturing for end-usable metal parts,” *The International Journal of Advanced Manufacturing Technology*, vol. 62, no. 9-12, pp. 1147–1155, 2 2012. [Online]. Available: https://doi.org/10.1007/s00170-011-3878-1

[12] C. R. Deckard, “Method and apparatus for producing parts by selective sintering,” Sep. 5 1989, US Patent 4863538.

[13] H. Abdel-Aal, *Additive Manufacturing of Metals: Fundamentals and Testing of 3D and 4D Printing*, 1st ed. McGraw Hill Professional, 2022.

[14] E. Lavernia, J. Shackelford, B. Zheng, K. Ma, and J. Schoenung, *Metallic powders for additive manufacturing.* John Wiley Sons, 2 2024. [Online]. Available: https://doi.org/10.1002/9781119908142

[15] H. Kotadia, G. Gibbons, A. Das, and P. Howes, “A review of laser powder bed fusion additive manufacturing of aluminium alloys: Microstructure and properties,” *Additive manufacturing*, vol. 46, p. 102155, 7 2021. [Online]. Available: https://doi.org/10.1016/j.addma.2021.102155

[16] S. Lathabai, *Additive manufacturing of Aluminium-Based alloys and composites.* Woodhead Publishing, 1 2018. [Online]. Available: https://doi.org/10.1016/b978-0-08-102063-0.00002-3

[17] O. Rayan, J. Brousseau, C. Belzile, and A. E. Ouafi, “Maraging steel powder recycling effect on the tensile and fatigue behavior of parts produced through the laser powder bed fusion (L-PBF) process,” *The International Journal of Advanced Manufacturing Technology*, vol. 127, no. 3-4, pp. 1737–1754, 6 2023. [Online]. Available: https://doi.org/10.1007/s00170-023-11522-x

[18] S. Svozilova, I. Zetková, J. F. S. Marin, and J. A. T. Garay, “Evaluation of recycled and reused metal powders for DMLS 3D printing,” *Materials*, vol. 17, no. 24, p. 6184, 12 2024. [Online]. Available: https://doi.org/10.3390/ma17246184

[19] A. Brandão, R. Gerard, J. Gumpinger, S. Beretta, A. Makaya, L. Pambaguian, and T. Ghidini, "Challenges in additive manufacturing of space parts: Powder feedstock Cross-Contamination and its impact on end products," *Materials*, vol. 10, no. 5, p. 522, 5 2017. [Online]. Available: https://doi.org/10.3390/ma10050522

[20] Y.-Q. Liu, Z. Xiong, Y.-L. Zhang, and H. Liu, "Breakthroughs in projection-enabled additive manufacturing: From novel strategies to cutting-edge applications," *The Innovation*, vol. 4, no. 3, p. 100395, 3 2023. [Online]. Available: https://doi.org/10.1016/j.xinn.2023.100395

[21] L. Zhou, J. Miller, J. Vezza, M. Mayster, M. Raffay, Q. Justice, Z. A. Tamimi, G. Hansotte, L. D. Sunkara, and J. Bernat, "Additive manufacturing: A comprehensive review," *Sensors*, vol. 24, no. 9, p. 2668, 4 2024. [Online]. Available: https://doi.org/10.3390/s24092668

[22] M. Mashhadikarimi, Y. Aghayar, P. Moazzen, M. Masoumi, S. Shamsdini, and M. Mohammadi, "Hybrid additive manufactured tool steels: Microstructural modifications and mechanical enhancements through heat treatments," *Materialia*, p. 102552, 9 2025. [Online]. Available: https://doi.org/10.1016/j.mtla.2025.102552

[23] O. Diegel, A. Nordin, and D. Motte, *A practical guide to design for additive manufacturing.* Springer Nature, 1 2019. [Online]. Available: https://doi.org/10.1007/978-981-13-8281-9

[24] F. J. M. Rivera and A. J. R. Arciniegas, "Additive manufacturing methods: techniques, materials, and closed-loop control applications," *The International Journal of Advanced Manufacturing Technology*, vol. 109, no. 1-2, pp. 17–31, 6 2020. [Online]. Available: https://doi.org/10.1007/s00170-020-05663-6

[25] T. G. Spears and S. A. Gold, "In-process sensing in selective laser melting (SLM) additive manufacturing," *Integrating materials and manufacturing innovation*, vol. 5, no. 1, pp. 16–40, 2 2016. [Online]. Available: https://doi.org/10.1186/s40192-016-0045-4

[26] A. F. De Souza, K. S. Al-Rubaie, S. Marques, B. Zluhan, and E. C. Santos, "Effect of laser speed, layer thickness, and part position on the mechanical properties of maraging 300 parts manufactured by selective laser melting," *Materials Science and Engineering A*, vol. 767, p. 138425, 9 2019. [Online]. Available: https://doi.org/10.1016/j.msea.2019.138425

[27] I. Gibson, D. W. Rosen, and B. Stucker, *Additive manufacturing technologies: Rapid prototyping to direct digital manufacturing.* Springer, 1 2009. [Online]. Available: http://dro.deakin.edu.au/eserv/DU:30063904/gibson-additivemanufacturing-2010.pdf

[28] M. Korpela, N. Riikonen, H. Piili, A. Salminen, and O. Nyrhilä, "Additive manufacturing: Past, present, and the future," *Technical, economic and societal effects of manufacturing*, vol. 4, no. 0, pp. 17–41, 2020.

[29] J. O. Milewski, *Additive manufacturing of metals: from fundamental technology to rocket nozzles, medical implants, and custom jewelry.* Springer, 7 2017.

[30] N. D. Dejene and H. G. Lemu, "Current status and challenges of powder bed fusion-based metal additive manufacturing: Literature review," *Metals*, vol. 13, no. 2, p. 424, 2 2023. [Online]. Available: https://doi.org/10.3390/met13020424

[31] W. Abd-Elaziem, S. Elkatatny, A.-E. Abd-Elaziem, M. Khedr, M. A. A. El-Baky, M. A. Hassan, M. Abu-Okail, M. Mohammed, A. Järvenpää, T. Allam, and A. Hamada, "On the current research progress of metallic materials fabricated by laser powder bed fusion process: a review," *Journal of Materials Research and Technology*, vol. 20, pp. 681–707, 7 2022. [Online]. Available: https://doi.org/10.1016/j.jmrt.2022.07.085

[32] C. Panwisawas, Y. T. Tang, and R. C. Reed, "Metal 3D printing as a disruptive technology for superalloys," *Nature Communications*, vol. 11, no. 1, 5 2020. [Online]. Available: https://doi.org/10.1038/s41467-020-16188-7

[33] J. F. Ready, *LIA handbook of Laser materials processing.* Laser Institute America: Magnolia Publishing, 1 2001. [Online]. Available: https://ci.nii.ac.jp/ncid/BA52752035

[34] Y. Zhang, S. Wu, Z. Guo, G. Peng, L. Wang, and W. Yan, "Defects caused by powder spattering and entrainment in laser powder bed fusion process: High-fidelity modeling of gas, melt pool and powder dynamics," *Acta Materialia*, p. 120816, 2 2025. [Online]. Available: https://doi.org/10.1016/j.actamat.2025.120816

[35] H. Wan, Z. Zhou, C. Li, G. Chen, and G. Zhang, "Effect of scanning strategy on grain structure and crystallographic texture of Inconel 718 processed by selective laser melting," *Journal of Material Science and Technology*, vol. 34, no. 10, pp. 1799–1804, 2 2018. [Online]. Available: https://doi.org/10.1016/j.jmst.2018.02.002

[36] T. Bhardwaj and M. Shukla, "Effect of laser scanning strategies on texture, physical and mechanical properties of laser sintered maraging steel," *Materials*

Science and Engineering A, vol. 734, pp. 102–109, 7 2018. [Online]. Available: https://doi.org/10.1016/j.msea.2018.07.089

[37] S. B. Joo, G. W. No, Y. H. Jung, M. J. Baek, D. J. Lee, and J. G. Kim, "Scan strategy effect on the mechanical properties and microstructure of directed energy deposited 18NI300 maraging steel," *Korean Journal of Metals and Materials*, vol. 63, no. 1, pp. 1–10, 12 2024. [Online]. Available: https://doi.org/10.3365/kjmm.2025.63.1.1

[38] B. Mooney, K. I. Kourousis, and R. Raghavendra, "Plastic anisotropy of additively manufactured maraging steel: Influence of the build orientation and heat treatments," *Additive manufacturing*, vol. 25, pp. 19–31, 10 2018. [Online]. Available: https://doi.org/10.1016/j.addma.2018.10.032

[39] S. P. Karlapudy, T. Nancharaiah, and V. V. S. Rao, "Influence of post-heat treatment on microstructure, texture, and mechanical properties of 18Ni-300 maraging steel fabricated by using LPBF technique," *Progress in Additive Manufacturing*, vol. 9, no. 6, pp. 1667–1682, 11 2023. [Online]. Available: https://doi.org/10.1007/s40964-023-00530-8

[40] Y. Bai, Y. Yang, D. Wang, and M. Zhang, "Influence mechanism of parameters process and mechanical properties evolution mechanism of maraging steel 300 by selective laser melting," *Materials Science and Engineering A*, vol. 703, pp. 116–123, 6 2017. [Online]. Available: https://doi.org/10.1016/j.msea.2017.06.033

[41] J. Mutua, S. Nakata, T. Onda, and Z.-C. Chen, "Optimization of selective laser melting parameters and influence of post heat treatment on microstructure and mechanical properties of maraging steel," *Materials Design*, vol. 139, pp. 486–497, 11 2017. [Online]. Available: https://doi.org/10.1016/j.matdes.2017.11.042

[42] G. Casalino, S. Campanelli, N. Contuzzi, and A. Ludovico, "Experimental investigation and statistical optimisation of the selective laser melting process of a maraging steel," *Optics Laser Technology*, vol. 65, pp. 151–158, 8 2014. [Online]. Available: https://doi.org/10.1016/j.optlastec.2014.07.021

[43] S. Sarafan, P. Wanjara, J. Gholipour, F. Bernier, M. Osman, F. Sikan, M. Molavi-Zarandi, J. Soost, and M. Brochu, "Evaluation of maraging steel produced using Hybrid Additive/Subtractive Manufacturing," *Journal of Manufacturing and Materials Processing*, vol. 5, no. 4, p. 107, 10 2021. [Online]. Available: https://doi.org/10.3390/jmmp5040107

[44] A. Suzuki, R. Nishida, N. Takata, M. Kobashi, and M. Kato, "Design of laser parameters for selectively laser melted maraging steel based on deposited energy density," *Additive manufacturing*, vol. 28, pp. 160–168, 5 2019. [Online]. Available: https://doi.org/10.1016/j.addma.2019.04.018

[45] T. Larimian, B. AlMangour, D. Grzesiak, G. Walunj, and T. Borkar, "Effect of laser spot size, scanning strategy, scanning speed, and laser power on microstructure and mechanical behavior of 316L stainless steel fabricated via selective laser melting," *Journal of Materials Engineering and Performance*, vol. 31, no. 3, pp. 2205–2224, 11 2021. [Online]. Available: https://doi.org/10.1007/s11665-021-06387-8

[46] L. Mugwagwa, I. Yadroitsev, and S. Matope, "Effect of process parameters on residual stresses, distortions, and porosity in selective laser melting of maraging Steel 300," *Metals*, vol. 9, no. 10, p. 1042, 9 2019. [Online]. Available: https://doi.org/10.3390/met9101042

[47] S. Chowdhury, N. Yadaiah, C. Prakash, S. Ramakrishna, S. Dixit, L. R. Gupta, and D. Buddhi, "Laser powder bed fusion: A state-of-the-art review of the technology, materials, properties amp; defects, and numerical modelling," *Journal of Materials Research and Technology*, vol. 20, pp. 2109–2172, 8 2022. [Online]. Available: https://doi.org/10.1016/j.jmrt.2022.07.121

[48] Y. Bai, Y. J. Lee, C. Li, and H. Wang, "Densification behavior and influence of building direction on high anisotropy in selective laser melting of High-Strength 18Ni-Co-Mo-Ti maraging steel," *Metallurgical and Materials Transactions A*, vol. 51, no. 11, pp. 5861–5879, 9 2020. [Online]. Available: https://doi.org/10.1007/s11661-020-05978-9

[49] A. Santana, A. Eres-Castellanos, J. A. Jimenez, R. Rementeria, C. Capdevila, and F. G. Caballero, "Effect of layer thickness and laser emission mode on the microstructure of an additive manufactured maraging steel," *Journal of Materials Research and Technology*, vol. 25, pp. 6898–6912, 7 2023. [Online]. Available: https://doi.org/10.1016/j.jmrt.2023.07.114

[50] K. Kempen, E. Yasa, L. Thijs, J.-p. Kruth, and J. Van Humbeeck, "Microstructure and mechanical properties of selective laser melted 18Ni-300 steel," *Physics Procedia*, vol. 12, pp. 255–263, 1 2011. [Online]. Available: https://doi.org/10.1016/j.phpro.2011.03.033

[51] Q. Nguyen, D. Luu, S. Nai, Z. Zhu, Z. Chen, and J. Wei, "The role of powder layer thickness on the quality of SLM printed parts," *Archives of Civil and*

Mechanical Engineering, vol. 18, no. 3, pp. 948–955, 3 2018. [Online]. Available: https://doi.org/10.1016/j.acme.2018.01.015

[52] H. K. Kim, D. Han, J. Jo, and S. Kim, "Effect of layer thickness on internal pore and mechanical properties of hybrid additive manufactured 18Ni-300 maraging steel," *The International Journal of Advanced Manufacturing Technology*, 12 2024. [Online]. Available: https://doi.org/10.1007/s00170-024-14864-2

[53] S. Z. Hussain, Z. Kausar, Z. U. Koreshi, S. R. Sheikh, H. Z. U. Rehman, H. Yaqoob, M. F. Shah, A. Abdullah, and F. Sher, "Feedback control of melt pool area in selective laser melting additive manufacturing process," *Processes*, vol. 9, no. 9, p. 1547, 8 2021. [Online]. Available: https://doi.org/10.3390/pr9091547

[54] L. Dowling, J. Kennedy, S. O'Shaughnessy, and D. Trimble, "A review of critical repeatability and reproducibility issues in powder bed fusion," *Materials Design*, vol. 186, p. 108346, 11 2019. [Online]. Available: https://doi.org/10.1016/j.matdes.2019.108346

[55] K. Abd-Elghany and D. Bourell, "Property evaluation of 304L stainless steel fabricated by selective laser melting," *Rapid Prototyping Journal*, vol. 18, no. 5, pp. 420–428, 7 2012. [Online]. Available: https://doi.org/10.1108/13552541211250418

[56] T. DebRoy, H. Wei, J. Zuback, T. Mukherjee, J. Elmer, J. Milewski, A. Beese, A. Wilson-Heid, A. De, and W. Zhang, "Additive manufacturing of metallic components: Process, structure and properties," *Progress in Materials Science*, vol. 92, pp. 112–224, 10 2017. [Online]. Available: https://doi.org/10.1016/j.pmatsci.2017.10.001

[57] ASTM B213, *Standard test methods for flow rate of metal powders using the Hall Flowmeter funnel*. West Conshohocken, PA, USA: ASTM Standard, 2020.

[58] J. Clayton, "Optimising metal powders for additive manufacturing," *Metal Powder Report*, vol. 69, no. 5, pp. 14–17, 9 2014. [Online]. Available: https://doi.org/10.1016/s0026-0657(14)70223-1

[59] H. Sun, X. Chu, Z. Liu, A. Gisele, and Y. Zou, "Selective laser melting of maraging steels using recycled powders: A comprehensive microstructural and mechanical investigation," *Metallurgical and Materials Transactions A*, vol. 52, no. 5, pp. 1714–1722, 3 2021. [Online]. Available: https://doi.org/10.1007/s11661-021-06180-1

[60] A. P. Mouritz, *Introduction to aerospace materials*. Elsevier, May 2012.

[61] N. Takata, R. Nishida, A. Suzuki, M. Kobashi, and M. Kato, “Crystallographic features of microstructure in maraging steel fabricated by selective laser melting,” *Metals*, vol. 8, no. 6, p. 440, 6 2018. [Online]. Available: https://doi.org/10.3390/met8060440

[62] C. Tan, K. Zhou, M. Kuang, W. Ma, and T. Kuang, “Microstructural characterization and properties of selective laser melted maraging steel with different build directions,” *Science and Technology of Advanced Materials*, vol. 19, no. 1, pp. 746–758, 10 2018. [Online]. Available: https://doi.org/10.1080/14686996.2018.1527645

[63] S. Felicioni, A. Aversa, E. Librera, F. Bondioli, and P. Fino, “Directed energy deposition of 18NiM300 steel: Effect of process and post processing conditions on microstructure and properties,” *Science and Technology of Advanced Materials*, vol. 25, no. 1, 4 2024. [Online]. Available: https://doi.org/10.1080/14686996.2024.2346071

[64] Y. Yao, L. Fan, R. Ding, C. Franke, Z. Yang, W. Liu, T. Li, and H. Chen, “On the role of cellular microstructure in austenite reversion in selective laser melted maraging steel,” *Journal of Material Science and Technology*, vol. 184, pp. 180–194, 12 2023. [Online]. Available: https://doi.org/10.1016/j.jmst.2023.10.032

[65] W. Li, J. Chai, G. Liu, X. Rong, P. Wen, J. Su, and H. Chen, “On the role of chemically heterogeneous austenite in cryogenic toughness of maraging steels manufactured via laser powder bed fusion,” *Acta Materialia*, vol. 276, p. 120157, 7 2024. [Online]. Available: https://doi.org/10.1016/j.actamat.2024.120157

[66] S. Yin, C. Chen, X. Yan, X. Feng, R. Jenkins, P. O’Reilly, M. Liu, H. Li, and R. Lupoi, “The influence of aging temperature and aging time on the mechanical and tribological properties of selective laser melted maraging 18Ni-300 steel,” *Additive manufacturing*, vol. 22, pp. 592–600, 6 2018. [Online]. Available: https://doi.org/10.1016/j.addma.2018.06.005

[67] Y. Bai, D. Wang, Y. Yang, and H. Wang, “Effect of heat treatment on the microstructure and mechanical properties of maraging steel by selective laser melting,” *Materials Science and Engineering A*, vol. 760, pp. 105–117, 6 2019. [Online]. Available: https://doi.org/10.1016/j.msea.2019.05.115

[68] T. Tekin, G. Ischia, F. Naclerio, R. Ipek, and A. Molinari, “Effect of a direct aging heat treatment on the microstructure and the tensile properties of a 18Ni-300 maraging steel produced by Laser Powder Bed Fusion,” *Materials Science and Engineering A*, vol. 872, p. 144921, 3 2023. [Online]. Available: https://doi.org/10.1016/j.msea.2023.144921

[69] L. Jiang, C. Chen, and M. Zhang, "Effect of heat treatment on the properties of a high alloying maraging steel fabricated by laser metal deposition," *Metals and Materials International*, vol. 29, no. 1, pp. 141–156, 6 2022. [Online]. Available: https://doi.org/10.1007/s12540-022-01218-4

[70] A. Feitosa, G. Ribamar, J. Escobar, R. Sonkusare, T. Boll, F. Coury, J. Ávila, J. Oliveira, and A. Padilha, "Precipitation and reverted austenite formation in maraging 350 steel: Competition or cooperation?" *Acta Materialia*, vol. 270, p. 119865, 3 2024. [Online]. Available: https://doi.org/10.1016/j.actamat.2024.119865

[71] A. Santana, A. Eres-Castellanos, A. Królicka, J. D. Poplawsky, A. J. Clarke, C. Capdevila, and F. G. Caballero, "Collaborative or competitive phase transformation processes in an additively manufactured-maraging steel M300," *Journal of Materials Research and Technology*, 9 2025. [Online]. Available: https://doi.org/10.1016/j.jmrt.2025.09.243

[72] A. Królicka and J. Malawska, "Recent progress in laser powder bed fusions processes of advanced high-strength steels," *Materials*, vol. 17, no. 19, p. 4699, 9 2024. [Online]. Available: https://doi.org/10.3390/ma17194699

[73] D. Kim, T. Kim, K. Ha, J.-J. Oak, J. B. Jeon, Y. Park, and W. Lee, "Effect of heat treatment condition on microstructural and mechanical anisotropies of selective laser melted maraging 18NI-300 steel," *Metals*, vol. 10, no. 3, p. 410, 3 2020. [Online]. Available: https://doi.org/10.3390/met10030410

[74] G. W. No, J. Jeong, G. H. Ryu, J. B. Seol, and J. G. Kim, "Mechanical properties and microstructure of laser powder bed fusion-processed 18Ni300 maraging steel according to direct aging treatment conditions," *steel research international*, 9 2024. [Online]. Available: https://doi.org/10.1002/srin.202400348

[75] ISO 148-1, *Metallic materials — Charpy pendulum impact test*. Geneva: ISO Standard, 2016.

[76] ASTM E23, *Standard test methods for notched bar Impact testing of metallic materials*. West Conshohocken, PA, USA: ASTM International, 2012.

[77] I. Hatos, H. Hargitai, G. Fekete, and I. Fekete, "Effect of energy density on the mechanical properties of 1.2709 maraging steel produced by laser powder bed fusion," *Materials*, vol. 17, no. 14, p. 3432, 7 2024. [Online]. Available: https://doi.org/10.3390/ma17143432

[78] M. Rombouts, E. Yasa, J. Luyten, J. Deckers, and J. Kruth, *Experimental investigation of charpy impact tests on metallic SLM parts.* Taylor Francis, September 2009. [Online]. Available: https://doi.org/10.1201/9780203859476.ch30

[79] E. Yasa, K. Kempen, J.-P. Kruth, L. Thijs, and H. van As, "Microstructure and mechanical properties of maraging steel 300 after selective laser melting," *21st Annual International Solid Freeform Fabrication Symposium - An Additive Manufacturing Conference, SFF 2010*, pp. 383–396, 01 2010.

[80] G. Lupi, E. Bettini, F. Deirmina, and R. Casati, "Microstructural and mechanical properties of a novel cobalt and titanium free maraging steel for laser powder bed fusion," *Journal of Materials Research and Technology*, vol. 30, pp. 1269–1278, 3 2024. [Online]. Available: https://doi.org/10.1016/j.jmrt.2024.03.088

[81] F. Deirmina, P. A. Davies, and R. Casati, "Effects of powder atomization route and post-processing thermal treatments on the mechanical properties and fatigue resistance of additively manufactured 18Ni300 maraging steel," *Advanced Engineering Materials*, vol. 24, no. 4, 9 2021. [Online]. Available: https://doi.org/10.1002/adem.202101011

[82] ASTM B212, *Standard test method for apparent density of free-flowing metal powders using the Hall flowmeter funnel.* West Conshohocken, PA, USA: ASTM Standard, 2021.

[83] ASTM B311, *Standard test method for density of powder metallurgy (PM) materials containing less than two percent porosity.* West Conshohocken, PA, USA: ASTM Standard, 2017.

[84] ASTM E975, "Practice for X-Ray determination of retained austenite in steel with near random crystallographic orientation," *ASTM Standard*, 11 2022. [Online]. Available: https://doi.org/10.1520/e0975-22

[85] A. Young, "The rietveld method," *Crystal Research and Technology*, vol. 30, no. 4, p. 494, 1 1995. [Online]. Available: https://doi.org/10.1002/crat.2170300412

[86] ASTM E8/E8M, *Standard test methods for tension testing of metallic materials.* West Conshohocken, PA, USA: ASTM International, 2022.

[87] ASTME384, "Test method for microindentation hardness of materials," *ASTM Standarda*, 10 2022. [Online]. Available: https://doi.org/10.1520/e0384-22

[88] J. H. Tan, W. L. E. Wong, and K. W. Dalgarno, "An overview of powder granulometry on feedstock and part performance in the selective laser melting

process," *Additive manufacturing*, vol. 18, pp. 228–255, 10 2017. [Online]. Available: https://doi.org/10.1016/j.addma.2017.10.011

[89] W. Guo, C. Guo, and Q. Zhu, "Heat treatment behavior of the 18Ni300 maraging steel additively manufactured by selective laser melting," *Materials science forum*, vol. 941, pp. 2160–2166, 12 2018. [Online]. Available: https://doi.org/10.4028/www.scientific.net/msf.941.2160

[90] A. Strakosova, F. Průša, P. Jiříček, J. Houdková, A. Michalcová, and D. Vojtěch, "High-temperature exposure of the high-strength 18Ni-300 maraging steel manufactured by laser powder bed fusion: Oxidation, structure and mechanical changes," *Journal of Materials Science*, vol. 59, no. 33, pp. 15 859–15 882, 8 2024. [Online]. Available: https://doi.org/10.1007/s10853-024-10102-y

[91] F. Conde, J. Escobar, J. Oliveira, A. Jardini, W. B. Filho, and J. Avila, "Austenite reversion kinetics and stability during tempering of an additively manufactured maraging 300 steel," *Additive manufacturing*, vol. 29, p. 100804, 7 2019. [Online]. Available: https://doi.org/10.1016/j.addma.2019.100804

[92] R. Kannan, D. N. Leonard, and P. Nandwana, "Optimization of direct aging temperature of Ti free grade 300 maraging steel manufactured using laser powder bed fusion (LPBF)," *Materials Science and Engineering A*, vol. 817, p. 141266, 4 2021. [Online]. Available: https://doi.org/10.1016/j.msea.2021.141266

[93] C. Paul, J. Vincic, A. Wall, A. Jones, L. Tobber, and M. J. Benoit, "Investigation of micro-spot laser directed energy deposition of 18Ni-300 maraging steel towards repair applications," *The International Journal of Advanced Manufacturing Technology*, vol. 135, no. 9-10, pp. 4339–4357, 11 2024. [Online]. Available: https://doi.org/10.1007/s00170-024-14755-6